CHEMICAL AND PHYSICAL MODIFICATION OF GRAPHITIC MATERIALS BY OXIDATIVE PROCESSES AND SOLVENT INTERCALATION

A Thesis

by

CARRIE BETH WERKE

Submitted to the Office of Graduate and Professional Studies of
Texas A&M University
in partial fulfillment of the requirements for the degree of

MASTER OF SCIENCE

Chair of Committee,	James D. Batteas
Committee Members,	David H. Russell
	Hong Liang
Head of Department,	David H. Russell

December 2014

Major Subject: Chemistry

ABSTRACT

Graphene and graphite are materials of high interest for many applications. In order to increase the possible uses of these materials, more must be understood about how their properties can be modified. One way to modify graphitic properties is by chemical functionalization, such as oxidation. This work looks at two different oxidation techniques for graphite; UV/O_3 exposure and biased AFM lithography for broad and local oxidation, respectively. For the supported graphitic samples including graphene, it is important to understand how sample preparation can lead to contamination in addition to investigating how to chemically and physically manipulate the graphitic properties. Three different mechanical exfoliation sample preparations were used to create samples, and each method was investigated with biased lithography.

UV/O_3 exposure is able to form graphite oxide with only the exposed area undergoing oxidation. It was found that the length of exposure time could be linearly correlated to the amount of defects as determined by Raman spectroscopy. Biased AFM lithography of graphite was also able to oxidize graphite, in a localized pattern instead of entire exposed area. By controlling the lithography conditions, the extent of oxidation in an area could be manipulated.

Supported graphitic materials were created via Scotch tape, thermal release tape and water soluble tape. Each tape had unique sample preparation conditions, and each of the three samples yielded single to multilayer graphene surfaces which then underwent biased lithography. Biased lithography on each of these created surfaces

demonstrated the impact that sample preparation had on device creation as the samples had unique responses based on which method was used. Scotch tape samples saw growths stemming from the graphitic areas that underwent the biased lithography, thermal release tape samples formed wrinkles in the graphitic region while donuts, on the edges, and the water soluble tape showed oxidation of the graphitic region as well as the formation of bubbles. These bubbles are believed to be due to the solvent intercalation which was able to undergo electrolysis, a novel method for graphitic bubble formation.

DEDICATION

To my husband and family.

ACKNOWLEDGEMENTS

I would like to thank my committee chair, Dr. James D. Batteas, for his guidance and the opportunity to learn in such a new and exciting area of research. I would also like to thank Dr. David H. Russell, Dr. Huang Liang, Dr. Paul Cremer and Dr. Xing Cheng for serving on my current and past advisory committee.

Thank you to the Batteas Research group who helped foster ideas and gave of their own time and patience. Specifically I would like to acknowledge Brad for the comradery from the very beginning and for the friendship with him and Laura that helped to bolster me through the storms. Also a thank you to all those who made up the graphitic portion of the group, who added to this research by their insightful conversations and collaborations: Jiageng, Chi-Yuan, Jessica and Meagan.

Thank you to my friends and family who kept any thoughts that I was crazy for doing this to themselves and put forward the best fan base that I could have imagined. You were the ones that kept me sane and importantly your acceptance of me for who I am reminded me to stay true to myself. A special thank you to: my parents, Chris and Ruth, for their belief in my potential; my brothers, Robert and Jeffrey, for their unconditional love; my in-laws, Linda and Allen, for their acceptance of me into the family; my grandparents, Dolly and John, for their caring and prayers; and finally to all my wonderfully supportive aunts, uncles and cousins for the many ways that they showed family is a gift from God. To my wonderful friends who know how crazy

graduate school can be but still made me a priority: Laura, Ainsley, Lauren, Jenny, Krystal, Paul, and Jennifer, thanks for not giving up on me!

Tyler, you will always be the best thing that came from graduate school, your support, love, encouragement and joy have made all this possible. God has blessed me in numerous ways, which He reminds me of everyday with you.

Without my Creator nothing matters, but with Him, anything is possible.

Finally to all my fellow Aggies, including family, who have shown the unwavering Aggie support.

NOMENCLATURE

AFM	Atomic Force Microscope
BL	Bilayer Graphene
EG	Epitaxially Grown
FLG	Few Layer Graphene
GO	Graphene Oxide
HOPG	Highly Oriented Pyrolytic Graphite
MEMS	Microelectromechanical Syststems
ML	Monolayer Graphene
NEMS	Nanoelectromechanical Systems
RGO	Reduced Graphene Oxide
TRT	Thermal Release Tape
V	Volts
WST	Water Soluble Tape
XPS	X-ray Photoelectron Spectroscopy

TABLE OF CONTENTS

Page

Page

LIST OF FIGURES

Page

Page

Page

CHAPTER I

INTRODUCTION

1.1 Graphite and Graphene Introduction

In 1564, one of the first applications of graphite was implemented with the invention of the pencil.[1] Outside of its work as a writing utensil, graphite has also been used in solid lubricants,[2] batteries,[3] and nuclear reactors,[4] it is a very versatile material as its multiple notable properties have led to different applications. Graphite itself is a three-dimensional stacked system of single sheets of graphene held together by van der Waals forces. These single sheets are made up of a network of connected six member rings consisting of solely carbon with sp^2 hybridization forming a conjugated π system, also known as a honeycomb structure shown in Figure 1.1. The single sheet can form other allotropes such as 1-dimensional carbon nanotubes and 0-dimensional buckminsterfullerenes, commonly known as buckyballs. While graphite has an extensive history, buckminister fullerenes arrived on the scene in 1985[5] and carbon nanotubes in 1991,[6] but graphene is the newest, being isolated and identified by Giem and Novoselov in 2004 which then earned them the Nobel Prize in Physics in 2010.[7] Before their successful isolation of graphene it had been theoretically predicted in 1934 by Peierls,[8] in 1937 by Landau,[9] and in 1968 by Mermin[10] that two dimensional materials were not possible, as they were not thermodynamically stable. So while theoretical work had been conducted on the two dimensional form of graphite, it was only after 2004 that graphene could be experimentally studied.

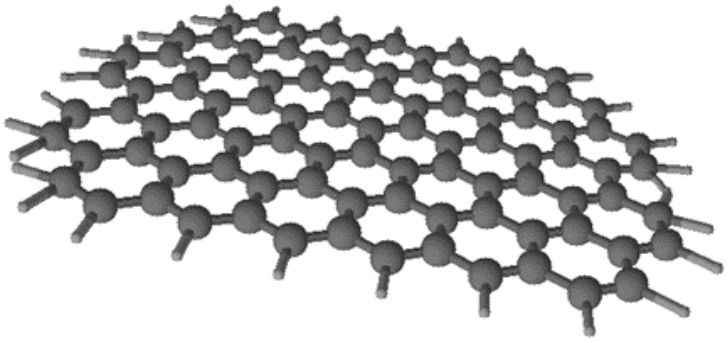

Figure 1.1 Graphene honeycomb structure.

The first method of isolating graphene was remarkably simple, it was accomplished by mechanical exfoliation of highly oriented pyrolytic graphite (HOPG) with Scotch tape, which has thus also been referred to as the 'Scotch Tape Method'.[7] The ease of generating this phenomenal 2-dimensional material opened it up for large amounts of research by making it available to a broad group of scientists all at once. Therefore, though it was first isolated a decade ago, there has been a plethora of research conducted investigating the properties graphene brings to the table. Graphene was found to have high optical transparency, incredible electronic properties and mechanical properties, which has led to a wide range of possible applications. [11-13] Being a 2-dimensional material, graphene has an incredibly large surface area to volume ratio, meaning any changes to the surface are going to have a profound effect on these properties, so that tailoring graphitic surfaces can lead to specialized functions. Thus graphite, graphene, and its multilayer forms, bilayer and few layer, have led to much

research with the goal of advancing this carbon allotrope into even more usable products.

1.2 Creating Graphitic Samples

With so many different studies being conducted on graphitic materials, it is important to note that not all graphite and graphene samples are equal and much depends on the sample preparation. This means that it is important to note how samples were made and under what conditions they were tested as this can have large impacts on the results. Some of the general observations about sample preparation are enumerated below to demonstrate that there are many means to prepare graphitic samples and that the process manner is very important.

Graphite can occur naturally as kish graphite, but the most commonly used graphite for research purposes is highly ordered pyrolytic graphite (HOPG), which is obtained from the pyrolysis of hydrocarbons at high temperatures.[14] HOPG is available commercially with differing quality dictated by the mosaic spread, where a lower mosaic spread means fewer steps in the cleaved surface. There are also different ways of obtaining graphene such as: the original mechanical exfoliation, chemical vapor deposition (CVD),[15] water soluble transfer of graphene oxide (GO) which is then reduced,[16] electrochemical exfoliation using ionic liquids,[17] unzipping of carbon nanotubes,[18] and epitaxial growth,[19] among others. These techniques create graphitic samples with differing numbers of defects, sizes, shapes, number of layers, and type of defects all dependent upon many of the variables in each creation process. The chemical

and physical characteristics of the graphene obtained will thus differ based on these conditions which all affect the graphene sample's mechanical and electronic properties.[20]

While there are many means to generate graphene samples, three of the most common ways of obtaining graphene are mechanical exfoliation, CVD, and the reduction of graphene oxide. Graphene obtained from mechanical exfoliation of HOPG tends to give more pristine graphene, but with smaller lateral dimensions; the number of layers and isolation of single layers are sample dependent and lately there have been studies about the effect that the tape is having on introducing small amounts of contaminants to both the graphene and the substrate.[21,22] CVD grown graphene, on the other hand, can be employed to create large lateral graphene or few layer graphene sheets with fairly controllable numbers of layers, but typically contains more defects in the honeycomb structure.[23] The third method involves using graphene oxide (GO) sheets which are soluble in water, which can allow for an easier placement of the graphene and reactions required for some product designs, but the subsequent reduction to the GO leaves residual oxidized species.[24] Not surprisingly, other mechanisms for obtaining graphene also have their advantages and disadvantages[25] and therefore depending upon the purpose and experimental conditions desired, the method of obtaining graphite, graphene and few layer graphitic supports must be chosen carefully.

1.3 Electronic Properties

One of the leading reasons graphitic materials are being so heavily investigated is due to their electronic properties. Graphite is a semi-metal with 100 times greater conductance across the plane than through the layers.[26] This is because across the sheet

of graphite there is an interconnected π system through which electrons can travel, while the layers themselves are held together by only the weaker van der Waals forces. So, in the same vein, a single graphene layer is also a semi-metal with a zero band gap. Still, just as the multilayers alter the electronic properties of the graphite through the material, so can the identity and structure of any materials on which graphene is supported. The first supported graphene structure on silicon dioxide exhibited a carrier mobility of ~ 10,000 cm^2/Vs at room temperature.[7] However, when the graphene was suspended and not interacting with a substrate the carrier mobility has been measured at almost 200,000 cm^2/Vs at low temperature (4.2 K).[27,28] This carrier mobility measured for the suspended graphene is much larger than silicon which has an electron mobility around 1,400 cm^2/Vs, as well as GaAs around 8,500 cm^2/Vs and that of organics, such as single crystal organic semiconductor rubrene at ~ 20 cm^2/Vs and the even smaller mobilities for naphthalene and anthracene.[29,30]

The carrier density for graphene again depends on how the sample was made, (*e.g.* grown or transferred). Typical graphene carrier densities range from 10^9 cm^{-2} for the low temperature suspended graphene[27] to 10^{12} cm^{-2} for exfoliated graphene on silicon dioxide[31] to 10^{13} cm^{-2} for epitaxial grown (EG) graphene on SiC.[32] In fact, just the transferring process of EG graphene onto silicon dioxide was observed to reduce the carrier concentration by half,[33] most likely due to the changing of the interactions with the substrate and defects introduced in the transfer process.

The cause for the high carrier mobilities observed can be thought of in terms of how the charge carriers are transported. Typically electrons moving through solids have

a mass that interacts with the crystal lattice of the solids they are flowing through and thus their progress is slowed down. Ballistic transport, however, is when the charge carriers do not experience any scattering interactions with the lattice. The electron transport in graphene has an effective mass approaching zero,[34] with electrons moving at the speed of light, unhindered by interactions with the solid.[35] Thus supporting the ballistic transport theory for graphene.[34] In graphene the transport of the carriers occurs in the continuous, flat π-system. Thus, the first truly 2-dimensional material analyzed, graphene, was found to have ballistic transport and even quasi-2-dimensional graphite has shown this behavior.[35] The best to-date electronic transport in epitaxial graphene is equivalent to a sheet resistance below 1 Ωper square, which beat the previous theoretical predictions.[36] This is well below amorphous gallium indium zinc oxide, which has been extensively investigated due to its potential applications as a thin film transistor, which showed sheet resistance of ~ 292 Ω per square.[37] When electron transport was studied in mesoscopic graphite at room temperature it was found to have a mean free path of ~ 2 μm, with a carrier mobility of ~ 10^7 cm^2/Vs and did not follow Ohm's law of strict proportional resistance to distance between voltage contacts, but had a length independent contribution from ballistic-like transport.[38]

While graphene is a two-dimensional material, when the breadth is limited graphene nanoribbons (GNR) are formed, which are quasi-1-dimensional systems. For electronic devices, the smaller nanoribbons are of high interest, plus with their narrow width, GNRs have unique electronic responses, with the formation of an energy gap due to the lateral confinement of the charge carriers, which also leads to a decrease in the

carrier mobility.[39,40] Depending on the size and method of obtaining GNRs, charge carriers can travel distances ranging from ~ 10 nanometers to over 10 μm without experiencing any scattering.[36,41] This considerable range stems from the methods used for creating the samples, with the small distance due to samples made via lithographically patterned exfoliated graphene whereas the larger distance coming from nanoribbons epitaxially grown on silicon carbide.[36,42] These results again emphasizes the importance of the sample preparation methods and that better device designs must take into account the first step, how the graphene is obtained. This ballistic or near-ballistic transport in 2-dimensional and quasi-1-dimensiontal graphene is what makes the carrier mobility so high, surpassing silicon, the staple of current electronics.[28] Combining this high carrier mobility with the high carrier concentration graphene shows great potential for future applications in electronics, either as a single sheet, few layer graphene or GNRs.

1.4 Electronic Applications

As described above, it is the high carrier concentrations and high mobilities that lend graphitic materials to electronic applications, with graphene as a possible new route toward smaller flexible electronics. It has already been observed that the change in local carrier concentration can be used to serve as a sensor. In fact, early after graphene's isolation, it was used for the detection of individual gas molecules, which had been beyond the sensitivity of previous solid-state gas sensors.[43] The big drive for graphene in advanced electronics though is through field effect transistors (FETs). FETs are electronic switches which work by changing the gate voltage to change the conductance

through a channel, a basic model of a FET is depicted in Figure 1.2. FETs are used in electronics such as in integrated circuits[44] and as amplifiers.[45] Before graphene can be used in FETs, the semi-metallic nature, with the implied lack of band gap, must be overcome since the pristine form would not make viable devices. Graphene's π and π* bands are conical, and as shown in Figure 1.3, touch at the Fermi level, which is located at the K-point in the Brillouin zone.[46] In order to have an effective FET, the device must show a dependence upon the gate voltage for the conductance across the sheet, which means there must be a band gap at the Fermi level that can be shifted. While in its pristine state graphene is without a band gap, as graphene either becomes functionalized, dimensionally confined, or the number of defects is increased, a band gap can be introduced. With the introduction of the band gap however there is a lowering of the carrier mobility and along with an altering of the carrier density, combining to show a net decrease on graphene's conductivity. Physically, when graphene is functionalized or has defects the π-system is partly broken, the surface can begin to pucker, losing its pure 2-dimensionality, producing sites where scattering can begin to become more dominant, yielding a decreased carrier mobility. Chemical functionalization also starts altering the chemistry, and thus the local density of states as well, affecting the carrier density. By modifying the extent of defects and functionalization, the electronic nature of graphene can be tuned from a semi-metal to a semiconductor, which introduces a controllable band gap to the graphene system. The type of functionalization or defects introduced also determines the nature of the semiconductor (p-type or n-type). In order for this to

actually be applicable in cases such as in FETs, the extent of functionalization must be controlled, and the ideal moieties to be introduced must be considered.

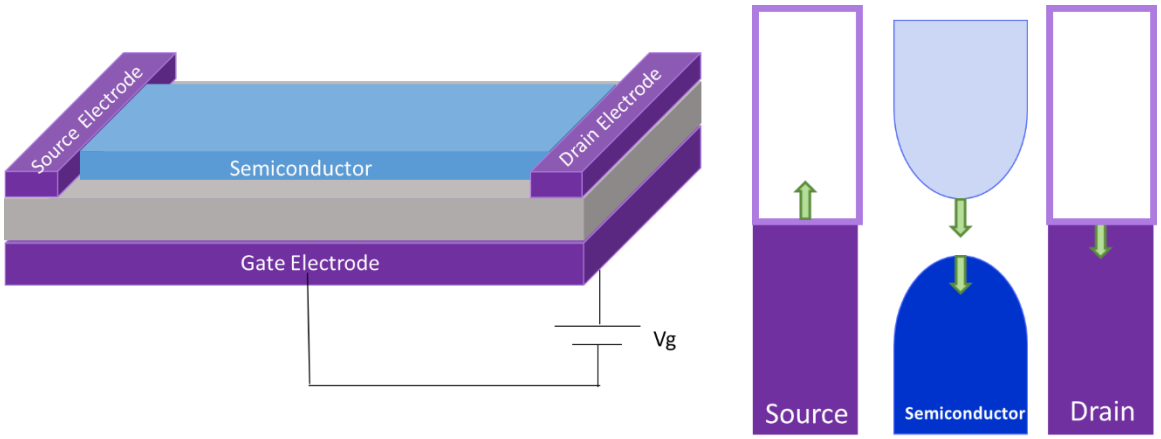

Figure 1.2 FET set up (left) and the band structure (right) of the source/drain and semiconductor with the green arrows indicating a change in location under an appropriate applied gate voltage.

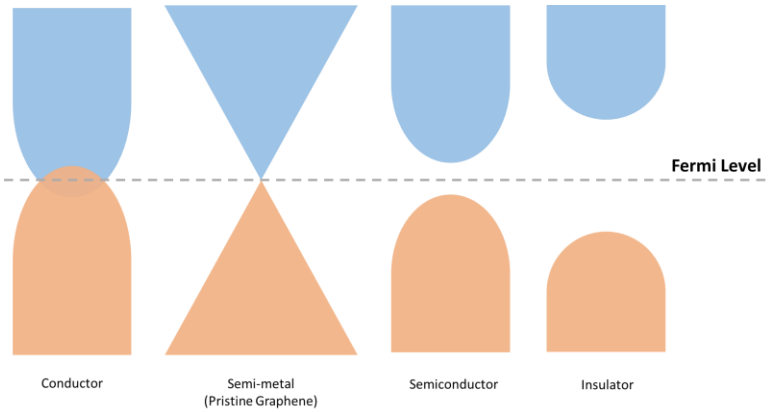

Figure 1.3 The band structure for conductors, pristine graphene as a semi-metal, semiconductors, and insulators.

As industry pushes for smaller and smaller electronic devices, there is a great desire to find smaller and thinner substances for FETs, and as graphene is a truly two-dimensional material it fits the bill. Due to this potential function, altering the graphene band gap has already been of much interest and many methods have been explored to do so.[47] One way that graphene has been altered to achieve a controllable band gap is by introducing defects to the graphene via a helium ion beam. The conduction through the lattice was tunable to the point where the FET had a current on-off switch ratio with two orders of magnitude.[48] Another way that the graphene π lattice has been opened is by photo-oxidation in the presence of water, which was found to reduce electron and hole mobility as monitored with Raman spectroscopy,.[49] However in that study the band gap was not determined and while it was presumably opened some, due to the chemical nature of the system changing, there is no direct relationship of the carrier mobility decreasing and the opening of the band gap. This points out the importance of determining both the carrier mobility and the band gap as they alter the conductivity responses for possible devices. There are other oxidation methods that have been used to create working graphene oxide FETs, such as by a modified Hummers method[50] and by exposure of graphene to UV/O_3.[51] With their large surface area to volume ratio, graphene FETs can show a strong response due to adsorption or reaction of molecules with the graphene surface. Thus, graphene FETs can also be used for sensing, with molecules that interact with the graphene FET, altering the voltage response, and thereby signaling a measurable change. Modified graphene FETs have been made into gas sensors for materials like nitrogen dioxide,[52] carbon dioxide,[53] and ammonia.[54] The

important thing when creating working FETs with graphene is the monitoring of the effect of the defect density on the band gap opening and carrier mobility and the resulting conductivity, so that controllable and reproducible designs can be achieved.

As stated above, when graphene is narrowed into GNRs, there is a band gap opening associated with the limited lateral dimension. Along with the band gap opening, the carrier mobility and the carrier concentration decrease, with the edge bonds having profound effects on the ribbon (denoted as edge effects).[39,40] A nanoribbon can thus be thought of as having both active and inactive regions, with the middle active region being where the charge transport occurs and the inactive region being the edge regions which cause boundary scattering.[55] Due to this the conduction through the GNRs has been found to scale inversely with the width of the GNR.[41] It was found that by creating 15 nm wide GNRs the band gap could be opened to ~ 200 meV.[39] This is consistent with early theoretical work which predicted that for graphene nanoribbons to have significantly higher carrier mobilities than the current silicon staple, the band gaps for the transistors will have to be less than 0.5 eV in order to maintain the ballistic transport; thus graphene nanoribbons show promise, but might not be as useful in the typical 0.5 - 1.0 eV FET range.[40]

While functionalizing graphene and confining its dimensions are two routes to induce a band gap, this also decreases the carrier mobility by decreasing the π orbital overlap and the number of carriers available. One way to establish a band gap without functionalizing graphene is by introducing strain, as graphene has a relation with its local curvature to its local electrochemical potential.[56] The introduction of strain

disrupts the π-system, which increases the number of scattering sites, but does not decrease the number of carriers. Strain can be induced when graphene conforms to a rough surface, or when graphene bubbles are created, or when graphene is placed on a flexible substrate or when suspended.[57-60] The altering of the electronic structure by strain has been observed via two-phonon Raman spectroscopy as uniaxial strain induces a deformation of the Dirac cone and displaces it away from the K point, yielding observable changes in the Raman spectrum,[61] shown in Figure 1.4. Simulation studies have proposed that creating graphene FETs by strain engineering can lead to improved operation, with calculated ON/OFF current ratios over 10^5:1 whereas most created ON/OFF ratios have been lower than 10:1.[62,63] It has also been predicted that the graphene band gap can be modulated from 0 eV up to 0.9 eV through shear deformation and uniaxial strain.[64] Graphene placed on flexible substrates allows for reversible and controlled strain of ~ 18 % with a corresponding change in the sheet resistance.[13]

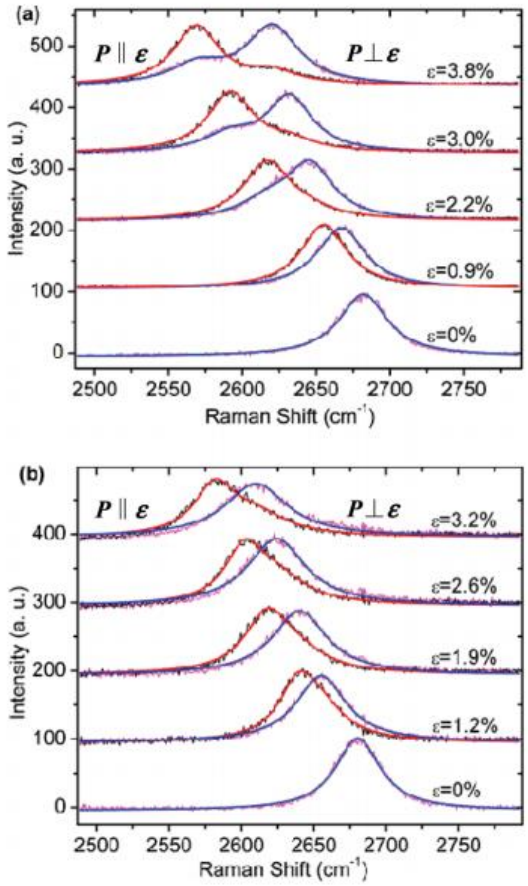

Figure 1.4 Shift in Raman peaks due to change in uniaxial strain. Reprinted with permission from ref 61. Copyright (2010) American Chemical Society.

GNRs can also experience strain and this too alters the electronic response. In armchair GNRs the changing of the ribbon width and amount of strain lead to an oscillation of the band gap; therefore strict control over the lateral size of the nanoribbon combined with precise control on the strain can yield controllable band gaps due to the quantum confinement effect.[65] Strain engineering of zigzag GNRs also shows a complex electronic correlation to strain.[66]

1.5 Frictional and Mechanical Properties

Outside of their electronic features and applications graphitic materials are also interesting for their frictional and mechanical properties. Mechanically graphene has the highest strength known, 100 times that of steel, and yet has high elasticity.[67] Carbon materials, such as diamond-like carbon show low coefficients of friction, lower than that of ice,[68] and graphite has similarly been used as a solid lubricant.[69,70] So along with its electronic characteristics, the mechanical characteristics of graphitic materials are also of high importance.

Each sheet in graphite is composed of strong covalent bonds between the carbon atoms, while the forces between the sheets, which have a 3.4 Å spacing, are much weaker, arising from van der Waals forces. Graphite lubricating materials take advantage of this lamellar structure, as the shearing of the layers leads to a reduction in the friction when sliding across the surface. In fact graphite has been proposed to exhibit suberlubricity when there is incommensurate contact with the top and bottom interacting layers, which would explain the measured 0.001 friction coefficients.[71] To test graphite as a lubricant, a three-ball slider set up measured the coefficient of friction for metals with and without lubricant. Without a lubricant, the coefficient of friction was 0.16-0.18, the metals with a mineral oil lubricant yielded a coefficient of friction of 0.15-0.17, and with a graphite film on the metal the coefficient of friction greatly dropped to 0.09-0.12.[72] Consequently graphite has been incorporated into solid lubricants that can be commerically found in stores today.[73]

With the advent of graphene, a great deal of interest was engendered in its possible application as a 2-dimensional or thin layer solid lubricant, especially for minute devices such as microelectromechanical systems (MEMS) and nanoelectromechanical systems (NEMS) devices.[20] However, the frictional properties of graphene have been found to differ from those of graphite; in fact, single layer, bilayer, few layer and bulk graphite have unique frictional characteristics. This follows from the differences in the interlayer interactions that are inherent in graphite, but are not the same for few layer or bilayer graphene, and of which there are none for single layer graphene.[74] When looking at how the differing number of layers of graphene alter the friction while either weakly bound to a substrate or suspended, it is observed that as the number of layers increases, the amount of friction decreases.[74] It has been proposed that the mechanism for the low friction for few layer graphene is due to the puckering effect,[75] where the top layers of graphene are able to deform and pucker around the stressor. Thinner samples on the other hand have a lower bending stiffness and therefore have an increased frictional resistance from the puckering effect as expressed in Figure 1.5.[76] This is because as the number of layers decreases, the amount of puckering around the tip, which is due to the out-of-plane deformation, increases. This increased puckering means an increased contact area and therefore increased friction.[20]

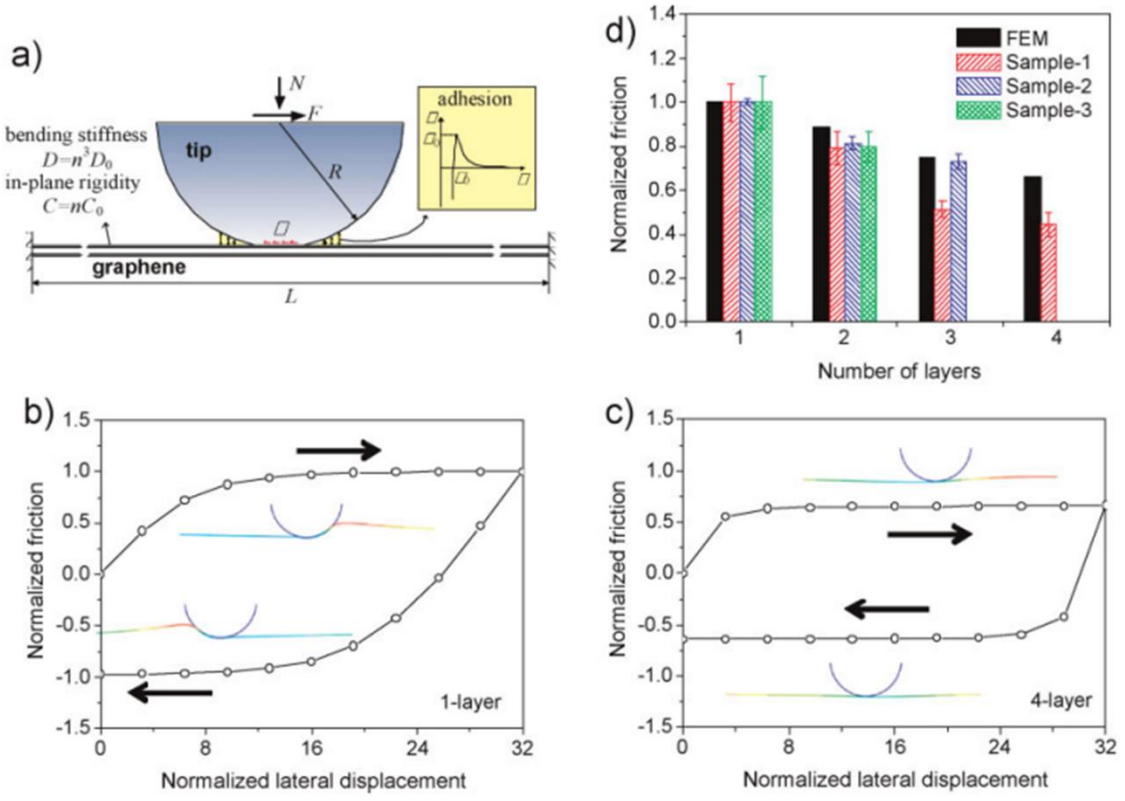

Figure 1.5 Increase in the friction due to the puckering effect. Reprinted with permission from ref 76. Copyright (2010) John Wiley and Sons.

Single layer to few layer graphene has been suggested as a protective coating, as a single sheet of graphene is impermeable to liquids and gases, including water and oxygen which can corrode or oxidize the substrate.[60] While this makes graphene a promising coating for surfaces, the frictional response has shown a great dependence on its support, or lack thereof.[76] This means the graphene-support interaction is an important factor on what, if any, role graphene can play as a solid lubricant. One reason graphene and layered graphene shows different responses on different substrates is due to the interaction of graphene with the substrate. Mica and silicon dioxide are common

substrates for graphene with very different frictional responses; when graphene is examined on mica there is a strong binding between the two materials, and thus the number of the graphene layers shows no dependence upon the amount of friction.[76] When graphene is placed on SiO_2/Si or suspended, the number of layers of graphene greatly affect the frictional response.[76] Even with non-mechanically transferred graphene, the substrate is an important factor, such as with epitaxially grown graphene films on SiC, which has a strong graphene-substrate interaction,[77] and has been shown to have the friction be cut in half by the growth of a single layer and the friction to be cut by another factor of two with the growth of bilayer graphene due to the puckering effect.[78] Thus, for graphene and/or few layer graphene to serve as both a protective and lubricating coating, its success is dependent upon the substrate and number of layers.

While graphene can keep water and oxygen from diffusing through its lattice, the method of sample preparation can sometimes lead to water becoming trapped between the substrate and the graphitic materials.[79] While trapped water has been observed between graphene and a mica substrate,[80] the study of how this water can then alter the frictional response of the graphene needs further exploration. It has even been found that with an increase in humidity, a fluid water film is able to form between the graphene and mica even when the graphene was initially applied while in a glove box with less than 5 ppm of each water and oxygen.[81] CVD graphene on Cu/SiO_2/Si has also been observed to have water intercalation during the copper etching, though it was not observed to be able to penetrate the graphene/Cu interface.[82] Rough substrates would also expect this water diffusion in humid environments, as well as when there are cracks

or breaks in the graphene coating even in epitaxially grown graphene,[83] increasing the importance of knowing how the water will change the graphene-substrate interactions.

Theoretical studies of water between graphene and SiO_2 has shown that the water decreases the adhesion energy between the graphene and substrate, as does hydroxylation of the SiO_2 surface.[84] The impact of the substrate-graphene interaction is also observed in the ability of water to split the graphene and then intercalate, with graphene epitaxially grown on Cu splitting much less effectively than graphene epitaxially grown on Ru.[85] While water can be trapped between the surface and graphene, it can also be trapped between the layers of graphene sheets. To date there has not been a study of water intercalated between the layers of the graphene and its effect on the frictional properties. Under high temperatures water can intercalate between the layers, so the resulting effect of water between graphene layers could have a large impact on device and lubricant applications.[86] This effect of trapped water between graphitic sheets or between graphitic material and the substrate is therefore an important one and one that has yet to be fully studied.

Aside from pristine mono- and multi-layered graphene, modified graphenes, such as graphene oxide and fluorinated graphene, have also been investigated for their lubricating properties.[87] Graphene oxide has been studied in particular due to its water solubility. This solubility can be used to contribute in two ways: one is using GO as a water-based lubricant additive, and the second is using the water solubility for placement of the GO on difficult surfaces such as on MEMS and NEMS. In both uses, GO has shown to decrease the observed wear to the surface, and in the case of using it as a

water-based additive, a coefficient of friction of about 0.05 was found.[88,89] GO can be subsequently reduced as well, with reduced graphene oxide (RGO) also showing reduced friction and wear resistance, with the measured friction coefficient on bare Si of 0.23, reduced from a Si/SiO_2 coefficient of friction of 2.65.[90] By using oxidized graphene or top layer oxidized graphite as a lubricant, the oxygen moieties can be directly reacted with the substrate while still maintaining their lubrication properties for the system.

Beside the pure frictional response, the mechanical properties of interest also include the Young's elastic modulus, 2.4 ± 0.4 TPa for single layer and 2.0 ± 0.5 TPa for bilayer,[91] which along with the out-of-plane bending and impermeability of gases allows for blisters and bubbles to form. These bubbles have been observed both naturally from liquid or air getting trapped when placed on the substrate, and also have been created by controlling and changing the pressure around suspended graphene.[92,93] Even graphene that has been epitaxially grown on SiC has been observed to have intrinsic bubbles or domes due to either defects, step bunching in the SiC substrate or from Si nano-droplets or nano-pillars.[94] Pristine graphene has such a small hole in the rings that no gas, not even H_2 is able to pass through; therefore by controlling the defects, graphene has been able to serve as a selective filter.[95,96] Bubbles can serve for more than just gas barriers; the curvature brought about by the bubbles presents novel functions such as: increased reactivity at the curved regions,[97] optical lenses,[92] and sites for reaction chemistry inside the bubbles.[98] While graphene itself is fairly inert, when curvature is introduced to the graphene the bonds become more amenable to reactions, so by creating graphene

bubbles the curved regions can be selectively reacted.[99,100] Giem and co-workers theorized that these graphene bubbles that formed with graphene on supported surfaces, for which they could alter the height of by changing the gate voltage, could be used for optical lenses.[92] Lim and co-workers also showed that nanobubbles could also be formed on diamond, by utilizing the mismatch between diamond and graphene.[101] It was then subsequently found that by altering the conditions at which the graphene was placed on the diamond, different solvents and molecules of interest could be encased in the nanobubbles, and upon heating, high pressure-high temperature conditions could be formed that would allow for reactions inside the bubble to occur, that were otherwise not stable under ambient conditions.[98] Moreover, since graphene itself is optically transparent, this allowed for the conditions inside of the bubble to be probed via techniques such as infrared spectroscopy.[102]

These findings thus far demonstrate that graphene bubbles can either happen by chance or in a planned method with manipulation of pressure conditions. The graphene on diamond technique shows the formation of nanobubbles in a fashion that was not specifically confined to a previous template but ensured the materialization instead of relying on chance.[101] In this thesis, a new way of developing bubbles between a graphitic region and its substrate in a more semi-controlled manner will be discussed. The control garnered from this method allows for more selective studies of bubbles generated with more than single layer graphene and on the same platform as non-bubbled regions.

1.6 Modification of Graphitic Materials by Oxidation

Precise control of functionalization of graphene is of interest for modifying the electronic, mechanical and chemical properties. Oxidation of graphene and graphite in particular have been studied extensively as a means to adjust the pristine graphene and graphite properties. Hummers and Offeman published a method of preparing graphitic oxide in 1958,[103] and their work and the subsequent modified Hummers' method(s) have been of great use especially since the isolation of graphene.[104] It has been found that as the extent of oxidation increases, so do the changes in the properties of the new graphitic oxide material. Further work has been done to find ways to put graphitic oxide to use such as, synthesizing and fabricating graphene oxide fibers, papers and films which can be applied in areas like electronics with field effect transistors,[105] biomedical applications,[106] and lubrication.[88,89] One of the important properties that graphene oxide brings to the table is that it changes the water contact angle from graphene's 87°-127° to a water dispersible level of about 30°-60°, which as mentioned before, allows for a sometimes easier method for placement of the graphitic material.[107] As discussed above, in many electronic applications it is necessary to open the band gap, and first principals calculations conducted examining the effects of hydroxyl and epoxide functional groups on single layer graphene estimated a local band gap opening from a few tenths of an eV to ~ 4 eV depending on extent of oxidation and location.[108] GO experiences three factors that alter its conductivity: the breaking of the graphene structure opens the band gap; the presence of oxidized species effectively remove electrons from the conductive π system, thus lowering the number of charge carriers; and large amounts of these

oxidized species also introduce deformation to the structure as the π-system is broken, and as graphene oxide is not flat, this introduces scattering sites. There have been limited studies on the exact values for band gap opening with graphene oxide in part because the extent of graphene oxide and the identity of the materials and associated surface bound species is greatly dependent upon the conditions of the oxidation.[109]

GO shows many possible uses, but the wet chemistry oxidation has many drawbacks. Hummers' method requires hours to days for the reaction, harsh conditions and, like most other oxidizing methods, does not have any control for the location and limited control on the extent of the oxidation. Also, even though Hummers' method was first described in 1958, it was only in 2014 that a mechanism for how the oxidation process works was reported.[110] In order to create more complex devices, have more tailored devices and to better understand the basic roles that oxidation has on graphitic materials, a better template for oxidation is required.

This is where the atomic force microscope (AFM) can start to impact the GO field. The AFM was invented in 1986 and is a tool for probing and studying the surface and its interactions with the AFM probe tip, which can be done under different environmental conditions.[111] The AFM contact mode set up can be modified such that a bias can be applied between the probe tip and sample, and this current or electric field can drive chemical reactions, such as oxidation.[112] Oxidation created by biased AFM can be studied in contact mode so that changes in topography and friction can be monitored immediately after the reaction, giving direct feedback to the extent and

locations of the oxidation. Coupling the biased AFM set up and graphitic surfaces, a proper examination of the effect of oxidation can be conducted.

Local functionalization is the key to understanding the effect that the modified region has on the graphitic structure in a direct and comparative manner. There are many types of local functionalization and several that involve AFM, such as nanoshaving, nanographting, and dip-pen lithography.[113] Another such method is local anodic oxidation (LAO), which chemically reacts the surface under the tip and was first reported in 1990.[114] In this process, also known as bias lithography, the oxidation is conducted by applying a potential between a metalized tip and a conductive or semi-conductive substrate which creates a localized electric field. This electric field in the presence of a humid environment drives the oxidation reaction under the water meniscus. Bias lithography on graphitic materials breaks open the π system and introduces new moieties such as hydroxides, epoxides and carboxylates. Since this method utilizes an atomic force microscope, where the applied bias can be controlled spatially on the nanoscale (limited predominately by the tip dimensions), it gives precise control on where the reaction is occurring and also allows for changing the conditions in one experimental set up. There are many factors that affect the lithography including: tip size, humidity, pattern size, tip speed, applied force and others. LAO by AFM has been applied for use in cutting through graphitic layers[115] and for controlled local oxidation.[116,117] Park and co-workers explored the frictional change induced by oxidizing graphene by bias lithography connected by gold contacts and found a 7-fold increase

compared to the pristine graphene.[87] This helps to elucidate the type of mechanical response that can then be expected with oxidized graphitic surfaces.

1.7 Monitoring the Surface of Graphitic Samples

While functionalization is a means of altering graphitic material properties, the identities of these new surfaces must be characterized as the type and extent of modification are important factors. X-ray photoelectron spectroscopy (XPS) and Raman spectroscopy are the two most commonly used techniques for graphitic samples due to the extensive information they yield and their non-destructive methods.[118,119] In the cases of large scale, homogenous modifications to graphite, XPS identifies the type of defects and the relative amounts thereof. XPS is a surface sensitive technique, which is ideal for monitoring the changes of the chemical nature of the top of graphitic surfaces. In XPS it is the binding energy of the photo-ejected electrons that is detected after an X-ray beam irradiates the surface and uniquely identifies the chemical element and its local electronic environment. When functionalizing graphene, XPS can provide the chemical confirmation of the functionalization and change in the conjugation of the graphitic structure as well as the relative concentration of the different moieties.[120] Both the type and extent of functionalization are important to monitor when using functionalization to modify electronic and mechanical properties for understanding the cause of the change in properties as well as for allowing for reproduction of the samples.[47] This is an important non-destructive means of obtaining true chemical information about the surfaces created, though it works best on larger areas of homogenous functionalization.

Another non-destructive tool frequently used when studying graphitic surfaces is Raman spectroscopy, which measures the inelastic scattering of light from the sample and can be used to look at smaller scale modifications that are not homogeneous. Unlike with XPS, Raman spectroscopy does not provide elemental specificity, but serves two important broad purposes: the monitoring of changes induced in the surface by defects or chemical changes, and the identification of single layer graphene versus bilayer graphene versus few layer and graphite-like surfaces. This means that to identify and study truly single layer graphene, the surface can be quickly probed with Raman spectroscopy instead of needing other more time consuming methods such as AFM. The spectroscopy of graphite has been studied beginning well before the isolation of graphene,[121,122] and with the advent of graphene, more work has been conducted, allowing for more conclusions to be made solely on the observed Raman spectra.[123,124] In Figure 1.6* the first order Raman modes, the G mode occurring around 1575 cm^{-1} and the breathing mode, or D mode, occurring around 1350 cm^{-1} are depicted. In pristine graphene, the G mode is the only first order mode visible, but as pristine graphite or graphene incurs defects, the Raman signal changes, with peak broadening and the introduction of the D band, which is symmetry forbidden and thus only allowed when the π lattice is broken.[125] There are also several second order modes observed in the Raman spectra: the G* mode at 2450 cm^{-1}, the 2D mode at 2650 cm^{-1} and, when defects are present, the D+G mode close to 2960 cm^{-1}.[94] For low concentration of defects the average distance between defects can be calculated based on the formula of Lucchese and coworkers:

$$\frac{I_D}{I_G} = \frac{102 \pm 2}{L_D^2},$$

where I_D/I_G is the intensity of the D to G peaks and L_D is the average defect separation, which is based on the Tuinstra and Koenig ratio.[123] The Raman signal is also sensitive to the substrate effects due to the interactions of the graphene with the substrate, with peak shifts for graphene and few layer graphene occurring on different substrates.[126-128] Thus Raman spectroscopy is a leading force in exploring graphitic systems and monitoring their changes.

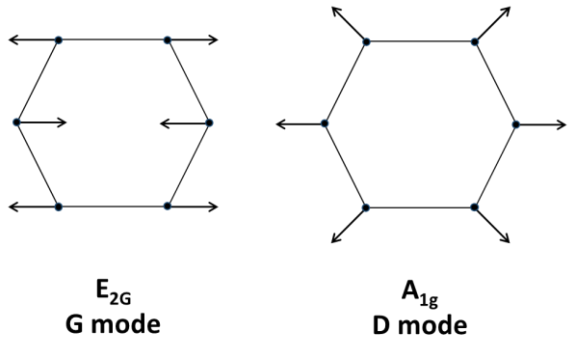

Figure 1.6 Raman modes for graphene and defect graphene.

Raman can serve in greater roles than just identifying and monitoring the purity of graphitic devices; it can become involved in the devices for analytical purposes as well. Already Raman spectroscopy has been used in conjunction with surface enhanced graphene devices for chemically identifying trace levels of molecules such as explosives.[129] There is also further work coupling graphene with gold nanoparticles on a

gold substrate which shows that at the three-way junction, there is about 50-70 times stronger electromagnetic field contributions, which is what gives the increased Raman signal.[130] This opens up Raman spectroscopy to not just identifying and monitoring the condition of the graphitic materials, but to being able to serve as an important addition to the graphene devices and their studies.

1.8 Goals of the Work in This Thesis

As more is learned about graphene the number of possible applications increases. Pristine graphitic materials however pose some problems with their lack of band gap and low chemical reactivity. Thus studying new modified graphitic materials can help lead to even more uses. Oxidation of graphitic matter addresses both the lack of band gap and low chemical reactivity by disrupting the π-system and introducing new reactive moieties. In this work two different oxidation methods are studied, oxidation by UV/O_3 exposure and by biased AFM. The resulting new structures and properties of the oxidized graphite and supported graphitic materials were then studied by AFM and Raman spectroscopy. The goal of this work is to further expand the knowledge of graphitic materials, specifically graphitic oxide and bubbled structures in order to learn more about the properties of these materials and lead to their future implementation as new platforms for device development.

CHAPTER II

METHODS

2.1 Experiment Overview

For the experiments conducted on graphite, purchased HOPG was used for the sample. The supported graphitic materials however, had to be created in a much more complex manner, requiring days per batch. First the supported samples necessitated the creation of a 90 nm thermally grown SiO_2 layer on a Si(100) wafer, onto which the graphitic material was then transferred, and examined to determine the size, quality and number of layers transferred. Both graphite and supported graphitic samples underwent at least one method for oxidation either biased lithography or UV/O_3 exposure. The modified samples were then investigated with many techniques, such as AFM imaging and force-distance spectroscopy, optical microscopy changes as a function of heating, Raman micro-spectroscopy and X-ray photoelectron spectroscopy.

2.2 Graphite Samples

Two different graphite samples were used from two different companies, both of high quality. The first HOPG came from SPI with a grade similar to ZYA, the highest grade, and a mosaic spread of 0.4 ± 0.1 degrees. The other HOPG sample came from NT-MDT KTEK of ZYB grade, the second highest grade of graphite, with a reported mosaic spread of 0.8-1.2 degrees. Both graphitic samples were kept in a dry box when not in use and freshly peeled before each experiment. These HOPG samples were used

for both the graphite studies and as the source of graphite for the supported graphitic materials studies.

2.3 Preparation of 90 nm Thermal Oxide (SiO_2) on Si(100)

To readily observe the deposition of graphitic samples on SiO_2, first the desired oxide thickness on a Si(100) sample must be created. In the beginning of the graphene revolution 300 nm SiO_2 films were used as it was found to have the desired optical contrast that makes graphene distinguishable via optical microscopy.[7] Later it was found that 90 nm oxide would also work and provide for slightly better detection due to even higher optical contrast and has therefore become the new standard in graphene studies.[131] To make the 90 nm SiO_2 substrate, approximately 1 cm by 2 cm rectangles were cut from a highly phosphorus doped Si(100) wafer (Virginia Semiconductor Inc.) with a resistance of 1-3 Ω*cm. The wafers were then placed in a slide holder and sonicated in isopropyl alcohol (Sigma Aldrich) for 20 minutes. Following the sonication was a long rinsing with the ultrapure water (18.2 MΩ·cm), obtained by the purification from distilled water by a NANOpure Diamond system (Barnstead). The samples were then placed in an acid piranha, a 3:1:1 mixture of water, sulfuric acid, and 30 % hydrogen peroxide solution that was in a hot water bath at about 80°C for 20 minutes. After rinsing with copious amounts of ultrapure water again the silicon pieces were placed in a base piranha, consisting of a 4:1:1 mixture of water, ammonium hydroxide and 30% hydrogen peroxide, also at around 80°C, for 20 minutes. Next the samples were again rinsed with copious amounts of ultrapure water and dried under streaming N_2. The dried samples were placed in a kiln and heated to 1050°C to for 1 hour and 23 minutes to grow

the 90 nm oxide layer. The thickness of the film can de deduced optically, and a 90 nm silicon oxide layer is purple in color compared to the shiny gray of the native silicon surface, as shown in Figure 2.1. To confirm the oxide thickness by the color, the wafer held at a 45° angle and was compared to the color chart obtained from Brigham Young University's cleanroom website in the 90 nm range at a 45° angle.[132]

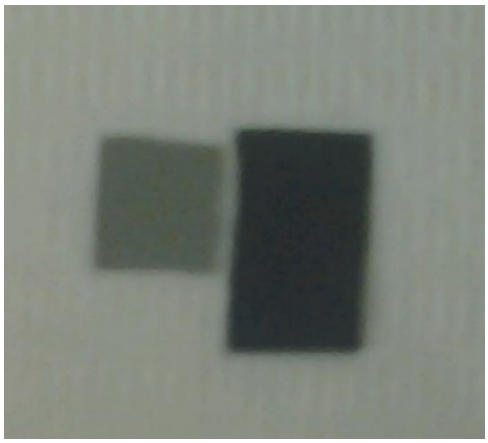

Figure 2.1 The color change from Si (left) to 90 nm SiO_2 (right).

2.4 Placing Graphene on 90 nm SiO_2

Once a 90 nm SiO_2 sample was created, graphitic layers could be physically transferred onto the substrate. To explore modifications of the Scotch tape method, three tapes and three methods used to create these mechanically exfoliated surfaces were examined: 1) Scotch tape as a reference, 2) a water soluble tape and 3) a thermal release tape. Each of the tapes had a unique process for removal, but all began with a freshly cleaved highly oriented pyrolytic graphite surface produced by a Scotch tape (3M) peel.

A freshly cleaved surface is integral in the process as studies have shown that over a short period of time (less than a minute), atmospheric contaminants on the HOPG surface can alter the graphitic properties such as the observed increase in the hydrophobic nature.[133,134]

For the Scotch tape (3M) transferred samples, the process began with a fresh, long piece of tape that was cut and used to peel the graphite once and then self-peeled about 3 more times. The tape was then pressed onto the prepared 90 nm SiO_2 surface and rubbed down with plastic tweezers before peeling off, leaving graphitic material behind. By self-peeling, the number of layers of graphite on the tape was nominally halved with each peel, with the intention of increasing the amount of single layer graphene areas transferred when placed onto the SiO_2 substrates.

Water soluble tape studies were conducted with water soluble wave solder tape (3M), which has a poly-vinyl alcohol backing and a water soluble synthetic adhesive. An approximate 1 cm by 1 cm piece of the tape was used to peel the HOPG and place it on the SiO_2 surface. Once the tape with graphite was on the surface it was rubbed down with plastic tweezers and then immediately held in hot water at ~ 80°C and stirred for 5 minutes to 20 minutes. After the majority of the tape was observed to have dissolved, the sample was removed from the water bath, run under copious amounts of ultrapure water, and dried with N_2. Only as much tape as was needed to peel the graphite was used and the HOPG was a 1 cm by 1 cm sample, therefore the 1 cm by 1 cm piece of tape was used. The amount of tape was limited as the tape itself dissolves into the water

and it was desired to remove the tape as quickly as possible with the least amount of contamination to the surface.

The last mechanical exfoliation method used was the thermal release tape (Graphene Supermarket). A piece of the thermal release tape was cut and placed on the HOPG. After rubbing it down with plastic tweezers, the graphite was then peeled and placed on the 90 nm SiO_2. Pressure was applied again with tweezers to the thermal release tape to the surface and the sample. Like with the water soluble tape, the tape was not peeled off, but this time, with the tape still attached, the sample was placed on a heated hot plate. As the sample warmed up the tape turned white and peeled off on its own around 100°C. The subsequent samples had a large amount of graphite left on the substrate. The samples were then quickly re-peeled with Scotch tape by simply pressing and peeling a single time, which removed a large amount of the graphite. This was done in order to increase the amount of fewer layer graphene and single layer graphene present.

2.5 Atomic Force Microscopy (AFM) Studies

Atomic force microscopy (AFM) was used both for its ability to study the surface properties such as friction and topography and also to drive the localized chemical reactions on the samples. There were two AFMs used in these studies: an Agilent 5500 Atomic Force Microscope and a WiTec Confocal Atomic Force Microscope. The small scan studies (those less than 10 microns in size) and the bulk of the biased oxidation were conducted by the Agilent 5500 AFM, while larger scale studies and Raman micro-spectroscopy studies (which will be discussed later) were performed on the WiTec AFM.

The atomic force microscope, which was invented in 1986,[111] is modified after the scanning tunneling microscope (STM). Unlike the STM, the AFM works on both conductive and non-conductive substrates and can provide true height information. The AFM works by directly probing a surface with a tip and raster scanning the surface. The interaction between the tip and the surface is monitored by a laser that is deflected off the back of a reflective cantilever to a split position sensitive photo-diode detector as depicted in Figure 2.2. On the front of the cantilever is a tip which, in the studies described here was typically metallic (Pt/Ir) and sharp (ca. 20 nm radius of curvature), although there are also carbon nanotube tips, colloidal probes, and organically modified tips, among others Si and Si_3N_4 tips are the most common however, and most metallic tips are formed by coating metals onto these materials.

Which tip is used depends on what mode will be used and what type of interactions are being investigated. As the tip scans across the surface, the change in the reflectance results in a change in the reading of the detector that is then sent to create the image and to the feedback loop. The horizontal changes in deflection come from the twisting of the cantilever and the vertical changes from the bending of the cantilever. These deflections lead to changes in photocurrent, which leads to the 3-dimensional information and images. The signal also goes to the feedback loop which analyzes the change in the detector, determines the corrections and next moves needed for the tip location and sends commands to the tip piezoelectric controls.

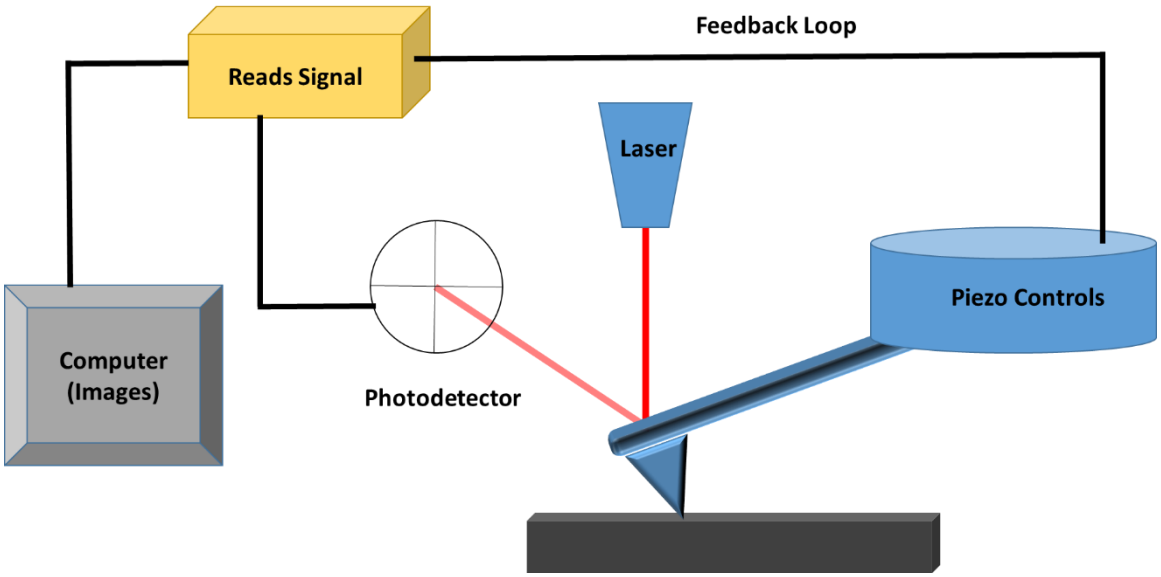

Figure 2.2 Atomic force microscope set up.

There are different modes of AFM, with the two main methods being contact mode and tapping mode. In contact mode, the probe and sample are brought into direct contact, and as the tip scans, it twists and bends in response to the friction and topographical properties of the surface. Friction is measured from the lateral twisting of the cantilever, while the topography is measured from the upward and downward bending of the cantilever due to changes in the surface features. In contact mode, the deflection is kept constant as the scanning occurs, with the constant lever deflection maintained by the feedback loop. In tapping mode, also known as alternating current mode or AC mode, the tip is resonated at or near its resonant frequency and then brought into intermittent contact with the surface, with the feedback loop maintaining a constant amplitude. Once initial contact has been made, the tip is scanned across the surface

while still resonating. As the tip interacts with the surface, the resonance frequency can be changed due to the forces between the tip and sample. Monitoring the phase shift of the measured frequency from the applied frequency allows for the phase mapping. Thus tapping mode yields both topography and phase imaging. Whether tapping mode or contact mode will yield more informative images depends on the interactions that are desired to be measured (such as friction versus phase), and the sample topography (as the tip will interact with flat versus large fluctuations differently).

Depending on the studies being conducted, the amount of control over how dry or humid the scanning conditions are while conducting AFM can have a significant influence on the images and forces measured. To meet this need, a custom set-up was created for the Agilent 5500 which was already equipped with a glass enclosed scanning system. The set-up is composed of a nitrogen tank attached to tubing that branches with valves so that the flow of the dry gas can either go directly into the AFM chamber or can be redirected to bubble through water before passing into the AFM chamber. The humidity was measured via tubing that left from the AFM chamber to a hygrometer, with the whole set up pictured in Figure 2.3. By tuning the flow through these two branches and the initial flow from the N_2 tank, the humidity was able to be controlled to within about 5% of the desired humidity.

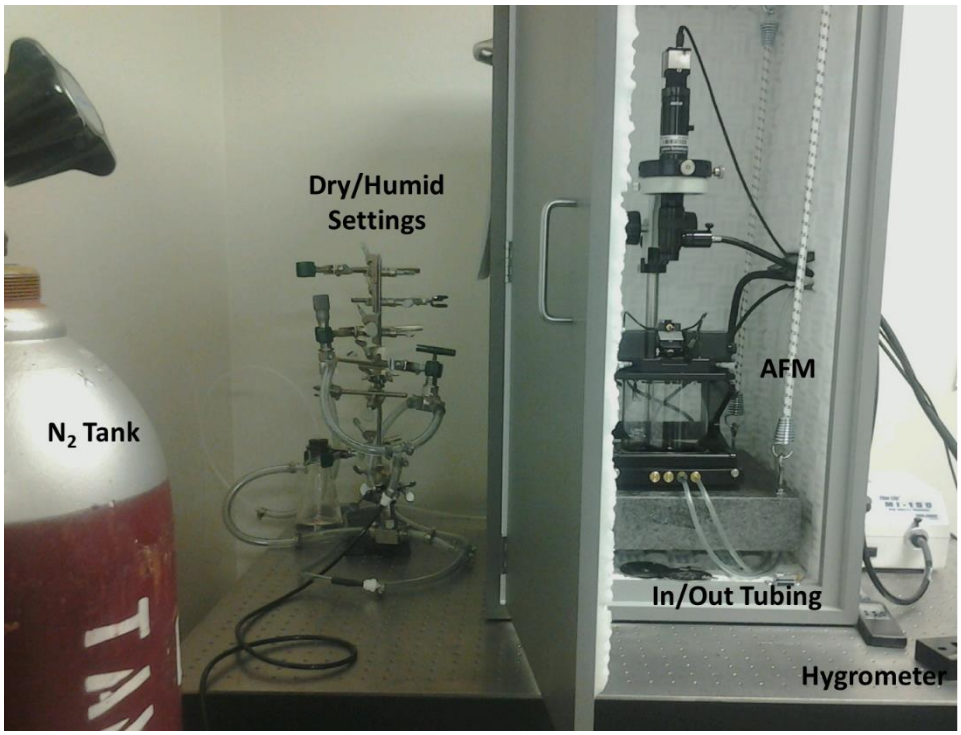

Figure 2.3 Humidity controls for the Agilent AFM.

As AFM measures the interaction forces of the sample and tip, the type of tip used is very important. In general typical contact mode tips have a low spring constant, whereas tapping mode tips usually have a higher spring constant and higher resonance frequency. There were several tips used in the experiments conducted in this work in contact mode, including SCM PIC (Bruker), CSC37/AlBS (MikroMasch), and MSCT (Bruker). SCM PIC are Pt/Ir coated n-doped silicon tips with only one cantilever per chip and a reported spring constant of 0.2 N/m. The average tip radius of a new Pt/Ir tip was measured to be ~ 26 nm, and the radius of the tip after use for lithography and imaging was found to have increased to an average of 36 nm. The CSC37 chip has 3 cantilevers made from an n-doped silicon with an aluminum backside coating which

vary in length (and thus spring constant), with average spring constants of 0.3 N/m to 0.8 N/m. The typical resonance frequencies for each cantilever ranges from ~ 20 kHz - 40 kHz.[135] The average radius of CSC37 cantilever B, which was isolated by manually removing the other two cantilevers and used in the studies, was ~ 24 nm. Finally the MSCT tips are made from silicon nitride with Ti/Au backside coating and are the sharpest with six different cantilevers, two of which are rectangular and four of which are triangular. Their spring constants range from 0.010 N/m to 0.10 N/m with resonance frequencies ranging from 4 kHz - 160 kHz. For tapping mode, another silicon based tip with aluminum backside coating was obtained from Vista Probe. Its spring constant was about 48 N/m with a resonance frequency of about 190 kHz.

2.6 High Resolution Scanning

The graphene atomic lattice itself can be observed with an AFM by carrying out high resolution imaging. The graphite lattice was first reported in 1987 by imaging graphite with a tungsten tip at a low load.[136] Graphene has a periodic lattice, and it is the stick-slip motion of the tip as it rasters over the surface that allows for the atomic scale features to be observed in the friction images. To obtain high resolution images of the graphite and oxidized graphite, a CSC37 tip was used. A low load was used while scanning at a high speed (32 nm/s) with a small set z-range. The feedback loop settings were adjusted to maximize the lateral force signal until the scan started to show the periodic lattice in the friction images.

2.7 Biased Lithography by AFM

It was found in 1992 that by using a metallic tip and applying a potential, nanometer-scale lithography could be accomplished with the AFM.[112] In 1994 this method was extended to the fabrication of new structures on silicon substrates.[137] Biased lithography works by applying a potential between the tip and the substrate, typically using the water meniscus as a source of oxygen to oxidize the surface. By switching the current direction, the type of redox reaction occurring on the graphitic material can be reversed. Thus a positive (sample) voltage yields oxidation while a negative voltage yields hydrogenation, though it was found that the absolute value of the potential had to be higher for hydrogenation of graphene than for the oxidation.[138] In these studies, biased lithography by AFM was conducted on graphite by the directly flowing current, and on supported graphitic materials on a Si/SiO_2 substrate, induced by the local high electric field. The biased lithography method is based on contact mode AFM, but with a separate, connected electronic set up. One necessary change is that the tip must be conductive; in this case the SCM PIC Pt/Ir coated n-doped Si tips were used. These tips were connected either to the built-in bias nose with the Agilent 5500 or by connecting the wires manually from the tip to a standalone power supply with the WiTec, as shown in Figure 2.4. In both configurations, the tip was then brought into contact with the surface and the area was scanned in contact mode. Then, after choosing the tip speed, force, pattern and bias, the tip location and movement under applied bias was used to conduct the lithography. After patterning the area could be re-imaged under 0 bias to monitor what, if any, changes occurred. For the graphitic samples supported on

90 nm SiO_2/doped Si substrate, a modification had to be made as there was too much resistance with the SiO_2 surface to have a flow of electricity. Thus the top of the substrate was scratched to the underlying highly doped Si to which the metallic wire was attached, thus completing the connection. When the electric potential was applied, a field was created between the substrate and the tip which allowed for the attempt at oxidation to occur.

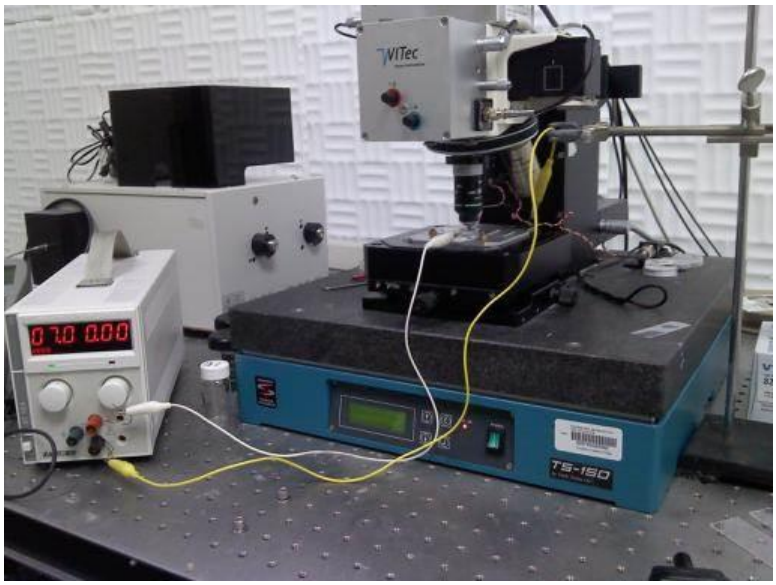

Figure 2.4 WiTec biased lithography set up with external power supply.

Due to their different configurations, HOPG samples and supported graphitic materials required different experimental conditions for ideal oxidation conditions. On the HOPG, as it is a conductive material, the reaction is driven by the electric current and therefore requires less of an applied potential. Supported graphitic materials, on the

other hand, relied on the electric field created and thus did not oxidize at the low bias levels. The exact ideal conditions depended on many factors, but the general bias settings for the HOPG in this work ranged from about 2 V up to 6 V, whereas the oxidation of the supported materials in this work had biases starting at about 6 V and going to the maximum allowed by the equipment of 10 V. Typical speeds for the tip when moving to conduct the lithography ranged from 0.01 microns/s to 1.00 microns/s. Humidity conditions ranged from the natural humidity (typically 45 % RH), but went as low as 24%, to over 80%, while room temperature was maintained at 21°C.

2.8 AFM Tip Characterization

The imaging and oxidation results from the AFM greatly depend on the characteristics of the tips themselves, not just on their composition. Therefore, the tips were characterized on the Agilent 5500 for their spring constant, radius and lateral force constant. These three characteristics have a strong influence on how the tip interacts with the surface for scanning purposes, force-distance plots and lithographic functions.

The Sader method for rectangular AFM tips was used for determining the spring constant of the tips based on the resonance frequency.[139] The Pt/Ir and CSC37 tips were mounted on the tapping mode nose cone and AC tuning was conducted. The data was then analyzed using Fityk, a program that assists in nonlinear curve fitting,[140] to get the quality factor, Q_f, and frequency, w_f. Using these values and the manufacturer's stated width, b, and length, L, of the cantilever, Sader's calibration for rectangular cantilevers was used to find the spring constant. The Sader equation is:

$$k = 0.1906 p_f b^2 L Q_f \Gamma_i(w_f) w_f^2 \,, \qquad (1)$$

where k is the spring constant, p_f is the density of the fluid, and Γ_i is the imaginary component of the hydrodynamic function.[139]

In 1993 Sheiko and co-workers reported using strontium titanate standards as a means to evaluate the tips, such that the deconvolution of the tip shape can be achieved.[141] Based on their studies, strontium titanate was used to find the tip radius of various tips. First the strontium titanate was cleaned by rising with ethanol then exposed to UV/O_3 for 1 minute. This was followed by another rinsing with ethanol and finally the strontium titanate was dried under a stream of nitrogen. The tip to be analyzed was then brought into close contact with the mounted strontium titanate and allowed to stabilize as the environment was pumped with N_2 gas to bring the humidity to 0%. The images were obtained by using a tight z range on a 250 nm square scan at 1.44 microns/s and 512 points/line. Scanning Probe Image Processor software from Image Metrology was used to calculate the tip radius based on the topography images from the AFM. At least 6 images were analyzed and averaged in order to determine the individual tip radii.

Because the friction is a result of the tip twisting in the lateral direction, the properties of each tip must be examined for their later force calibration. The method used in this research was based on Asay and co-workers work improving upon the direct force balance method.[142] A TGF11 standard (MikroMasch), which is a silicon substrate with etched trapezoid steps, was first rinsed with ethanol then dried under nitrogen to ensure a clean surface before being set up for scanning on the Agilent 5500. Scans of either 8x8 microns or 9x9 microns were conducted. The standard has five different regions, as shown in Figure 2.5 that were fit in the middle of the scan range, the light

blue box in Figure 2.5. At least 5 force-distance curves were performed on each of the regions of the surface. This method measured the force-distance curves on both flat regions (as the top and bottom would represent) and force-distance curves on the two different sloped regions with angles of 54.7°, Θ_1, and -54.7°, Θ_3, with respect to the flat top region. The lateral calibration factor, S_L, was obtained by using the equation:

$$S_L = \frac{k_N[\tan(\theta_1) - tan(\theta_3)]}{(\Delta L_1^{Average} - \Delta L_3^{Average})}, \quad (2)$$

where k_N is the normal spring constant, ΔL_1 and ΔL_3 are the lateral sensitivity (V/m) from the force-distance curves for slopes 1 and 3 respectively.[142]

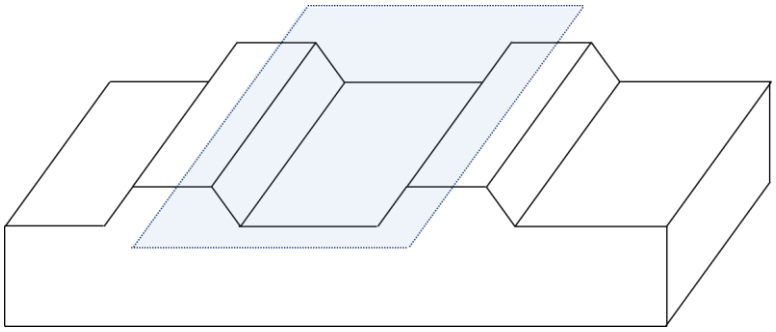

Figure 2.5 TGF11 Series Standard for tip characterization where the blue box is the region scanned for analysis with the AFM.

2.9 Force-Distance Spectroscopy

It was found that after biased lithography on the graphitic materials deposited using water soluble tape had been attempted, graphitic bubbles had formed. One way that these graphitic bubbles were inspected was by measuring force-distance spectroscopy with the Agilent 5500. Force-distance spectroscopy probes the measured

force between the tip and the sample versus the distance between the tip and sample. The AFM tip is driven along the vertical axis towards the sample with the displacement and change in deflection being measured. As the force-distance measurements were conducted after bias lithography attempts, they were carried out with the SCM Pt/Ir tips. The force-distance curves were taken on large bubbles, on areas with small bubbles, on graphite that had not undergone any oxidation and showed no bubbles, and on the SiO_2 substrate.

2.10 Heating of Graphitic Bubbles

Another way that graphitic bubbles were investigated to help determine their identity was that one of the samples was placed on a heating stage and heated while monitoring the optical images. The sample was placed on a Lake Shore 321 Autotuning Temperature Controller heating stage (Westerville, Ohio) which was then loaded onto the WiTec microscope. A 100x objective was used to bring the graphitic samples into focus and optical images were taken before heating, during each heating step, and during the cooling process. The heating of the sample was achieved by raising the temperature of the heating by 10°C every 20 minutes starting from room temperature and finishing at 60°C above room temperature. Once the stage was 60°C over room temperature, it was held there for 20 minutes. Then the temperature was lowered, decreasing at the same rate as it was increased. The slow increase of temperature was to allow for the stabilization at the new temperature, especially while the stage was being heated, as the sample was open to ambient conditions. The black and white images that were taken during the process and over the next several days were analyzed using public domain

Image J software (NIH) to track the changes of the cross section of a bubble over the entire process.

2.11 Oxidation by UV/Ozone

A Novascan PSD-UV, equipped with a mercury lamp, was used for both the cleaning of the strontium titanate standard, as mentioned above, and for the large scale oxidation of the HOPG surface. To oxidize the HOPG, a freshly cleaved sample of graphite was placed 5 cm from the light source, and exposed for lengths of time ranging from 5 minutes to 60 minutes. After removing the samples from the UV/ozone chamber, the samples were briefly rinsed with ethanol and dried under a stream of nitrogen gas. The resulting oxidized graphite appeared optically no different after the exposure. To compare the oxidized graphite to pristine HOPG on the same platform, a fresh piece of Scotch tape was used to peel half of the sample. Again, there was no observable visual change in the appearance except for a line where the peel occurred from the graphite breaking at that point as observed in Figure 2.6.

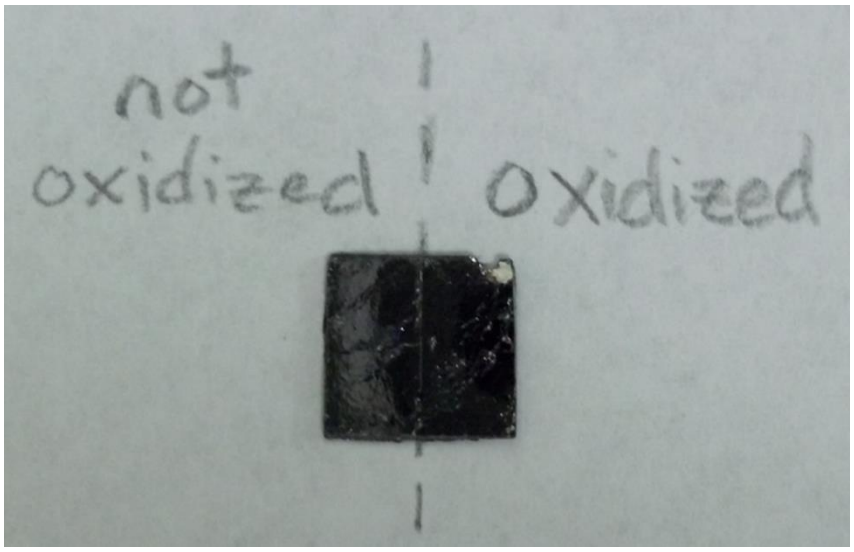

Figure 2.6 HOPG that has been freshly peeled (left) and exposed to UV/O_3 (right).

2.12 Raman Spectroscopy and X-ray Photoelectron Spectrometry

It is important to be able to identify and monitor the changes that occur when modifying graphite. Two non-destructive means of accomplishing this are Raman spectroscopy and X-ray photoelectron spectroscopy (XPS). Raman spectroscopy is the backbone for graphitic characterization as it is able to identify the number of graphitic layers transferred onto a substrate and monitor the samples for defects, after oxidation, for strain, and after bubble formation. It works by focusing a monochromatic light on the surface, which can then undergo inelastic scattering with the material. The resulting photons are then collected and the energy shifts are recorded in units of wavenumbers for the Raman spectrum. All Raman spectroscopic measurements in this work were obtained using a WiTec Confocal Atomic Force Microscope. The light source used was an Argon laser with a wavelength of 488 nm. The laser power used was set to about 1.5

mW, to be high enough for a good signal without being too intense to damage the surface being investigated. Both single spectra Raman and Raman mapping measurement were utilized for analyzing the different surfaces. For the single spectra an average of 20 accumulations were taken with a 0.5 s integration time using a grating of 600 grooves/mm. Raman mapping was conducted with a 0.08 s integration time for a 5x5 μm scan, also using a grating of 600 grooves/mm.

A Kratos Axis Ultra Imaging X-ray photoelectron spectrometer was used for XPS studies. XPS works by irradiating the sample under vacuum with X-rays, in this case from an Al source, and measuring the counts and kinetic energy of the resulting electrons. Pristine HOPG and HOPG that had been oxidized by UV/O_3 for 30 minutes were studied by XPS. An initial survey scan was conducted at 160 eV pass energy to obtain the general spectra. High resolution scans in the C1s and O1s were conducted at a 40 eV pass energy with the O(1s) region being collated with a dwell time of 0.4 s and an average of 4 sweeps, and the C(1s) region with a dwell time of 0.26 s and an average of 3 sweeps. The C(1s) was examined in the 276 eV to 292 eV binding energy range and the O(1s) in the 521 eV to 545 eV binding energy range.

CHAPTER III

LOCAL AND LARGE SCALE OXIDATION OF GRAPHITE

3.1 Overview

Graphite is more than just a source for obtaining the highly popular graphene, it is a material of interest in its own right. Graphite is a 3-dimensional carbon allotrope made up of single sheets of covalently bound honeycomb lattices that are stacked upon one another and held together by van der Waals forces. These graphitic materials have impressive conductive properties, high thermal conductivity, high strength, and a low coefficient of friction.[71,143] It is these properties that make them viable for many applications, such as in writing utensils, solid lubricants,[73] batteries,[3] conductive substrates for STM studies[144] and as a support for TEM.[145]

Graphite has a low chemical reactivity which can make complex device creation difficult, whether one attempts to bind graphite to a substrate or to react it with other species. Chemical modification of graphite increases the number of ways that graphite can be incorporated into a system, introduces chemically reactive moieties for further reactions onto it, and can be used as a platform for graphene studies. With at least one functionalized surface of graphite, the material could be attached to a substrate, and then the graphite could serve as a bound solid lubricant. Graphite in its 3-dimensional form has fewer sample creation difficulties and as such, it is much easier to conduct certain experiments with it while still learning relevant information that can be compared to graphene. The main problem with graphene in its electronic device implementation is

that it has no band gap. To overcome this, controlled functionalization can lead to selective band gap opening for application in systems such as field effect transistors.[50] There are many types of chemical modification such as hydrogenation, fluorination, and oxidation, with each altering the electronic, mechanical and chemical properties.[47,138,146]

Oxidized graphite is of particular interest due to its prevalent history (studies date back to 1859), its relative ease of synthesis (several methods are available), and the range of reactive oxygen groups that it can form.[109] When graphite is oxidized, it is typically via Hummers' method, or a modified form of Hummers' method, which uses potassium permanganate and sulfuric acid, among other chemicals, in harsh reaction conditions.[103,104] These methods allow for large-scale oxidization of the entire graphitic sample in solution but without any control or specification of the oxidation type or location. Thus these methods are great for situations where graphitic oxides are desired for broad use, such as when they are used for placement and then reduced,[16] but are not desired for localized oxidation such as in comparative frictional studies. Hummers' method, modified or not, also naturally exfoliates the graphite as the π-π interactions are disrupted, so the graphite yields graphene oxide (GO) sheets of various sizes and shapes. These single or few layer graphene oxide sheets therefore are not ideal for situations requiring the conductive graphite substrate nor do they yield themselves to a good study of the direct graphite oxide structure. Even these oxidized sheets are found to be a combination of functionalized graphene and surface bound graphene oxide debris which was discovered to alter at least the chemical characterization and electroactivity of the graphene oxide.[147,148] While the chemical and electronic properties have been studied,

there lacks a comprehensive study on the friction properties of the GO created via Hummers' method. These graphitic oxides are not a slight changing of the pristine graphite, but a new material, insulating in nature with many reactive oxygen sites. The mechanism of the oxidation process has only recently been successfully studied as published in 2014 by Dimiev and Tour[110] even though Hummers method was first published back in 1958.[103] The lack of understanding of this process, lack of control, harsh chemical environment, and the hours and days that it can take to fully react show the complications that Hummers' method introduces and how it fails to meet some of the more mild applications that do not require exfoliated, highly oxidized graphitic sheets.

While Hummers' method may be the current model for oxidizing graphite, it is not the only technique. Another method of oxidizing graphitic materials on the large scale is by UV/O_3 exposure. This method uses ozone radicals that bombard the surface and initiate the oxidation process on exposed graphite. This technique is a quick, wide reaching method that does not penetrate to all layers of a graphitic material as Hummers' method would,[149] nor does it involve the natural exfoliation of all the sheets and harsh chemical conditions. UV/O_3 has already been used to oxidize carbon allotropes such as carbon nanotubes,[150] to make graphene field effect transistors,[51] and to develop a sensitive graphene gas sensor.[151] As there is much interest in using graphene for solar cells, it is important to study how the environment could alter the working of the graphene device as both UV radiation and ozone occur naturally in the environment. One way to investigate these possibly harsh conditions is by using lab-based UV/O_3 exposure.[152] Specifically, for a solar cell application, the relation of the resistance of a

graphene film to the extent of oxidation based on UV/O_3 exposure is important as the devices are exposed to the environment for many years. Unsurprisingly it was found that for graphene, as the amount of UV/O_3 exposure time increased so did the resistance.[152] While the mechanism of the O_3 exposure has been theoretically studied on graphene's more reactive nanoribbon edges, with their already broken π-structure,[153] work done investigating the actual mechanism of UV/O_3 on larger area graphene or graphite and the study of the subsequent effect on the friction of graphite or graphene is lacking. Besides the possible application in solar cells, there are other uses that could lead to the exposure of graphitic materials to natural sunlight or to the reactive ozone radical. By studying the physical properties of UV/O_3 oxidized graphite, more can be learned about the stability of graphitic materials under this harsh environment to provide reasonable guidance for graphitic applications.

Both Hummers' method and UV/O_3 oxidation are able to oxidize large scale areas, but both lack the small, controllable patterning that would be ideal for selective reactions and direct studies of the physical properties of oxidized comparted to pristine graphite. It is through biased lithography using an atomic force microscope (AFM) that local studies of graphite oxidation can be conducted.[154] This process provides the patterning of oxidation and then the in-situ study of this modified graphite. Also known as local anodic oxidation (LAO), biased AFM works by creating an electric field at the tip and substrate interface with the use of a conductive tip (typically metal coated) and a conductive or semi-conductive substrate. Because the electric field created is based on the AFM tip location, the movement of the tip can be exploited to design patterns for

where the oxidation occurs on the sample. As these studies are conducted in either an ambient environment or under a controlled increased humidity, a water meniscus s present at the tip, and the oxygen which forms the moieties on the surface comes from this water. The main drawback to biased AFM is that there are many conditions which must be accounted for when attempting the biased lithography. During the lithographic process, the tip speed, humidity, force, tip size, applied potential and connections all impact the reaction.[117] Some of these important factors are easier to control than others. For example, as the experiment proceeds, wear occurring on the tip will broaden it as just a natural consequence of the scanning process, especially when applying a bias or large amount of force. Because all of these factors are dynamic in nature, exact parameters are hard to establish and maintain. This localized and patterned oxidation on graphite not only can serve as a platform for graphene oxide studies, but also allows for studies on the physical properties of the differing extents of oxidation. These oxidized species can be further reacted with other molecules to pattern complex designs for a conductive substrate with complex behavior.

Whichever oxidation method is used, it is important to understand the chemical characteristics and physical properties. The physical and mechanical changes induced by oxidizing the graphite can be studied with AFM. Contact mode scanning conducted after oxidation examines the changes in the topography and friction of the surface. The topographical information is important as this affects the roughness of the surface, which is significant for studying the contact/contact interaction as done wear studies.[155] Just as valuable is the friction information; in the industrial world, high friction is damaging as

it leads to heating, energy loss and can ultimately cause device failure, especially in the cases of small devices such as microelectromechanical systems and nanoelectromechanical systems.[20] As graphite is already used as a solid lubricant, knowing the friction response of the oxidized form can help determine its possible use as a solid lubricant in its own right. The benefit of having the oxygen moieties is that the graphitic material can be reacted to another material. Thus the combination of the solid lubricating properties can be incorporated in complex set ups that require at least one side of graphite to be chemically reactive.

When producing defects in graphite, it is imperative to know the extent of the defects as the properties of the modified material depend on the amount of alteration. Raman spectroscopy allows for the monitoring of the defects on the graphitic surface. Graphite is highly symmetric with a point group symmetry of D_{6h}, but only the $2E_{2g}$ mode should be first-order Raman active in its pristine form.[121] This E_{2g} mode is termed the G band in the Raman spectrum and appears at around 1575 cm^{-1}. When analyzing the Raman spectrum of graphitic samples there is also sometimes a peak about 1350 cm^{-1}; this is the D band, also known as the defect band. This signal allows for the monitoring of how pristine the graphitic material is because the band comes from the A_{1g} mode, which is the breathing motion of the ring. This breathing motion can only occur when the graphitic lattice, and thus the symmetry, is broken. Since the D band comes from defects, the relative intensity of the D band to G band yields information on the extent of defects in a graphitic sample.[122] Thus the D band does not give chemical identification of the defect, but it will appear if the surface has undergone hydrogenation,

fluorination, oxidation, or has lattice defects, among other modifications. Lucchese and coworkers reported a formula that calculates the defect separation for low amounts of defects based on the Tuinstra and Koenig ratio:

$$\frac{I_D}{I_G} = \frac{102 \pm 2\ nm^2}{L_D^2} \quad (3)$$

where I_D/I_G is the intensity of the D to G peaks and L_D is the average defect separation.[123] While this accounts for two of the bands that can be observed in the Raman spectra, there is also a prominent 2D peak, which can be explained as a double resonant scattering peak. Instead of the electron backscattering by a defect (which yields the D band), the 2D band is the backscattering off a second phonon which is why it is around 2650 cm^{-1}.[156] This 2D band can also be used to indicate the modification of graphite, as doped graphite leads to a shift in the band location.[120] When graphitic oxide materials are made via Hummers' method, the rigorous oxidation prevents the Lucchese formula from being used and indeed, the D peak and G peak are typically close in magnitude with a very weak 2D band.[148]

The combination of Raman spectroscopy, which gives the disorder in the system, with X-ray photoelectron spectroscopy (XPS), which indicates as to the identity of the defects, allows for comprehensive monitoring of the chemistry of the graphitic surface in a non-destructive means during these studies.

As substitutes to the harsh Hummers' method are investigated, it is important to monitor the chemical characterization and the physical properties of the surface. UV/O_3 can be used for quick, easy, large scale oxidation, and in this work the exposure time was related to the oxidation extent. Biased lithography was also studied for local

patterning; with this setup the control over the extent of oxidation was monitored while studying the physical properties as the oxidation occurs. These two techniques are important for increasing the means in which to obtain graphite oxide with different desired properties and characteristics. Later these methods can be used to increase the ways in which graphite oxide is applied in ways such as lubrication and as a support system.

3.2 Experimental

High quality highly oriented pyrolytic graphite (HOPG) was purchased from SPI and NT-MDT. These samples were then oxidized by either UV/O_3 or biased lithography.

Large scale oxidation of HOPG was achieved by UV/O_3 exposure. To begin the HOPG was peeled with Scotch tape (3M) for a freshly cleaved surface without the atmospheric contaminants that naturally form on graphite over time and can change its properties.[133,134] The HOPG was then placed in the Novoscan PSD-UV UV/O_3 chamber. The sample was kept 5 cm from the mercury lamp and exposed for different lengths of time. By changing the time of exposure, the extent of oxidation was controlled, with times ranging up to an hour. Once oxidized the sample was immediately removed and rinsed with ethanol and then dried under stream of nitrogen gas. For the studies comparing pristine and oxidized HOPG, part of the surface was then re-peeled with Scotch tape so that the non-oxidized and oxidized surfaces were on the same platform.

An Agilent 5500 atomic force microscope equipped with humidity control was used to conduct the AFM studies. AFM was utilized for localized biased lithography of

graphite samples as well as for the characterization of the surface. To thoroughly characterize the surface, pre- and post-oxidation studies were conducted, obtaining the topography, friction, force-distance curves and high resolution images of the graphite.

For biased lithography by AFM HOPG was placed on a glass slide to electrically isolate the graphite from the AFM plate, and the graphite was then set up for scanning. The graphitic surface was directly connected to the AFM circuit by a metal wire which was pinned down to an edge of the graphitic surface. SCM-PIC Pt/Ir coated n-doped silicon tips with a spring constant given as 0.2 N/m and an averaged initial tip radius of about 35 nm was used for both pre- and post-imaging and the lithography. Before biased lithography was conducted, the area of graphite was scanned so that before and after images could be compared. When biased lithography was conducted, several conditions were controlled including the humidity, bias, force and speed. The typical settings used were a humidity which ranged from 24% to 80%, biases from 2.0-6.0 V, an applied load of 0.1 nN plus adhesion and speeds from 0.01 microns/s to 1.00 micron/s. The modified surface was immediately rescanned in contact mode with the same tip that performed the lithography under typical contact mode conditions. Force-distance curves were taken on the supported graphite while applying a bias, with biases ranging from 0 V to 2.0 V.

Contact mode AFM was also conducted on pristine graphite and the graphite that had undergone UV/O_3. For these AFM studies contact mode CSC37/AlBS (MikroMasch) tips were used to obtain topography and friction images of the surface. High resolution images of 60 minute UV/O_3 oxidized graphite was accomplished with

contact mode settings also using a CSC37 tip. The tip had a spring constant of 0.3 N/m and was scanned at a speed of 32 nm/s with a small set z-range in order to obtain high resolution.

The oxidized and non-oxidized HOPG samples were monitored and chemically characterized by Raman spectroscopy and X-ray photoelectron spectroscopy (XPS).

Raman spectroscopy was conducted using the WiTec Confocal AFM. The light source was an Ar^+ laser (488 nm wavelength) that was focused on the sample through a 100x objective and the inelastic scattering of the photons was measured. Both Raman single spectrum and Raman mapping, which is the spatial mapping of the spectra, were conducted. The Raman single spectrum was obtained by taking the average of 20 spectra taken one right after another with an integration time of 0.5 s and a laser power of about 1.5 mW. Raman mapping had a slightly longer integration time of 0.08 s for a 5x5 micron scan, at the same laser power.

XPS was conducted using a Kratos Axis Ultra Imaging X-ray photoelectron spectrometer with an Al source on both oxidized HOPG (exposed to UV/O_3 for 30 minutes) and a freshly peeled HOPG. The two spectral regions investigated were the O1s and the C1s, the O1s scan had dwell time of 0.4 s and an average of 4 sweeps, and the C1s scan was done with a dwell time of 0.26 s and an average of 3 sweeps.

3.3 Results

Two methods of oxidation were explored to extend the means of creating graphite oxide and studying the properties of the materials made by these techniques. For obtaining the large scale graphite oxidation, the graphite was exposed to UV/O_3 for

various amounts of time. The second method used biased AFM lithography to selectively pattern the oxidation on the graphite, with changing parameters leading to changes in the extent of oxidation.

Instead of oxidizing all the layers in a sample of graphite, UV/O_3 exposure allowed for the large scale oxidation of only the top layers of the graphite. By changing the time of exposure to the UV/O_3, the extent of the oxidation was controlled as monitored by Raman spectroscopy. In Figure 3.1, the different Raman spectra responses are shown; the blue line is from HOPG that had been exposed to UV/O_3 for 30 minutes and the green is from the freshly peeled part of the HOPG sample. The Raman spectra obtained from the freshly peeled graphite demonstrates no sign of defects and has the characteristic pristine graphite peaks for the G band at 1575 cm^{-1} and the 2D band at 2650 cm^{-1}. The UV/O_3 oxidized graphite has those same peaks at the same locations, but it illustrates how the defect peak, D peak, at 1350 cm^{-1} emerges in the oxidized material due to the breaking of the π system. Following the Lucchese equation based on the Tuinstra and Koenig ratio for low defect density,[123] the average distance between defects was calculated to be about 11.7 nm for HOPG that had been oxidized for 30 minutes. A comparison of oxidation time to the intensity of the D/G ratio taken from the Raman single spectrum on the same graphite sample shows a linear trend from freshly peeled to 60 minutes of exposure as shown in Figure 3.2. This indicates a direct relationship between the amount of UV/O_3 exposure and the extent of oxidation. While this direct trend was observed for a specific graphite sample, when other HOPG samples

underwent UV/O_3 exposure, they started with different initial amounts of defects and had different intensities of the peaks based on the quality of the graphite sample.

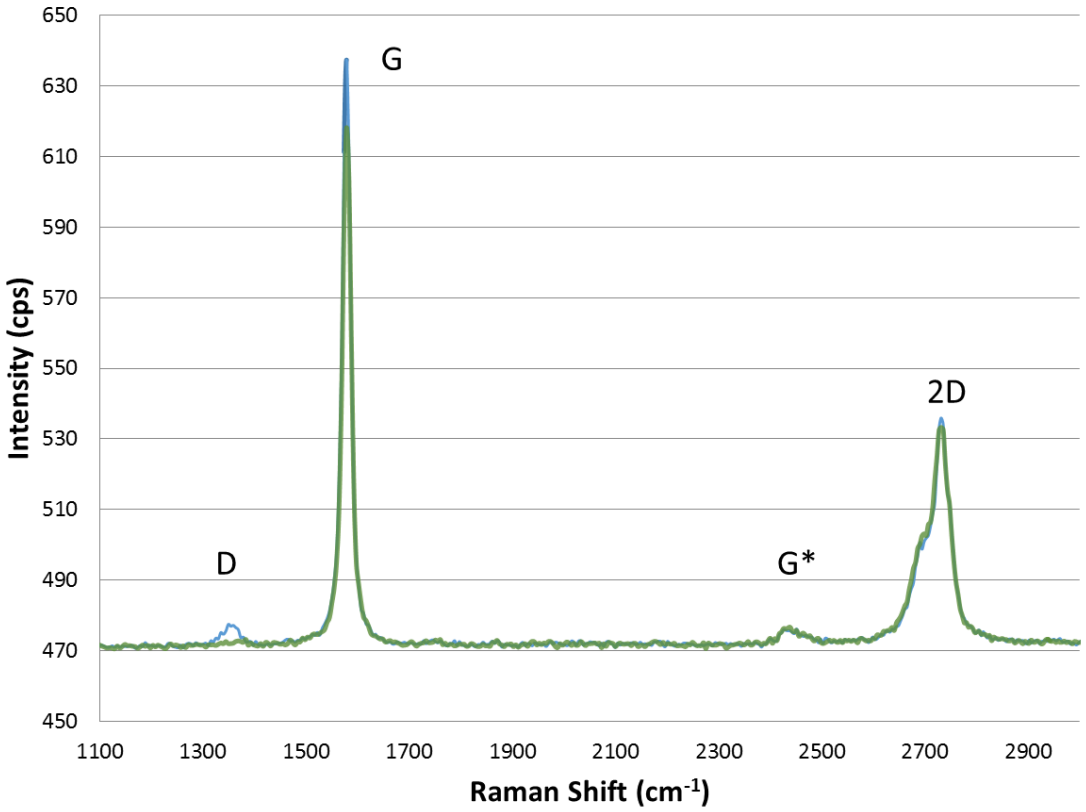

Figure 3.1 Raman spectra for HOPG (green) and UV/O_3 oxidized HOPG (blue).

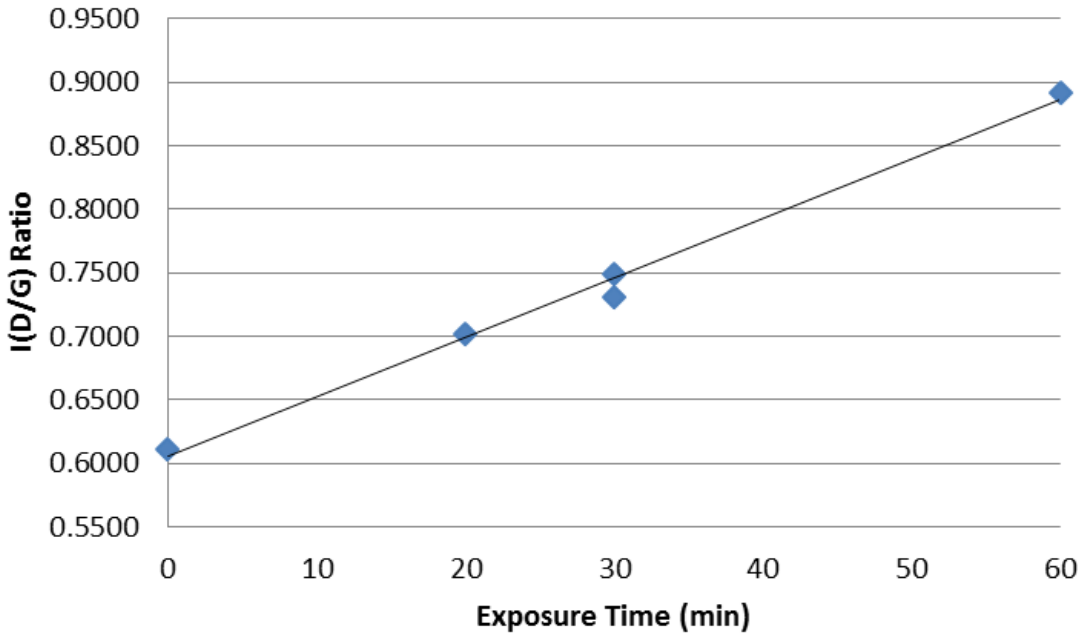

Figure 3.2 Intensity of D/G ratio as a function of exposure time of HOPG to UV/O_3.

Further chemical characterization on how UV/O3 alters the graphitic surface was done by conducting XPS. It was performed on pristine, freshly peeled HOPG and on UV/O_3 oxidized HOPG that had been exposed for 30 minutes in order to determine the identity and extent of defects. The resulting C1s for the pristine HOPG and the partially oxidized HOPG and the O1s for the partially oxidized HOPG are shown in Figure 3.3. In accordance with the literature, the C1s spectrum has a C-C bond with a biding energy of 284 eV,[157] with the measured values for the pristine graphite being measured at 284.55 eV. Comparing this pristine graphite carbon peak to the oxidized carbon peak, the value was found to have moved to 284.65 eV and extends to 284.85 eV; it is a broader peak, with a shoulder at 286.75 eV. This is consistent with the fact that as the

pristine π-system of the graphitic lattice is broken, the peak will broaden and shift. Specifically, when oxygenated species have formed on the graphite and broken the π lattice, they shift the binding energy to higher energies, with C-OH, C=O and O=C-OH providing chemical shifts of +1.5, +2.5 and +4.0 eV respectively.[120,149] Thus these results support the conclusion that some combination of primarily hydroxides and epoxides are now present on the graphite sample. The appearance of a response in the O1s spectra in the UV/O_3 exposed sample also supports the conclusion that oxygen moieties are present. The literature reports that in the O1s spectra, C=O and O=C-OH groups give a peak at 530.6 eV, and the C-OH groups yield a peak at 533 eV.[120] The UV/O_3 exposed graphite with a peak located at 532 eV for the O1s, as observed in Figure 3.3, again supports the idea that some combination of different oxygen moieties reacted onto the graphitic surface.

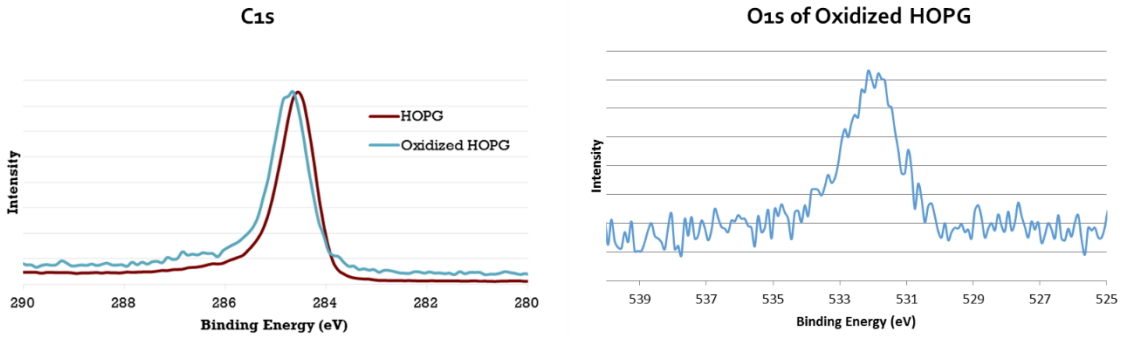

Figure 3.3 XPS C1s for HOPG and 30 minute UV/O_3 oxidized HOPG (left) and the O1s for the oxidized HOPG (right).

Graphene has a lattice spacing of 0.246 nm, and, with high resolution scanning the graphene lattice is visible due to stick-slip of the tip on the graphene sheet.[74] A high resolution image of graphite exposed to UV/O_3 for 60 minutes was obtained to see if there were any observed changes in the graphite lattice. Figure 3.4 presents the friction image from a small, high resolution scan along with the corresponding friction loop. There appears to be about a 0.25 nm spacing, which is consistent with the graphene lattice; the carbon lattice remains very periodic and with no observable change to the structure. The 60 minute UV/O_3 exposed graphite surface has a defect every 10.7 nm based on the I(D/G) ratio from the Raman spectrum results; therefore it is not surprising that even with the hour long time length of UV/O_3 exposure, there was no observed change to the lattice. One point defect would not have appeared in an image that is measuring the lattice so a few nanometers between defects would not have been enough to alter the lattice signal and thus the high resolution with the resolved lattice was achievable.

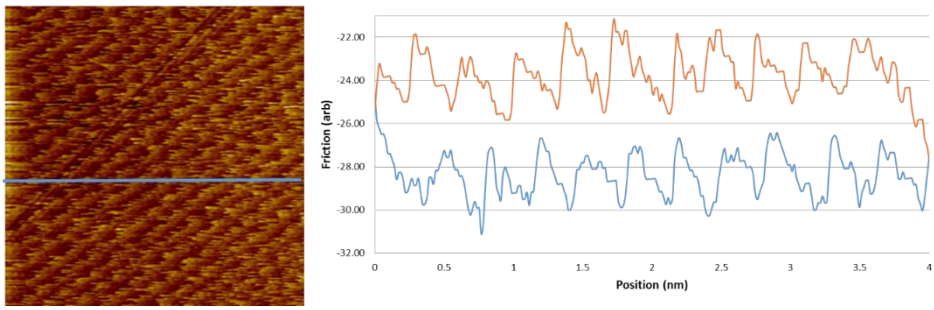

Figure 3.4 A 4x4 nm friction image and the friction loop (red line is the trace and blue is from the retrace) at the blue line in the friction image of a 60 min UV/O_3 HOPG sample.

While UV/O_3 gave another route for the broad oxidation of graphite, in order to study the direct impact of oxidation on the friction and topography, local patterning produced by biased AFM was employed. It was found that with the variation of several conditions, the extent of oxidation could be altered; specifically: moving slower, using a higher bias, or increasing the humidity led to an increased amount of oxidation. In Figure 3.5, the applied bias was changed while the other factors were kept the same. In this figure, it can be seen that by just increasing the bias, there was an increase in the amount of oxidation, with the higher degrees of oxidation distinguished by a higher friction change. The average difference in the friction of the oxidized and non-oxidized graphitic regions shows about a 7-fold increase in friction in the oxidized samples. These results agree with similar work done by Park and co-workers, who observed a 7-fold increase in the friction of a locally oxidized single layer graphene.[87] It is also observed in the topography that there is an increase in the height, with changes of up to almost 2 nm corresponding to the same region in which the friction response was higher. Other ways to increase the amount of oxidation achieved included increasing the time that the tip was in contact with a region, which is why decreasing the speed or increasing the dwell time also yielded higher amounts of oxidation. In general the increase of humidity also led to an increase in oxidation as this increased the size of the water meniscus at the tip and led to a larger area with the oxygen present for reacting being exposed to the bias.

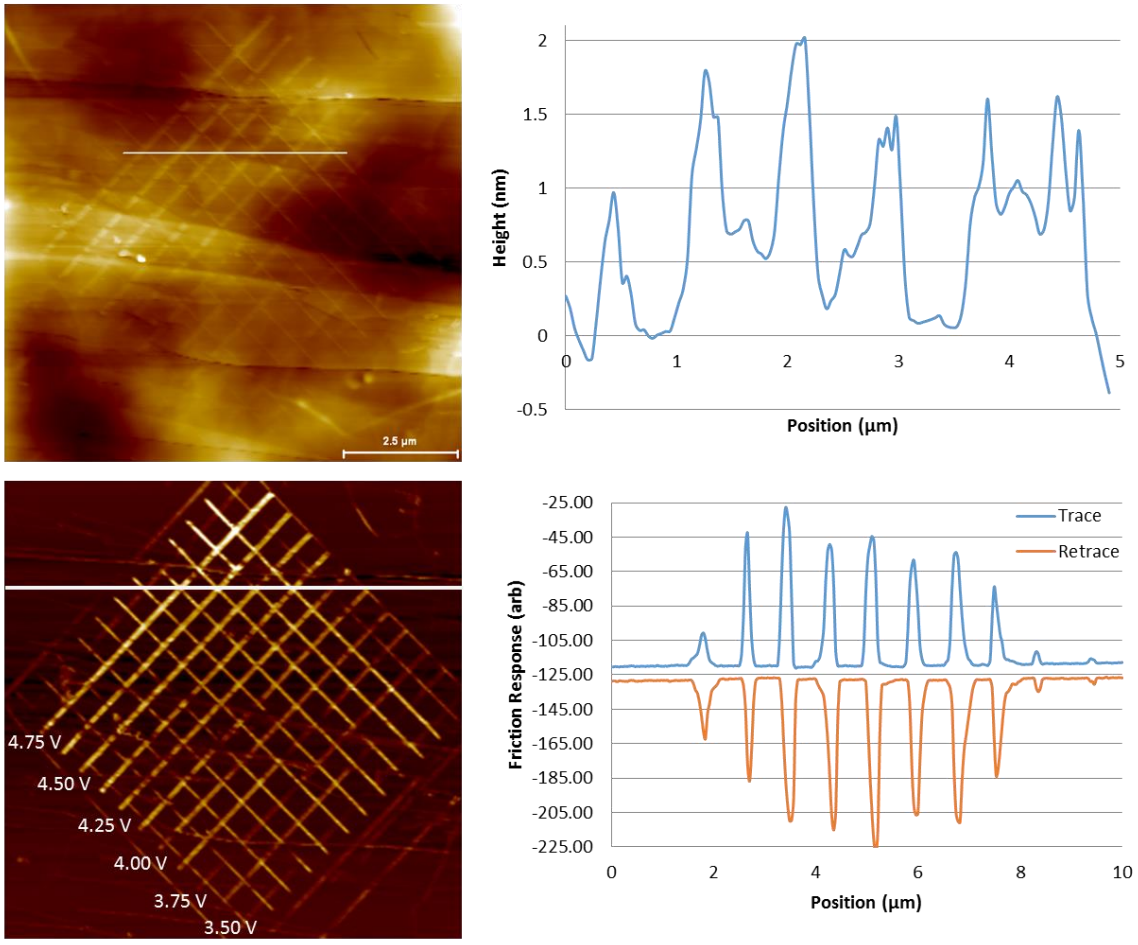

Figure 3.5 AFM topography (top left) with the cross section (top right) and friction (bottom left) with the friction loop (bottom right) images after lithography in which the humidity was 50%, the tip speed 0.1 µm/s and the bias varied from 4.75 to 3.50 V.

The observed trend of an increase in bias yielding an increase in friction was found to break down as the applied bias was increased to over 5 V. This is likely due to the fact that at the higher applied biases, there can be some burning away of the graphite instead of just the oxidation of the top layer. To support this theory, the topography signal shows a decrease in the height instead of the slight increase that was observed for

most of the oxidized samples as previously noted. This is not surprising as biased lithography has been used for small scale cutting of the surface.[115] Using Hummers' method or a modified Hummers' method, it was observed that fully oxidized debris was resettling on the surface of the graphene oxide flakes;[147] this technique however did not encounter that problem and thus allowed for the direct examination of the effect of oxidation on the friction of graphite.

Each of the parameters for the oxidation had its own optimization, but these parameters were not set quantities. For example, when a potential was applied between the metal coated tip and the conductive sample, an attractive electrostatic capacitance force was added to the adhesion force.[158] In an attempt to model this effect, several force-distance curves were taken while applying a range of biases. The measured adhesion from the force-distance curves was then plotted versus the applied potential. When the data selected ranged from 0 V to 2.0 V, the R^2 value of the linear trend line dropped to 0.9013, signifying a poor linear relationship. More importantly the amount of adhesion after 2.0 V applied bias was not within the range of the instrument as it was too high a value. The breakdown of the linear relationship is believed to be due to the fact that the graphite can begin to be oxidized close to the 2.0 V potential. The graph of the force of adhesion versus applied bias is shown in Figure 3.6 for the potential range of 0 V to 1.5 V and shows a much more linear relationship, as predicted by Tivanski and co-workers,[158] with the force of adhesion increasing as the applied potential was increased. Thus while the force of the tip was set to be constant throughout the biased lithography work, it must be understood that the force changed as a function of the bias,

though not in a predictable manner due to its complex relationship with the reaction at the surface.

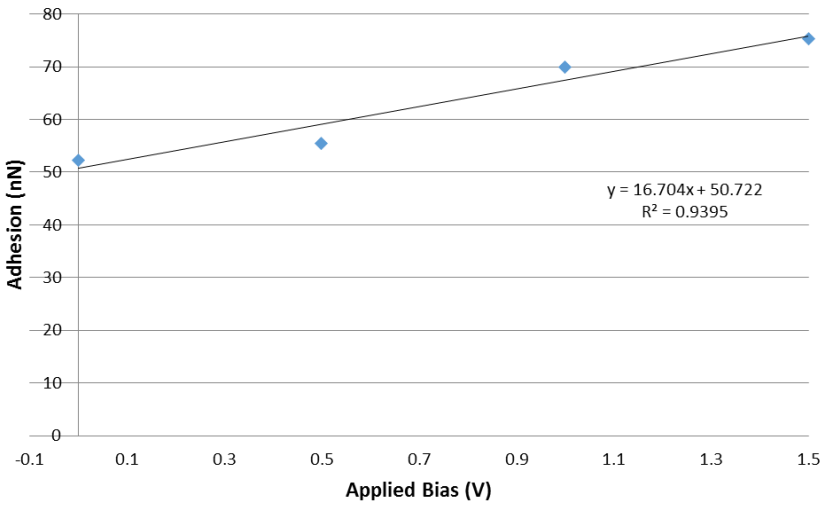

Figure 3.6 Force of adhesion as a function of applied bias based on force-distance curves taken with a metal coated tip.

When high resolution was attempted on the regions that had undergone biased AFM lithography, lattice resolved images were not obtainable. This is thought to be due to the fact that the lattice had been altered enough that the stick-slip motion of the tip on the lattice was not attainable. Also, it was also difficult to ensure that the tip landed on the oxidized regions without high levels of oxidation, so that high resolution of the lower oxidizing conditions could not be acquired unlike with the UV/O_3 oxidized graphite.

While the topography and friction identified that the surface had been modified, further characterization by Raman spectroscopy was desired. However, the typical local

biased lithography method conducted with the Agilent 5500 AFM had a small general area of oxidation, with each oxidized area less than 10 microns due to instrument design. Since the oxidized patterns were small in size, the background graphitic Raman signal overpowered any changes that could have been distinguished from the defects. To try and overcome the set-up limitations, the oxidation was attempted with the larger range WiTec Confocal AFM- the same instrument that took the Raman spectra. It was found that the Raman signal from the oxidized area was still too weak to see the D peak unless the graphite was cut by burning the area with a high bias. The topography, friction and corresponding Raman spectrum of the oxidized graphite conducted with the WiTec as shown in Figure 3.7. In this figure, a 6.0 V bias was used, and it was observed in the topography that the applied bias cut into the graphite. Based on the topography, the depth of the cuts ranged from 3 nm to over 80 nm. The friction response and loop also showed a change in the response where these cuts were, but also where there was no measured height change in the topography and no distinguishable D peak in the Raman spectrum. Thus it is theorized that there was oxidation, but not burning, of the surface in these lines, which did not have a high enough local oxidation density to show up in the Raman spectrum. The reason there was no increase in topography observed like in the work done on the Agilent is that while the WiTec provides an increase in scanning range, it does not give the same high level resolution in the z-range of the instrument. Even though the biased lithography conducted in Figure 3.7 was under the same bias, load, speed and humidity, there were significantly differing responses for the lines. This difference could be due to the changing amount of water in the water meniscus or the

surface roughness. XPS was not attempted, as one drawback with XPS is that it is only feasible when the area is large and homogenous. The local biased lithography patterns were so small that it was not possible to confidently focus solely on those spots, so XPS was only conducted on the UV/O_3 oxidized samples.

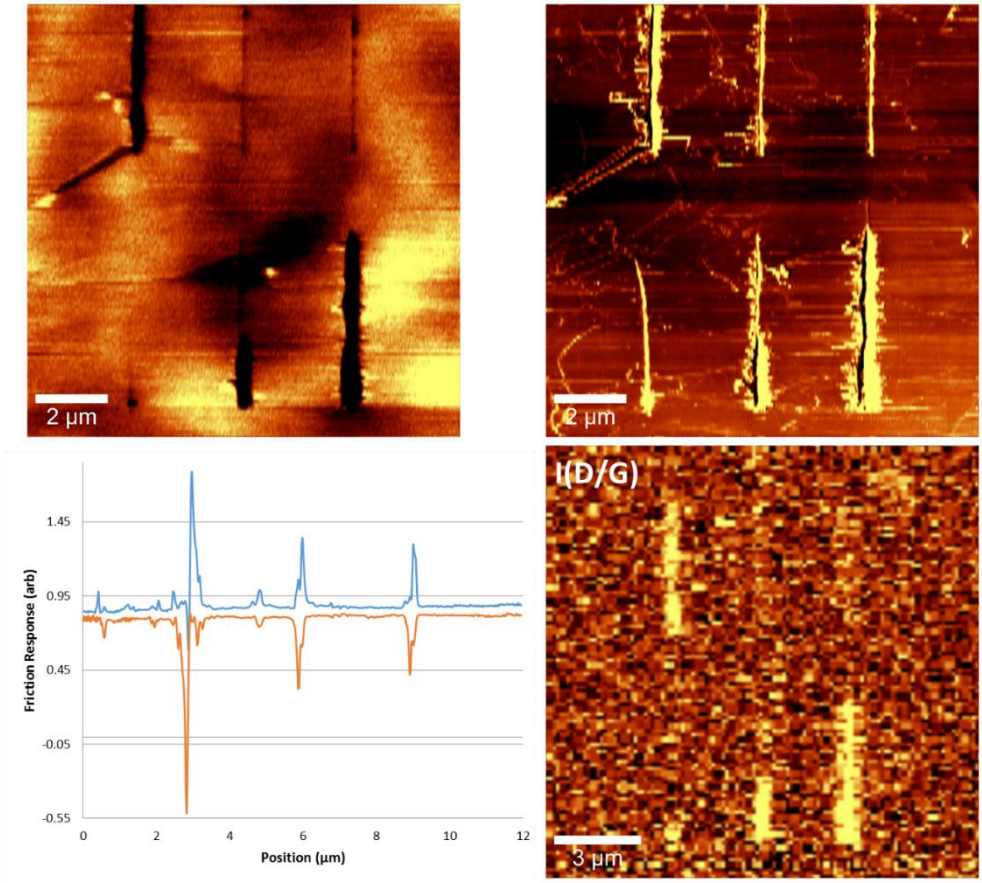

Figure 3.7 Oxidized graphite topography (top left), friction trace (top right), friction loop bisecting the middle of the top oxidized row (bottom left) and the I(D/G) scan from the Raman spectra of the same area (bottom right).

3.4 Conclusion

Graphite is a useful material, whether it is its conductive, non-reactive or lubricating properties being utilized. By functionalizing graphite, specifically by oxidization, it can be incorporated in more ways and studied as an easy platform for studying graphene. While Hummers' and modified Hummers' methods have been the primary source of oxidation, they leave an empty niche for a less aggressive and more controlled oxidation. In this work two techniques were used for oxidizing graphite samples: exposure to UV/O_3 and biased AFM lithography. The oxidation done broadly with UV/O_3 and locally by biased lithography only reacted with the first few layers of the graphite, with the oxide layers staying attached to the graphite substrate instead of naturally exfoliating as with Hummers' methods.

It was shown that UV/O_3 is a good method when large scale oxidation is desired. The limited depth of oxidation was confirmed after peeling the UV/O_3 oxidized graphite with Scotch tape, as the HOPG again showed pristine Raman spectra signals. Unlike with Hummers' method, it did not produce the oxidized debris as observed by AFM. The AFM high resolution scans were able to obtain the graphitic lattice even after 30 minutes of UV/O_3 exposure. This supports the use of graphite for its physical properties even if there is some small amount environmental UV or ozone exposure. There was also control over the extent of oxidation based on the exposure time. Based on Raman spectroscopy and Lucchese's equation, the distance between defects created by UV/O_3 was calculated, with a 30 minute exposure time leading to an average distance of 11.7 nm. These defects were confirmed to be from the oxidation of graphite by XPS.

For smaller-scale oxidation in a more complexly controlled environment, biased AFM lithography was conducted. This method allowed for the patterning of different conditions in one scheme which could be immediately studied by AFM. The AFM gave information on the physical changes, specifically topography and friction. Due to changes in the friction it was observed that the greater the bias applied, the more oxidation was able to occur, up to a certain limit. After about 5 V, the oxidation process morphed into a tool for cutting the surface, as confirmed by the decrease in the topography images. Comparing a well-oxidized region to the pristine graphite background showed about a 7-fold increase in friction. The friction response was found to have a higher sensitivity to the modification than the Raman spectra, which, in such a non-homogenous sample, was overwhelmed by the bulk graphite signal. While the amount of oxidation could be manipulated by several factors- the applied bias, humidity and applied force, among others- these factors were not static components. This work also reported the finding of how the force applied by the tip is increased with the application of a potential, but concluded that the exact amount of the increase becomes more difficult to predict as the potential approaches the level required to oxidize graphite. Due to the similarity in materials, the same complicated experimental design would be predicted to be present for graphene samples as well. This means of oxidizing also allows for complex patterned studies, such as with an STM which could investigate how self-assembled monolayers formed on graphite versus graphite oxide in a single platform.

With these two successful methods, more complex graphitic set ups can be created, combining the wonderful low friction properties of graphite with the functionality of the oxidized species. Future applications of these methods include creating Janus-like materials, with one side being oxidized and the other pristine. These complex materials could be applied in different settings such as a solid lubricant, or the functionalization of a surface with the oxidized species, but retaining its main graphitic features for decreasing the wear on the surface. Based on these results, if less oxidized and more controlled techniques are required for graphene oxide systems, these two methods would be much better than the graphene oxide produced by Hummers' method.

CHAPTER IV

WATER, GRAPHENE AND THE BUBBLES IN-BETWEEN

4.1 Overview

Graphene is an exciting material that has taken the research community by storm since its isolation in 2004.[7] The 3-dimensional form of graphene is graphite, which is composed of stacked graphene sheets held together by van der Waals forces, but graphene itself is the single sheet of carbon atoms in a honeycomb structure, with strong covalent bonds. The reason that this material is of such interest comes from its many desired properties including its electronic properties with high carrier mobility,[28] semimetal character,[26] ballistic transport[159] and massless Dirac fermions;[1] and also for its mechanical properties with its low coefficient of friction[68] and high Young's elastic modulus.[91] Since graphene is 2-dimensional, it has a large surface area-to-volume ratio, which makes it highly sensitive to any modification on the surface, whether covalent or not. These mechanical and chemical properties can be tuned for different uses in wide range of fields such as field effect transistors[160] to solid lubricants[161] to earphones.[162]

Graphene can be obtained in many ways such as: mechanical exfoliation, chemical exfoliation, epitaxial growth, and chemical vapor deposition (CVD), among others.[163] One of the easiest method to obtain graphene, which also yields high quality graphene, is the method Geim, Novoselov and coworkers used to first isolate graphene, mechanical exfoliation.[7] Graphene and few layer graphene are often transferred onto 90 nm SiO_2 as, due to the optimal refractive index changes, the single layer has enough of a

contrast to be optically observed[131] and the SiO_2 is an insulator which allows for the electrical separation of the system. However, in mechanical exfoliation it has been found that the use of tape actually can alter the graphene-substrate interaction, with the tape creating water-containing adlayers instead of pure water layers that might naturally occur on the surface.[21] It has also been found that the tape residues form an ultrathin layer on SiO_2 which, while not always observable by atomic force microscopy (AFM), was detected by electrostatic force microscopy (EFM).[22] It has been observed that general polymer residue adsorption can alter the doping in graphene with both reversible and irreversible effects,[164] therefore when using tape of any sort, there should be an impact on the graphitic material and its properties. Thus, tape selection is not trivial as it will dictate what residues influence the properties of graphene.

These graphene samples can be used for a wide variety of purposes, such as lubrication or electronics. Graphite has been used as a lubricant for many years, and for very small devices such as microelectromecanical systems (MEMS) and nanoelectromechanical systems (NEMS), there is much interest in using the thin graphene or few layer graphene as a thin solid lubricant.[20] These devices require lubricants to stop or delay the wear which leads to the ultimate failure of these devices due to the oscillating, sliding and rotating that occurs on the small scale that they undergo.[20] If graphene is going to be used as a lubricant, it is important to study how the graphene reacts to electric fields that might occur in the devices it is lubricating. Field effect transistors (FETs) also can use the 2-dimensional nature of graphene, to form small and thin electronic devices. For graphene to be an effective material for FET, the

lack of band gap must be overcome so that there can be an off state in the device. In order to create useable graphene FETs, the graphene can be manipulated to open up the band gap. This and other applications of graphene necessitate chemical modification or physical manipulation for the formation of a band gap and development of a selective surface. In order to create a complex structure control over the chemistry of the surface is required and one way to achieve this is by nanolithography such as with biased lithography atomic force microscopy (AFM). This technique combines the precise and local control of the AFM with the coordinated use of an applied bias to drive the oxidation reaction. This allows for the direct patterning of the oxidation on the micron and sub-micron scale, as conducted in this work. Thus the extent of chemical modification can be controlled by controlling the lithography situations.

This work also demonstrates the unforeseen use of biased lithography for a semi-selective means for the formation of graphitic bubbles. Since early in the days of researching graphene, there have been bubbles reported when graphene has been transferred onto substrates. Upon transfer gasses becoming trapped between the sheet and substrate, including in experiments where mechanically exfoliated graphene was placed on a SiO_2/Si support.[165] The size of these bubbles depends upon several factors including how many molecules are trapped between the surface and the graphene, the elastic properties of graphene and the amount of adhesion between the graphene and its substrate.[166] Bubbles can also be created by set ups that involve changing the pressure of the environment after placing the graphene[93] and by heating float transferred-graphene onto diamond.[101] The bubble formation has not been able to be controlled so

far, unless the design was such where the graphene was placed on hollowed out areas and the pressure changed. It was found in 2011 by Giem and co-workers that by changing the gate voltage the size of the bubbles could be altered, and with this report they theorized that graphene bubbles could be used as optical lenses.[92] These bubbles could also be used for high pressure, high temperature reactions as demonstrated with the graphene on diamond work. Bubbles introduce strain in the graphene which changes the electronic behavior[167] and increase the reactivity of the surface.[99] So far the graphene bubbles can be systematically created over porous regions, everywhere with the lattice mismatch with diamond or by chance with simple exfoliation placement, but for actual applications better control over the bubble formation is greatly desired. This work begins to address this lack of control over location issue.

To create the bubbles in this work, water either had to get between the layers of graphene or between the substrate and the graphitic material. However, there has not been much research into the interaction of a water layer between the graphene and substrate, partly due to the fact that methods such as chemical vapor deposition of graphene or mechanical transfers conducted in vacuum do not have a water layer on the surface. Graphene has been considered as an oxidation barrier for metals, but when there is water between the graphene and the substrate it has actually been shown to increase the oxidation compared to the bare substrate.[79] Theoretical work done has shown that the surface adhesion between graphene and SiO_2 is reduced when there is an adsorption of water on the substrate.[168] This water layer though can have an effect on the friction and topography, as Xu and co-workers showed with their growth of water

islands on the mica and subsequent studies with graphene on top.[80] It has also been shown with graphene and few layer graphene applied by mechanical exfoliation onto mica with a slit pore that humidity can be used to control the formation of water layers between the graphene and the substrate.[81] Even after graphene surfaces were formed on SiO_2, under very high humidity Lee and co-workers found that water was able to make wrinkles and droplets of water between the two has been observed.[169] However, not all of the graphene areas showed the same intake of water into the system and not the same results were obtained under the same conditions for graphene on mica.[169] Thus water is an important factor in graphene devices, but the extent of its effects have not been investigated.

Changing graphene's chemical or physical makeup can alter its mechanical response too. Graphene has incredible mechanical properties, with a low coefficient of friction,[68] a high elastic modulus of 2.4 ± 0.4 TPa for a single sheet[91] and a breaking strength of 42 N/m for a defect free sheet.[11] Cannara and co-workers proposed the reason for the low coefficient of friction response of graphite is due to the tip being able to lift graphitic layers.[75] When oxidizing graphite and graphene there is an expected change in the friction as the chemistry at the surface has been altered, which is indeed the case as Park and co-workers observed with a 7-fold increase in graphene's friction compared to that of the pristine.[87] Thus when oxidizing graphene or creating bubbles with graphene it is also imperative to study the mechanical response as the properties will change.

It is important to be able to characterize the surface when changing the chemistry of the surface and Raman spectroscopy allows for the monitoring of alterations in the graphitic material in a nondestructive technique. Graphene has a very distinct Raman signal, and as the number of layers grows, the ratio of the 2D to G peaks alters along with peak broadening. There is also a change in the Raman signal when the purity of the graphitic material decreases, with the breaking of the π system leading to the appearance of the D band around 1350 cm^{-1}.

For graphene devices to flourish, two issues need to be addressed, first, how does sample preparation effect the device and second, how can graphene's properties be manipulated. This work investigates both these issues. Specifically how different exfoliation methods can alter the graphene samples and their responses was investigated, as well as how biased induced oxidation may be used as a new method for graphene bubble formation and the novel properties therein. By learning more about these basic concerns, a better understanding for the future applications of graphene can be realized.

4.2 Experimental

In order to make the graphitic supported samples, first a 90 nm silicon oxide on a silicon surface was created. To begin, a rectangle approximately 1 cm × 2 cm was cut from a highly doped silicon wafer (Virginia Semiconductor) and cleaned. To clean the silicon the wafers were sonicated in a glass slide holder in isopropyl alcohol for 20 minutes, then rinsed with Millipore water (Barnstead). Next the wafers were placed in an acid piranha with a 3:1 of concentrated sulfuric acid to hydrogen peroxide in a water bath at 85°C for 20 minutes. The samples were then rinsed with copious amounts of

Millipore water, and placed in a base piranha 4:1 $NH_4OH:H_2O_2$ solution, also at 85°C, for 20 minutes after it started bubbling. After the base piranha the silicon was then rinsed with copious amounts of Millipore water and dried under N_2. Once the silicon wafers were cleaned they were then placed in a kiln and heated to 1050°C for 1 hour 23 minutes, creating an approximate 90 nm oxide film. The 90 nm oxide thickness was confirmed based on the Silicon Dioxide Color vs. Film Thickness and Viewing Angle Calculator found on Brigham Young University's Cleanroom website.[132]

There were several transfer methods used to transfer the highly oriented pyrolytic graphite (HOPG) to the SiO_2 surface, namely by Scotch tape (3M), thermal release tape (Graphene Supermarket) and water soluble wave solder tape (3M). The HOPG used was high quality graphite supplied by SPI or NT-MDT KTEK, with mosaic spreads ranging from 0.4 to 1.2 degree. All of the samples started off with the fresh peeling of the graphitic surface with Scotch tape, to cleave the top layers of the HOPG as contaminants will adsorb to graphite over time[133] and a pristine surface was desired. In the Scotch tape method the HOPG was peeled with tape, and then re-peeled several more times and finally placed on the surface of the SiO_2 and rubbed down. The tape was then quickly peeled off, to limit tape residues, leaving behind some of the graphitic material. In the case of the thermal release tape a section was placed on the HOPG, rubbed with a plastic surface so that when the tape was removed some of the graphite came along too. The thermal release tape was then placed on the SiO_2 surface, rubbed down, and placed on a heated hot plate at about 100°C till the tape turned white and lifted off the surface, within less than a minute, leaving a lot of the transferred graphite. This surface was then

quickly re-peeled with Scotch tape to increase the amount of single layer to few layer graphene. For the water soluble tape the tape was rubbed on the HOPG, peeled, and cut so that there was no excess tape on the sides and finally placed on the 90 nm SiO_2 surface. The sample was then placed in a hot water bath at about 85°C stirring for varying times from 5 to 20 minutes depending on when the tape appeared to have dissolved or removed. After that the sample was rinsed with high purity Millipore water and dried with N_2.

In order to identify the graphene, bilayer graphene, few layer graphene (FLG), graphitic and highly concentrated glue regions, the optical contrast was combined with Raman spectroscopy. Micrograph images were observed and taken using the WiTec confocal microscope with a 100x objective and optimized light for contrast. To confirm the micrograph's identification of the number of layers of graphene observed Raman spectroscopy was conducted. The single spectra of the different regions were obtained by doing 20 accumulations at 0.5 s integration time using the 488 nm Ar laser.

The samples were also altered using bias lithography AFM with the Agilent 5500. This instrument comes with a conductive set up, just requiring a conductive tip and manually connecting the sample to complete the circuit. A Pt/Ir coated tip was used with an initial average radius of 25.7 nm and spring constant average of 0.18 N/m. To accommodate for the fact that the 90 nm SiO_2 is an insulating material, part of the SiO_2 was scratched with a diamond cutter so that the silicon below was exposed and this is where the metal connecting to the bias was placed. The underlying Si is highly doped with a resistance of 1-3 Ω*cm. A schematic of the set-up is shown in Figure 4.1. The

same set-up was done on the WiTec atomic force microscope using an external power supply to complete the circuit for the bias lithography set-up. Lithography was conducted using the Agilent and WiTec while controlling: bias, tip speed, size of pattern, humidity and the force applied. The oxidized regions were immediately rescanned with the AFM in contact mode, using the same tip that conducted the lithography.

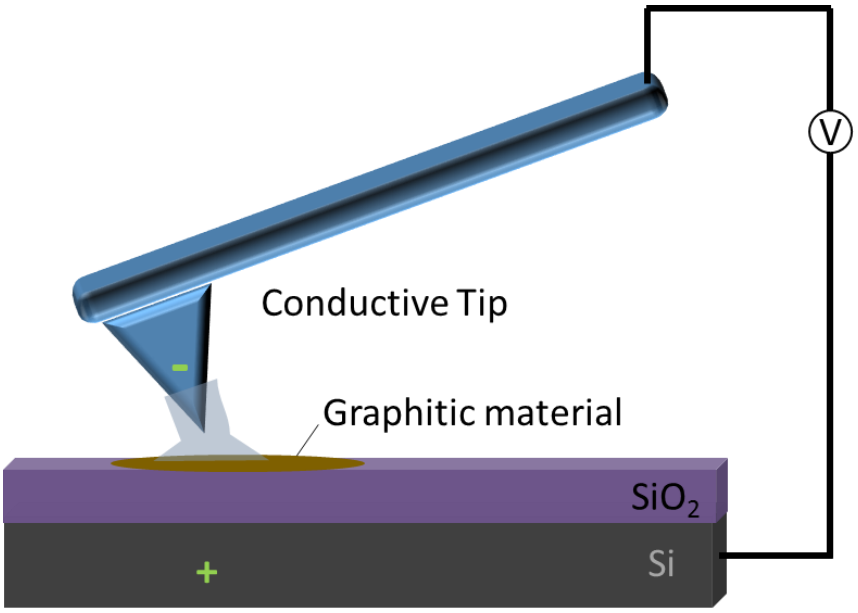

Figure 4.1 Schematic of the AFM biased lithography set-up.

From the AFM oxidation experiments with the water soluble tape some bubbles were created and the resulting bubbles were analyzed by Raman following the same methods as before the samples were oxidized. In order to compare the bubble region to its surroundings, three Raman mapping images were taken: one around the large bubble on the few layer graphene, another as a background image in a neighboring area where

no bubbles were observed and the third was taken in another section where small bubbles were observed. The bubbles chosen to compare were selected on few layer region instead of on the more graphite-like regions.

While contact mode gave friction and topography images, it was not ideal for obtaining the height of the bubbles as it was pushing them away or flattening them, therefore tapping mode with the Agilent AFM was used to study the surfaces of the water soluble tape samples. This meant that the bubbles were studied by intermittent contact, helping to decrease the amount of shear the tip was applying on the raised graphene areas. Tapping mode AFM was conducted with a Vista Probe silicon tip where the tip was oscillated close to its resonance frequency, around 190 kHz. Regions where bubbles were observed by optical micrographs were analyzed along with regions where no bubbles had been viewed optically on both oxidized and non-oxidized areas of the graphite.

A Pt/Ir tip was used to conduct force-distance curves on the supported graphitic surface. For the water soluble tape samples the curves were taken on all of the different surfaces: the SiO_2 substrate, the regions where there were no bubbles and no bias applied, the region with bubbles large enough to be seen optically and easily landed upon, and on the region with small bubbles visible only by tapping mode.

To test how the bubbles reacted to heating, a sample showing bubbles after oxidation was placed on a Lake Shore 321 Autotuning Temperature Controller heating stage (Westerville, Ohio) and monitored optically as the stage temperature was increased. The temperature of the stage was raised a total of 60°C, increasing 10 degrees

every 20 minutes, till it reached the highest temperature set and was held there for 10 minutes, then the temperature was cooled, decreasing 10 degrees over every 20 minutes. Optical micrographs were taken during the process every 20 minutes and then a number of others over the next several days. The black and white images were analyzed using Image J software to measure the gray value of the cross section on one bubble over the time.

4.3 Results

To test how sample preparation methods altered the supported graphitic design, several graphitic structures on SiO_2 were created. While mechanical exfoliation was used for each sample, three different transfer methods were used: Scotch tape, thermal release tape and water soluble tape. For all three types of fabricated samples, the number of layers of graphitic materials were initially identified by optical contrast due to the 90 nm thick silicon oxide substrate. One optical micrograph is shown in Figure 4.2 with the substrate and different number of layers labeled. Single layer graphene is just distinctly visible and appears faint and pale gray compared to bilayer which is darker, few layer which is even darker and finally graphitic regions which appear white. In order to confirm the identity of the graphitic species Raman spectroscopy was also conducted on areas of interest on each of the samples. For the graphene regions the large 2D-to-G peak ratio gave confirmation of the identity. For the bilayer to few layer graphene there is an almost equal peak intensities between the 2D and G peaks and some 2D peak broadening was observed. With the very distinguishable graphitic regions there is a large G-to-2D peak ratio with even more peak broadening, all of which is shown in

the Raman spectra in Figure 4.3. One important peak which was not observed in the initial samples was the D peak, or defect peak, that can be located at about 1350 cm^{-1}. This speaks to the high quality of the transferred graphitic material, which had low defect densities.

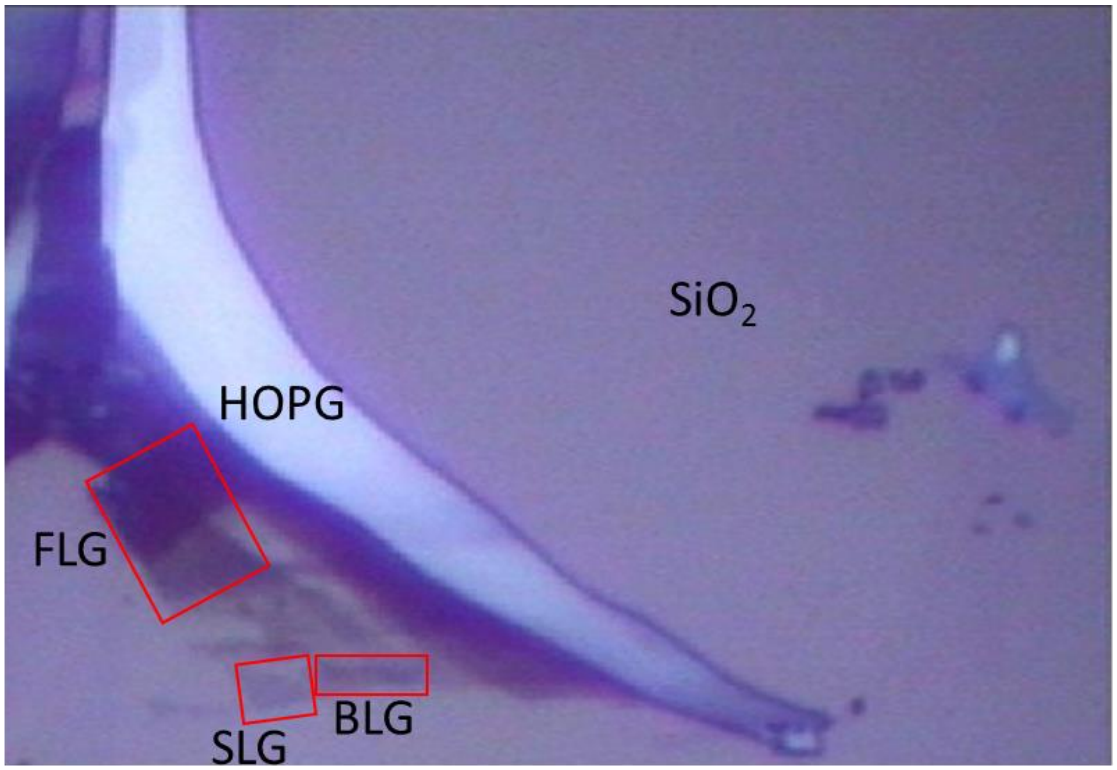

Figure 4.2 Optical micrograph of a sample surface with single layer graphene (SLG), bilayer graphene (BLG), few layer graphene (FLG) and graphite (HOPG) labeled on the 90 nm SiO_2 substrate.

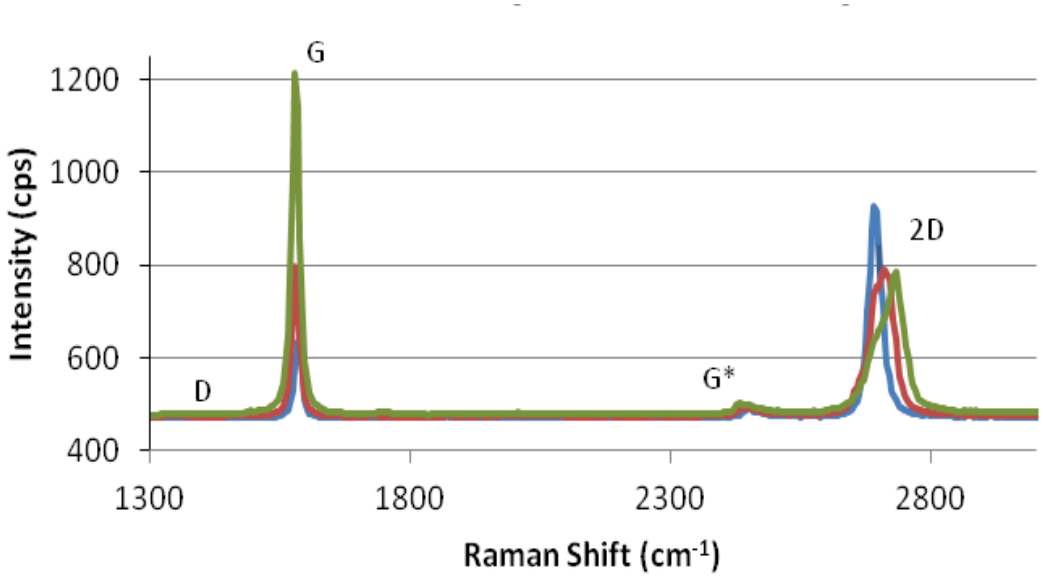

Figure 4.3 The Raman spectra for graphene (blue), few layer graphene (red) and HOPG (green).

Aside from the occasionally visible tape residues, the three techniques produced similar graphitic samples confirmed optically and by Raman spectroscopy. To test these different designs, biased lithography was employed on all three samples. Unlike in Chapter III, where the substrate was conductive, as the material studied was graphite, in this scheme there was an insulating 90 nm layer of SiO_2 between the conductive graphene, or graphitic material, and the highly doped silicon. Thus the reactions attempted on the supported graphene require higher potentials, ranging from 6-10 V instead of the 2-5 V for the graphite. This is because it is the electric field that drives the reaction with the supported graphitic material and it must overcome the oxide barrier. To determine the electric field strength experienced at the tip a simplified model where

the tip is considered a conductive sphere was used with the following equation from Wang and Woo:

$$\Phi = \frac{-Q}{4\pi\varepsilon_0 a} \quad (4)$$

where Q is the single charge trapped in the sphere, ε_0 is the dielectric constant of the vacuum and α is the tip radius.[170] When the potential applied was 7 V this meant that there was an electric field of about $2.35*10^6$ C/m. This is an approximation based on the tip size, but even the radius of the tip changed over the experiment, with new conductive tips having an average radius of 25.7 nm while the tips used for lithography and scanning showed an average tip radius of 35.8 nm.

One difference in the graphene/SiO_2 samples created by Scotch tape was that it was found to make smaller graphene and few layer graphene general areas than those in which water soluble tape and thermal release tape were used. The more distinct difference though was that when oxidation was attempted on the Scotch tape based samples, some sort of growth was observed outside of the graphene region. This development appearing to branch out from the graphitic region which had experienced the bias, with the progression depicted in Figure 4.4. Areas that had not undergone the biased lithography did not see this same growth even with multiple scanning of the surface, as are pointed out with the red arrows in the leftmost bottom two images in Figure 4.4. The biased lithography was conducted in the middle of the graphene region, and the subsequent growths were evident in both the topography and friction images and are pointed out with black arrows in Figure 4.4. The height of the new expansion ranged from 2 to 5 nm high and had a change in friction that was closer to that of the lower

fractioned graphene than the higher friction area of the SiO_2 substrate. Since the oxidation conditions occurred under high humidity, on an area that had been exposed to Scotch tape it is theorized that the growths are the reaction of some of the tape residue to the bias and humidity. It is also believed that since the graphene layers themselves are conductive, they were able to spread out the electric field which is why the growths

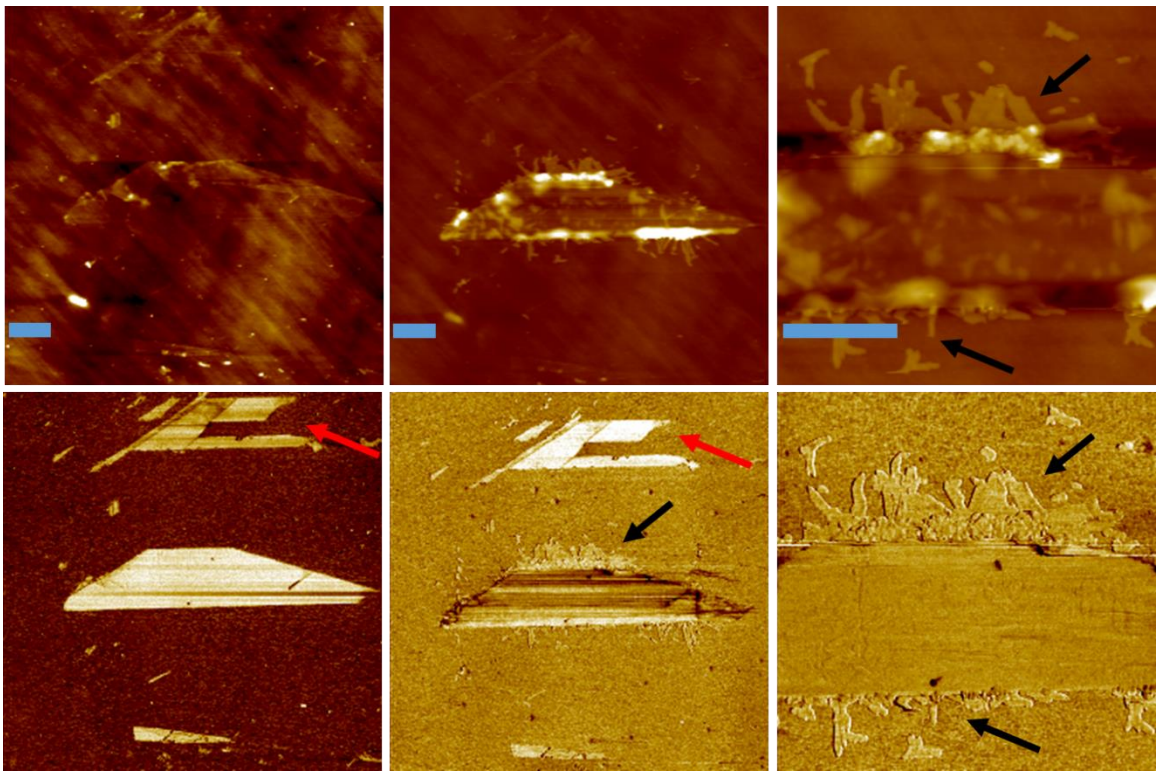

Figure 4.4 Scotch tape made samples with topography (top) and friction (bottom) before oxidation (left), after oxidation (middle) and zoomed in (right). All scale bars represent 1 micron.

appear around all the edges of the graphene region. The growths were also analyzed with Raman spectroscopy, but no signal outside of the SiO_2 was observed, but the glue from the tape when visible from the objectives and scanned by Raman spectroscopy was also invisible to Raman spectroscopy.

The second method for sample creation used thermal release tape which required the exposure to a hot surface to remove the tape. Again, biased lithography was attempted on the graphitic regions of the samples. This time, after the lithography attempts on a multilayer graphene region wrinkles appeared in the local area where the bias was applied. These wrinkles though appeared to dissipate or become "ironed out" after several subsequent scans. As the wrinkles only occurred after a potential had been applied, the cause of the wrinkles might be due to a very small amount of water intercalation due to the natural humidity. This water would then be pulled towards the electric field at the tip, and was subsequently flattened after rescanning. Water intercalation has been observed under high humidity conditions,[80] so it is not unreasonable to expect some intercalation is possible as the humidity was set to over 70% for these experiments. Besides the wrinkling noted on the graphite, there was also the generation of donut looking growths on the edges of the graphitic material. In Figure 4.5 the progression from before lithography to after showing some of the wrinkles present to a zoom in on the donut area is shown. The wrinkles were most evident in the friction images and are marked with a black arrow on the larger scan as shown Figure 4.5, but were also seen in the topography in the smaller images where more fine definition could be observed. It is believed that the bias spread throughout the graphitic

material due to the high conductivity of the graphene sheets and that a reaction occurred at the edges. This is supported by the fact that regions of the contiguous graphite saw the donuts even when the bias was applied several microns away, as seen in the right images marked with the red arrows in Figure 4.5, whereas a noncontiguous graphene layer that did not have bias applied on it in the same region saw no donuts form around it. When scanned by Raman spectroscopy there was no signal outside of the silicon dioxide observed. However, the donuts were very small so it is possible that if there was a signal it would have been too weak or they could have been Raman inactive. Thermal release tape also lacked a Raman signal when scanned on its own. The donuts themselves are observable in friction, with a similar response as the silicon dioxide, and the topography appeared to exhibit a slight depression. The hypothesis is that the donuts are actually further oxidation of the silicon dioxide, induced by the high potentials and high humidity, thus the friction would be similar to that of the grown SiO_2 substrate.

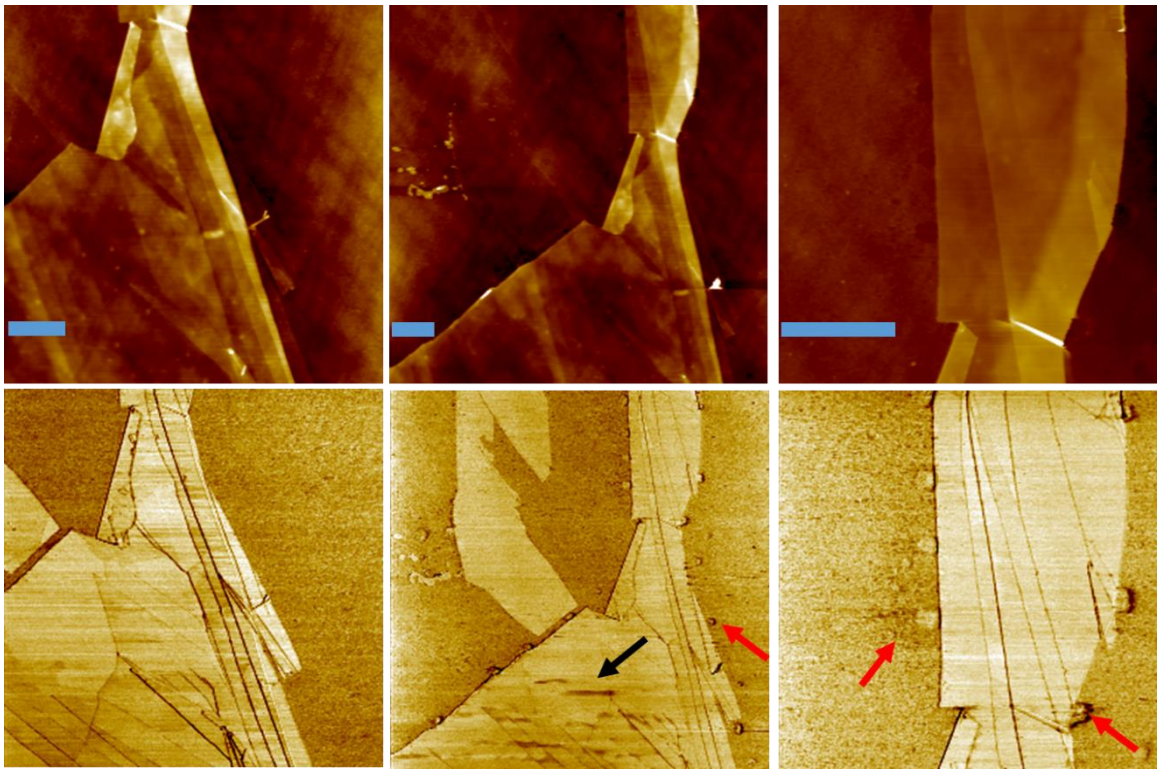

Figure 4.5 Thermal release tape method sample with topography (top) and friction (bottom) before oxidation (left), after oxidation (middle) and zoomed in after (right). All scale bars represent 1 micron.

After comparing the AFM results from the donuts from the thermal release tape samples and the expansions from the Scotch tape prepared samples, the two growths do not appear to be the same material. Their friction and topographical responses are very different even though the oxidation conditions were very similar. This supports the theory that it is tape identity dependent response and that at least one of them is due to the specific glue residues from their respective tapes.

While the Scotch tape and thermal release samples were made with differing tapes and different conditions, no heating versus heating, the third sample preparation

method by water soluble tape involved the submersion in warm water. This method provided larger few layer graphitic regions than the other two methods. Unlike the other two techniques, the water soluble tape samples exhibited oxidation of the graphitic material under biased lithography. While the oxidation sometimes occurred, a more frequent, and sometimes concurrent, result was the formation of new features that were later determined to be bubbles. A small scan AFM image showing both the oxidized multilayer graphitic pattern and a bubble created by biased lithography are shown in Figure 4.6. While both features are observable in the friction image, it is not so in the topographic image. The topography only shows a possible slight increase in height for the oxidized region, not the bubble, and in fact the contrast in the topography could be due to coupling in the x-y of the tip to the frictional change as opposed to true height information. Aside from the type of tape, these samples differ from those made with Scotch tape or Thermal release tape, as they were heated in water for several minutes. In Figure 4.7 a possible scheme of the theory on how the graphitic material is being translated into bubbles is shown. In this process bilayer graphene on Si/SiO_2 substrate is depicted, the intercalation of water in between the layers and between the substrate and graphene from the submersion in the hot water, to finally the electrolysis of some of the water molecules to form hydrogen and oxygen gas. While the scheme shows a bilayer graphene situation, the bubbles were observed on several types of graphitic situations, from bilayer to graphite-like number of layers. It is also not known if the water that is hypothesized to be intercalating into the system is only between the graphene layers but it could be that the water is only between some layers or only between the bottom

graphene sheet and the substrate. Also unclear is exactly how many layers are forming the bubbled region. The support for the gas formation as the major source of pressure for the bubble formation is discussed later in this section with the heating data.

From the literature, the minimum voltage needed, under ideal conditions, for the electrolysis of water is 1.23 V.[171] However, in this experiment there is a very complicated electric field, in which a direct voltage of the current at the junction of interest cannot be measured. As previously mentioned, the approximate electric field calculated for a 7 V applied potential was $2.35*10^6$ C/m, however, this calculation assumes that the tip radius is where the charge is staying, but when the tip comes into contact with the conductive graphene, the charge should spread across the entire sheet. To support that the field is throughout the graphitic material, while biased lithography was conducted on parts of a graphitic region, the bubbles could appear on any contiguous region. Thus the true electric field depends on the size of the graphene samples that the tip is in contact with. Experimentally the bubbles were observed on many different size samples of graphitic material, but all much larger than the tip, as they were at least several microns in size, so the electric field can be expected to be much lower than the calculation.

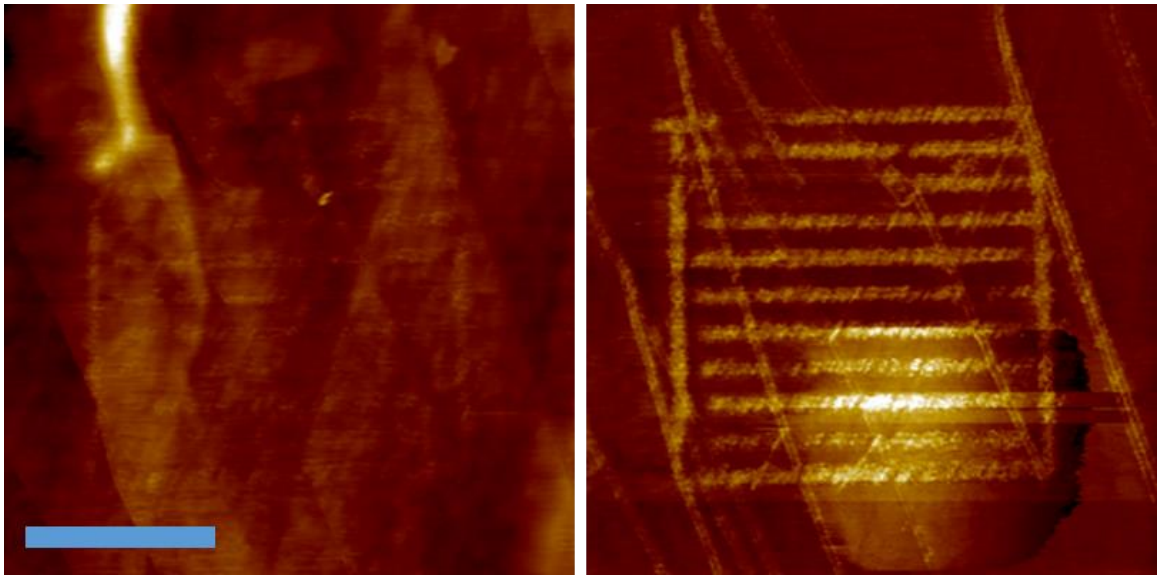

Figure 4.6 AFM images, topography (left) and friction (right), of a bubble and the biased patterning on the WST sample. The scale bar is 0.5 microns.

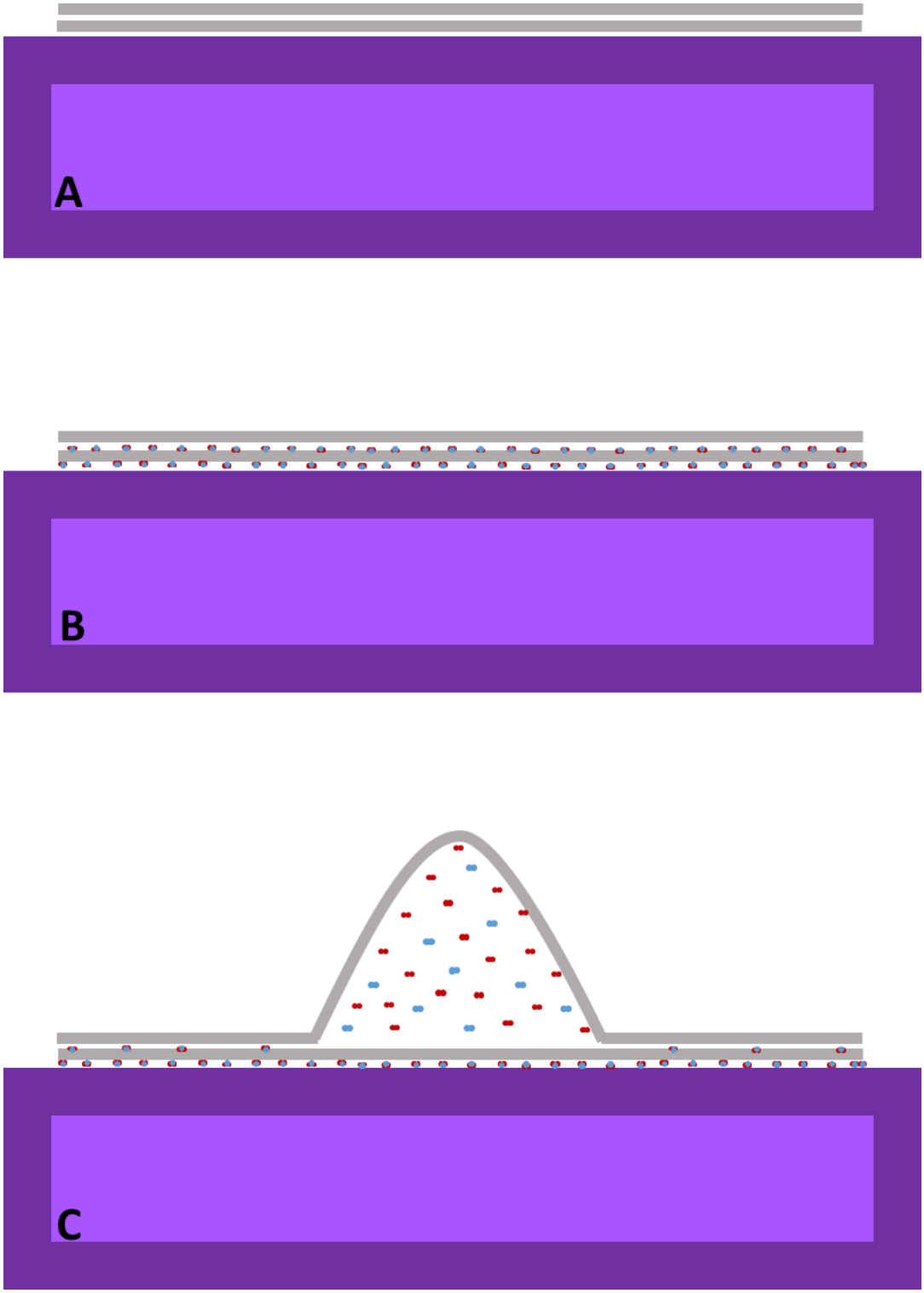

Figure 4.7 Schematic of bilayer graphene on Si/SiO_2 (A), after being treated in hot water (B) and after biased lithography (C).

The largest bubble measured was 200 nm in height with a radius of 1.25 μm, giving it a volume of about $4.96*10^{-19}$ m^3, when using the formula for volume for a spherical cap. When assuming an ideal gas, an internal pressure of 1 atm and a temperature of 298 K, leads to there being $2.03*10^{-17}$ moles of gas, or $1.22*10^7$ molecules of gas following the ideal gas law. If all these gas molecules were to have come from water molecules, there would need to be $8.15*10^6$ water molecules. If the assumption is made that there was a monolayer of water on the same area, using the radius 1.25 μm for the radius of a circle, and 0.1 nm^2 area for each water molecule, then $4.92*10^7$ water molecules would be present. This value is in the same range as the number of water molecules needed to form the bubble. There are several reasons though that this model is only an approximation, as there are many assumptions made which could greatly change the values obtained. Some of the assumptions for calculating the number of gas molecules present include: ideal gas scenario with non-ideal gasses; that the pressure is at 1 atm; and that all of the gas comes from the decomposition of water alone. There are also assumptions on the number of water molecules present, including the major assumption of a monolayer of water, that the bubble was not multiple bubbles combining, which would have had a larger surface area in which to create the gas, and ignores the attraction of water molecules to the tip when the bias was applied. Still, these calculations show that an, as an approximation, it is reasonable to assume that the bubbles could be generated via the electrolysis of water.

While the bubbles were observable in the friction, they were not unsusceptible to the scanning conditions. As seen in Figure 4.8, three chronological scans showed no

indication of the bubbles in the topography images while there was movement of the bubbles in the frictional images. The bubbles were observed to move down in the same path as the slow scan direction. Some of the bubbles were also observed to join multiple bubbles into one, showing a fluidity in their nature. It is believed that the force of the tip was able to slowly push the air inside the graphitic pockets down the substrate, meaning that the bubbles do not have firm boundaries but are able to move with the movement of the graphitic layer(s). The lack of pinning of the bubbles also meant that sometimes the bubbles were observed to shrink, and it is believed that the gas was able to escape to other regions in the graphitic material. When the bubbles were close to edges of the graphitic material scanning that drove them toward the edges led to the decrease in the number of bubbles present. There were also either small bubbles, gas or water that was observed to move in the friction images, some of these smaller bands are seen in Figure 4.8, though sometimes these bands were less defined than shown in these images. Aside from moving these bubbles due to scanning conditions, there was also the lack of signal change in the topography, which meant that contact mode was not able to obtain height information.

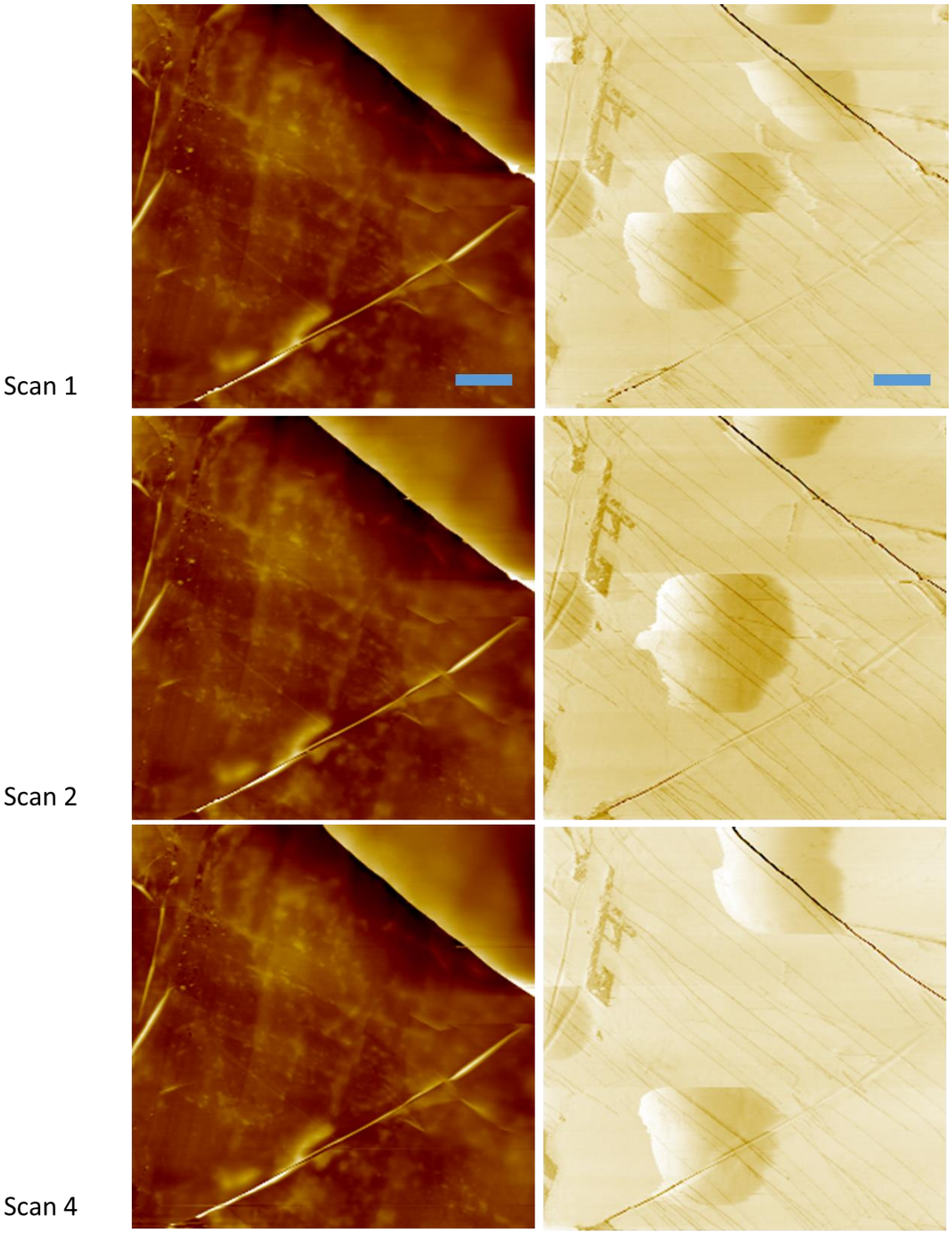

Figure 4.8 AFM, topography (left) and friction (right), response of bubbles in first, second and fourth subsequent scans. Scale bar is 1 micron.

To acquire a better picture of these bubbles and measure their true height, tapping mode AFM was used. It was observed that the bubbles that had been observed in the micrographs and contact mode ranged greatly in size. It was also observed that bubbles that had not been previously known to exist, either based on contact mode scanning or by optical contrast, were in fact present. This might help to account for the odd friction responses that were sometimes observed in some of the contact mode scans, where it had been assumed that it was water moving through the layers, but could in fact have been gas. These not optically observed bubbles were small in size, ranging from about 6.5 nm to 10 nm. The size of the bigger bubbles that were visible in either optical or contact mode had a large range in size, starting just above 10 nm to 200 nm. It is the results from these tapping mode images that confirms the height that was assumed from the optical changes under the microscope and from the friction images taken by contact mode.

The water soluble tape samples were re-investigated using Raman spectroscopy after biased lithography to monitor changes induced by these bubbles. By focusing on the regions where bubbles were visible to the 100x objective and comparing the Raman maps to the optical micrographs, the Raman signal for the different sized bubbles were examined. It was observed that the larger bubble did show distinct differences from the background and area of small bubbles, single spectra taken from the three regions are shown in Figure 4.9. The ratio of the 2D/G peaks on the larger bubbler are more similar to that found in bilayer graphene, even though prior to the bubble formation the region was of the same color and therefore should have the same number of layers as the

sample Raman taken for the background. This supports the assumption that the bubbles are either a single layer or only just a few layers of graphene that are being raised, thus giving a more bilayer-like signal. The 2D peak was shown to shift slightly, to lower wavenumbers for the larger bubbles, congruent with the more bi-layer signal values. Another noticeable change is that the location of the G peak is also shifted to lower wavenumbers for the larger bubble. This shift suggests that there is indeed strain, as reported in the literature,[172] since this changes the distance between the bonds. The Raman mapping with and without bubbles shown here was conducted on the few layer graphene region as the graphite-like region results had too much background signal to distinguish differences in the bubble regions.

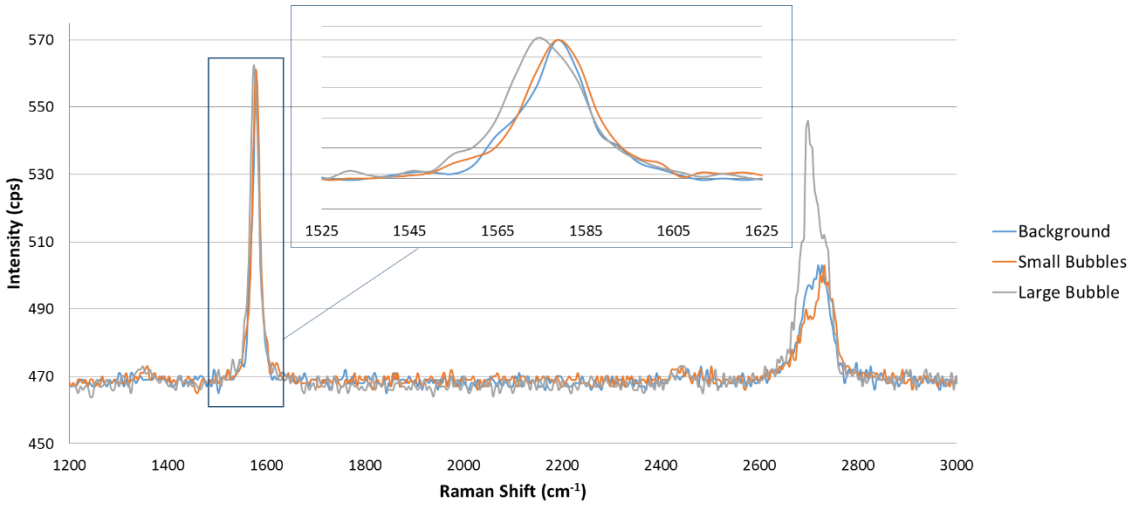

Figure 4.9 Raman spectrum focusing on graphitic areas that had no bubbles (blue), small bubbles (red) and a large bubble (gray). Inset is a zoom in on the G band.

Force-distance curves give information on surface interactions. When force-distance curves were taken on the graphitic regions before any oxidation attempts, the expected, sharp retract peak was observed. This sharp retract was evidence of the quick pull off of the tip from the graphitic surface as the interacting forces were overcome. However, when conducted directly on bubbles or regions that had bubbles, the retract curves were prolonged. These pull-off curves looked more like there were several un-binding events as observed in some cell adhesion studies[173] or like there was a capillary bridge that raised as the tip went up till it finally snapped off.[174] Examples of the force-distance retract curves observed on the SiO_2 substrate, few layer graphene region where there were no bubbles and on bubbles themselves are shown in Figure 4.10. The approach curves, though not shown, on the bubble containing region has a much larger snap in force, about 18 nN, compared to the less than 1 nN experienced by both the SiO_2 and bubble-free few layer graphene. This difference could be explained due to the more malleable state of the graphene bubble, as the tip starts to put pressure on the air or liquid inside, moving them out of the way and allowing for a larger amount of contact area. The graphene bubbles also do not have direct contact with their substrate, allowing for more freedom of movement. Both the SiO_2 and bubble-free few layer graphene material have very similar force-distance curves, as seen in Figure 4.10 with the graphitic region showing slightly higher adhesion. It is the graphene bubble region that has the prolonged and high snap off data. The theory behind this is that the bubble allows for the tip to become surrounded by the graphene before it hits the more firm substrate. This would explain the larger snap-in force for the bubbled region as the

trapped air would be able to morph around the tip. Then, as the tip was pulled away from the sample, the graphene-tip interactions are much greater as the graphene can surround larger areas of the tip. As the tip moves away from the surface, the bubble can only extend so far, if at all, before the graphene begins to unbind. Thus the force-distance curves will have a longer and distance of unbinding events which leads to what was referred to as a prolonged retraction.

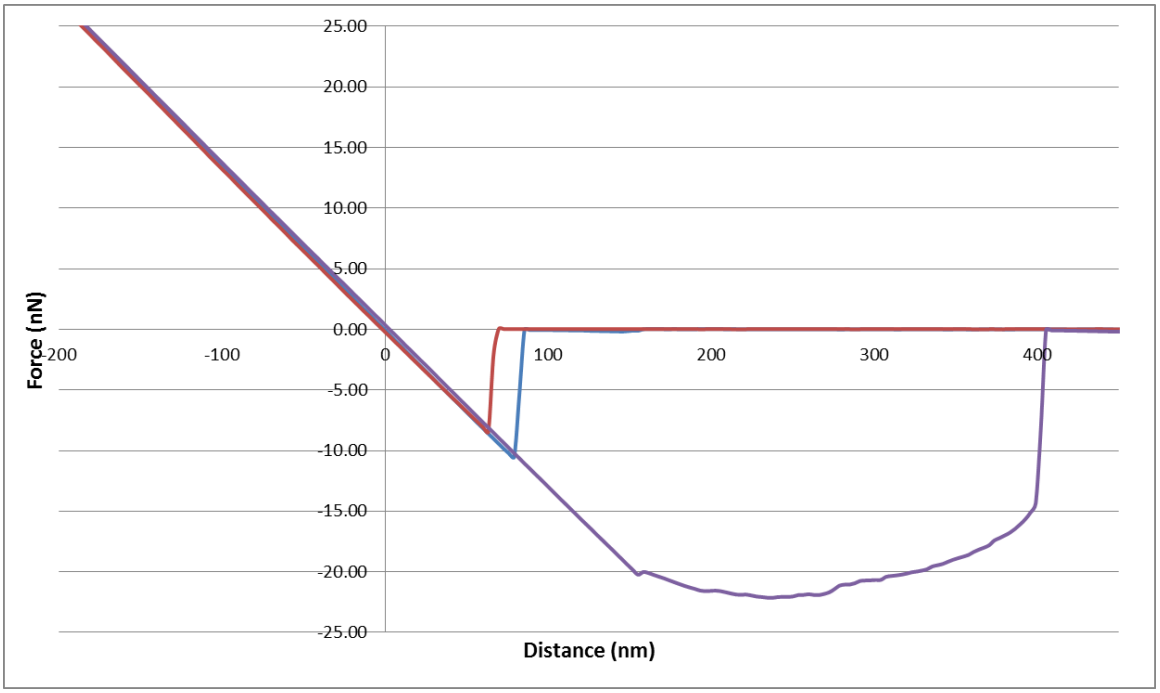

Figure 4.10 Force-distance curves for SiO_2 substrate (red), few layer graphene supported on SiO_2 (blue) and on a graphitic bubble (purple).

For further confirmation of the identity of the bubbles and to better understand their properties, the bubble samples were optically monitored while being heated.

Bubbles would be expected to show an increase in size with an increase in temperature, following the relationship of pressure and temperature of gasses. The images of the before heating, at the hottest temperature heated to and a few days later of the bubble area shows that there was a large effect from the temperature change. As the stage was heated the bubbles appear to grow or spread and then upon cooling the bubbles appear to start going back to how they were in the beginning. Snap shots from the process are shown in Figure 4.11 with a before, during and after cooling images. One bubble in particular, marked with a yellow line bisecting it, was tracked over time. Specifically after each step in the heating process, the change in the observed gray value was noted. This cross section of the gray value and its change with respect to heating is thought to be correlated to the height. The way that the color changed for the bubbles differed depending on the thickness of the graphitic material where they were located. Initially, the bilayer and few layer graphene section the bubble appears lighter in color whereas in the multilayer region the bubbles appear darker in color to their graphitic flat region counterparts. For the bilayer and few layer graphene, this is thought to be due to in part to the physical height off the substrate, as higher protrusions are going to appear lighter in coloring from the focusing of the camera. The bubbles located on the multilayer graphene section though appeared darker, partly because the multilayer graphitic region is more like graphite and thus is not as transparent as the graphene to few layer graphene. The bubbles on top of multilayer graphene are likely only one to a few layers thick of graphene, which is more transparent, so this would change the way the light

traveled, as it would be able to go through the single to few layer but would be reflected off the graphite regions, losing some of its intensity as it changed refractive index.

The cross section of the gray value for the bubble on the few layer graphene as it was heated and then cooled is show in Figure 4.12. It was observed that with the heating the gray value increased and then with the cooling, the gray valued decreased. The shapes of the cross section also changed over the heating and cooling process. Initially the bubble began with a slight dark center, implying a donut-like shape, with the donut-shape becoming more distinct up to the raised 50°C change. After that, the shape became more parabolic, implying that whatever layers were resisting forming the bubble by van der Waals forces, were overcome by the building pressure from the air in the bubble. This also led to a change in widths, with the hottest time leading to the tallest bubble, but also the narrowest. However, upon the last cooling cycle, the cross section appeared to have expanded back to the same size of the initial size before heating. There is some error in this measurement due to having to manually take the cross section after placing the sample in as identical a manner as possible, but no large variation in the x-y plane was noted and the images matched fairly well. This corroborates the hypothesis that the bubble is rising due to increased pressure in the z direction as seen in the gray value changes, but as the gas is in the bubble, the general van der Waals interactions of the graphene-graphene and graphene-substrate remain the same. Based on the micrographs and gray value cross section, it supports the theory that there is a gas inside the bubble that is expanding, following the ideal gas law, as the temperature increases

due to the increased pressure. As the changes are noted well below the temperature of water's boiling point, this discounts the theory that this could be just water vaporizing.

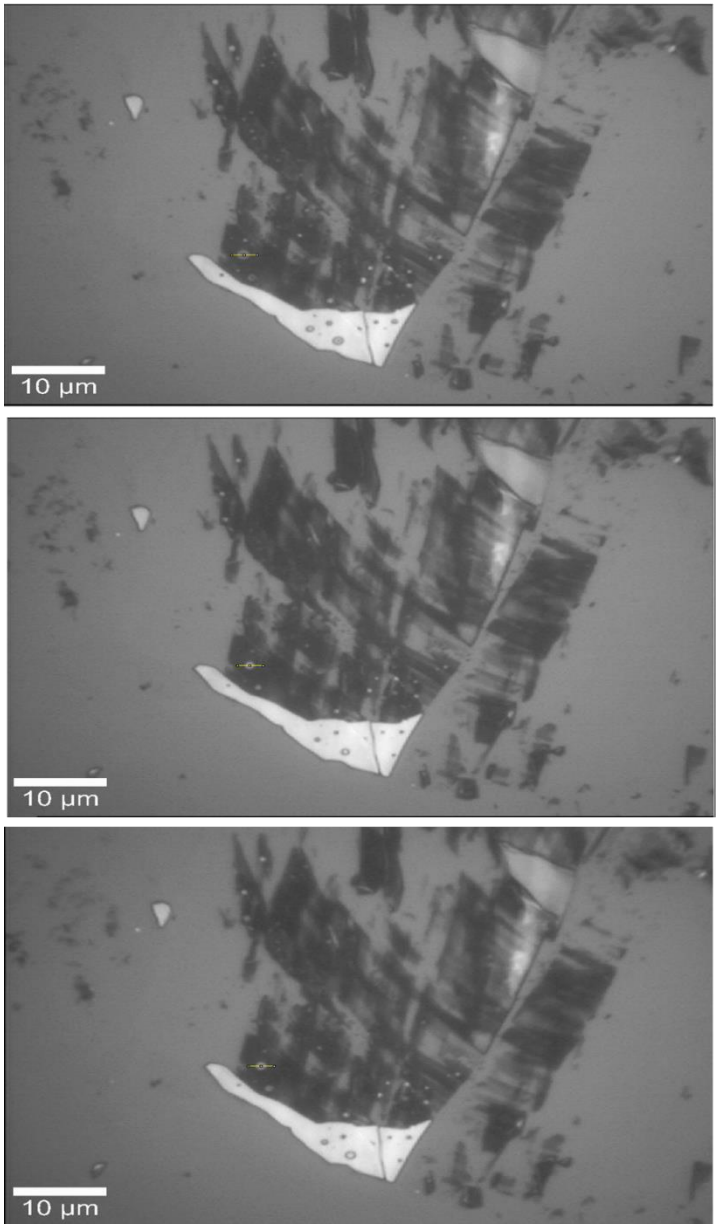

Figure 4.11 The bubble surface before began heating (top), at 60°C above room temperature (middle) and several days later (bottom).

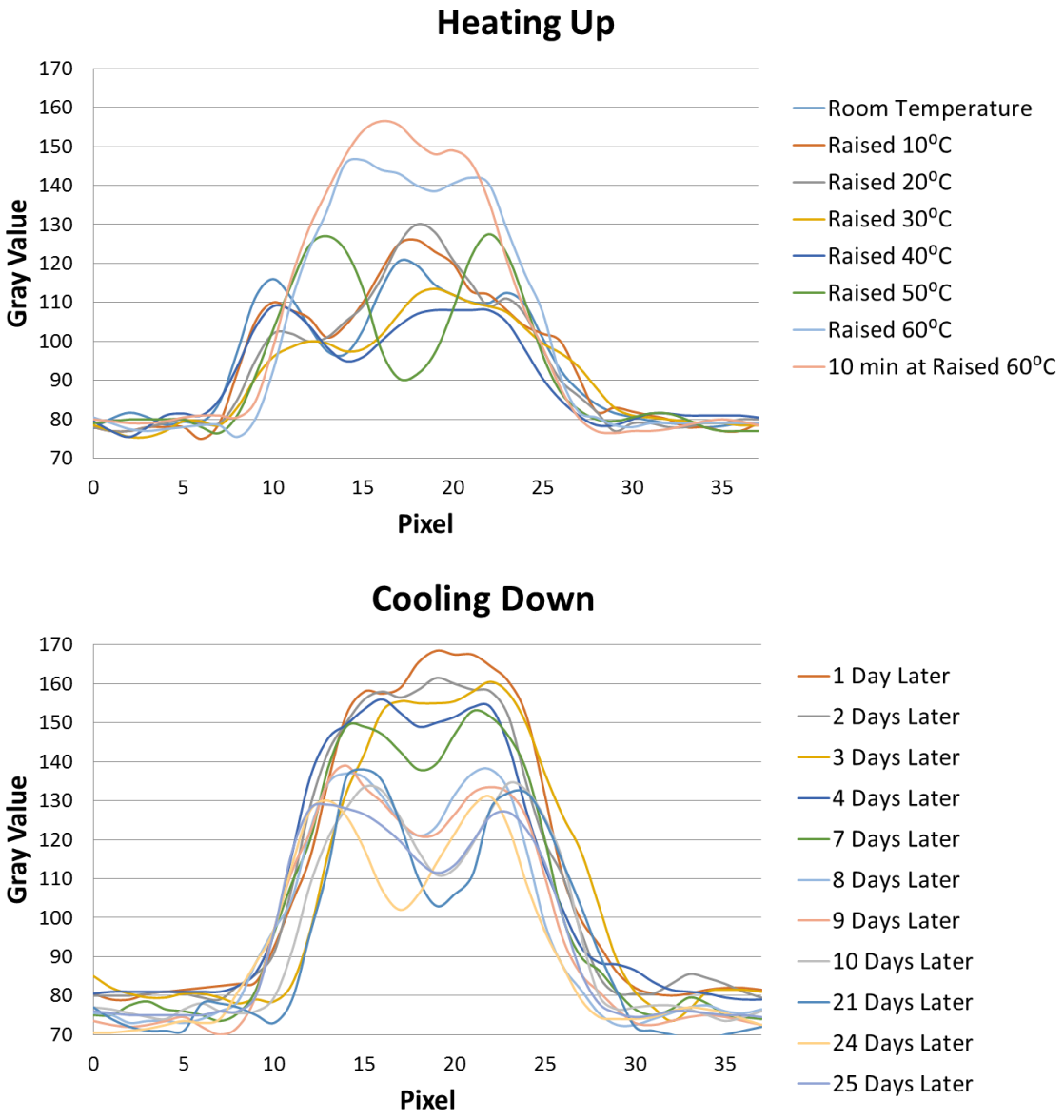

Figure 4.12 The gray value cross section of the bubble shown in Figure 4.11 while heating (top) and cooling (bottom).

4.4 Conclusion

While mechanical exfoliation has been one of the leading methods for creating graphitic samples, this work shows that the different forms of it can lead to different chemical responses. Each of the three different tape methods used in this work made systems that differed in their response to local biased lithography attempts. The Scotch tape appears to have left residues, which while not observable in Raman nor AFM scans, were then oxidized upon the application of an electric field under bias. This gives concerns about how much contamination is being propagated by the generally used method that first isolated graphene. Thermal release tape showed what is believed to be further oxidation at the SiO_2 substrate surrounding the edges of the graphitic materials that was placed under bias. In this case, when the tip came into contact with the graphitic sample, the bias conducted across the graphene sheet and through the layers, leading to high potentials at the interface edges of the graphene/SiO_2, which, under high humidity was able to react. The third mechanical exfoliation method was the water soluble tape, which was able to produce the originally expected locally patterned oxidation of few layer graphene. However, this oxidation was not as well controlled and the biased lithography also led to the formation of graphitic bubbles.

The second original goal of the work, was to create samples that were chemically altered to change the properties of graphene. Originally oxidized graphene was the desired method, but a by-product of the set up provided another means of manipulating graphene's properties. While chemical functionalization is one technique for influencing graphitic properties, so is mechanical strain, which can be created by the formation of

bubbles. In this work a unique way of creating graphitic bubbles was developed which was semi-selective in location as only areas that underwent biased lithography attempts would show bubble formation.

When these bubbles were first observed it was by contact mode AFM, which showed that there were new features that moved with the scanning direction in the friction images, while no changes were observed in the topography. The samples were examined under a 100x objective and showed new features that appeared to be bubbles, or at least have some height due to the change in the color contract. To determine the height, tapping mode AFM was conducted, with which it was observed that the bubbles are in fact there, with heights that ranged from 6.5 nm to 200 nm. Force-distance curves, sample heating and Raman spectroscopy were conducted to show the changes in the properties of the graphitic materials. The force-distance curves showed a higher snap-in force and then prolonged retract curves, indicating that the graphene was able to better surround the tip. This work also supports the theory of the puckering effect[75] used to describe how graphene's friction, as the bubbles led to more tip-graphene interaction, as observed in the force-distance and contact mode results. The bubbles showed a strong reaction to the heating and cooling of the environment, supporting that it is indeed a gas that is causing the bubbles to form. In the Raman spectra it was observed that the characteristic G and 2D peaks changed after the bubble formation. On large bubbles the multilayer graphene showed more bilayer graphene response, with the intensity of the 2D and G peaks being almost even. While the G peak was seen to move to lower wavenumbers as a result of strain the in the carbon-carbon bonds.

Thus it was found that even for mechanical exfoliation, which is supposed to produce very pristine graphene, the specific tape used can have a large impact on the samples. It is also important to note that the sample contamination, while known to happen quickly, can be hard to detect and that sample preparation has a large impact on any future device fabrication. It was also discovered that in samples which had undergone submersion in warm water as part of their sample preparation could lead to bubbles when a bias was applied. These bubbles changed the mechanical responses of the graphitic material as well as the Raman signal. This method of creating regionally selective graphitic bubbles could be further used to selectively react to regions of a graphitic sample as the strain caused by the bubbles should make these areas more reactive.

CHAPTER V

SUMMARY AND OUTLOOK

From pencils to lubricants[2] and from batteries[3] to sample supports,[144] graphitic materials have been incorporated into a wide range of purposes since 1564.[1] Their potential is not limited to these uses though as tailoring of their properties opens new avenues of applications. One way to manipulate graphitic materials is by chemical modification, such as oxidation. In the beginning of this work, two different oxidation techniques and their effects on graphite were explored. The second half of this work investigated the newer graphene and graphitic supported materials and the importance of sample preparation, solvent intercalation, and the chemical and physical modification of these materials.

While Hummers' method or a modified Hummers' method has been used to produce graphitic oxide, these methods require harsh chemical environments and exfoliate the graphite as it chemically converts to graphene oxide.[103,104] In order to have the large scale oxidation without the harsh chemical conditions, this work utilized UV/O_3 exposure to oxidize the graphite. As the amount of exposure time was increased, so did the amount of oxidation. This oxidation was limited to just the top few layers of the graphite on the HOPG substrate and the oxidized surface did not exfoliate. A linear relationship from one of the graphite samples was observed between the length of UV/O_3 exposure to the number of defects, as determined by the intensity of the D/G ratio from Raman spectroscopy. This shows that UV/O_3 lends a controllable manner for

the extent of oxidation. In the center of the studied time range it was found that a 30 minute exposure time led to an average distance between defects of 11.7 nm. At this defect density the graphite was able to maintain its honeycomb structure as confirmed by high resolution AFM scanning.

While UV/O_3 provided an easy platform for large scale graphite oxidation, it did not allow for a local study of the effects of oxidation, which is ideal to compare friction information and to create small patterned areas of the oxidized species. Biased AFM lithography allowed for the localized, controlled patterning of graphite without the exfoliation of the oxidized graphite. Comparing the friction of the highly oxidized graphite to the pristine graphite, there was found to be a seven-fold increase compared to the pristine graphite. This agrees well with the work done by Ko and co-workers which found that graphene on SiO_2 which underwent biased oxidation showed a seven-fold increase in friction.[87] It was also noted during this work that there are many factors which can alter the oxidation process; specifically, the force of adhesion was shown to depend on the applied bias in a complicated manner when the potential approached the bias needed for oxidation. There was also a dependence of the extent of oxidation based on the amount of humidity, bias, and tip speed, which agrees with other work using AFM biased lithography.[117]

For graphene to be used in devices, it is necessary to know how to best make those devices and what types of contamination are to be found. The studies herein investigated three different tapes and methods of mechanical exfoliation. It was found that depending on the type of tape and its sample preparation, the response after

undergoing biased AFM lithography varied. The three tapes and their methods were: Scotch tape, with a simple press and peel; thermal release tape, which underwent heating and then a re-peel with tape; and water soluble tape, which experienced submersion in warm water. The regions of the samples undergoing biased lithography were chosen for the lack of appearance of any tape residue or other visible contaminants as viewed by 100x optical micrographs, Raman spectroscopy, and initial AFM scanning. Biased lithography was attempted by applying a potential between the doped Si and the metallic tip, with the 90 nm SiO_2 and graphitic material between, thus generating an electric field. After biased lithography, three different results were observed for the three different types of samples. The Scotch tape samples showed growths that are believed to be due to the oxidation of the tape residue, extending from the edges of the graphitic region in which the bias was applied. These growths did not show up as graphitic in nature in the Raman spectra, but the friction was closer to that of graphene than the SiO_2 substrate. For the thermal release tape samples, the applied bias led to the formation of wrinkles on the graphitic material and donuts around the edges of the graphitic region. The wrinkles are believed to be due to the pulling in of water that either intercalated due to high humidity or was present from the pressing of the tape under ambient conditions. However, the donuts are thought to be due to the high electric field at the edges leading to the further oxidation of the SiO_2 substrate. When the local oxidation was attempted on few layer graphene using samples made with water soluble tape, it was found that besides oxidizing some of the graphitic regions, bubbles could also be formed. All of these samples only showed changes near or on the graphitic region in which the biased

lithography was conducted. The graphitic regions are conductive, so when the tip came into contact, the potential was able to spread throughout the region, which led to reactions on the entire region or on the edges with the substrate instead of solely the dimensions where the tip came into direct contact. These different results show that more needs to be done to ensure the purity of graphitic samples and that Raman spectroscopy is not sufficient to guarantee sample uniformity as all of the samples in this work showed the same initial Raman spectra response. It was also concluded that the way in which a sample or device is prepared can have a large impact on the way it reacts later.

The initial intent for attempting biased lithography was to chemically change the graphitic material, which would tune the electronic and chemical properties of the material. Oxidation of the graphitic materials was only achieved on the samples prepared with water soluble tape. Outside of this graphitic oxidation, there was also the formation of graphitic bubbles. Mechanical strain, such as that created in formation of these graphitic bubbles, also changes the electronic and chemical properties of graphitic material,[99,167] and thus also achieves the original purpose of the experiments. As part of the sample preparation for the water soluble tape method, the sample was submersed in hot water, allowing for possible water intercalation. The formation of bubbles on the water soluble tape is thought to be due to this intercalated water, either between the layers or between the graphitic material and the substrate, which decomposed in the high electric field to form hydrogen and oxygen gas. The tapping mode and contact mode images showed that the bubbles greatly varied in height ranging from 8 nm to about 200

nm, with friction responses showing the movement of the raised graphitic material along the scan direction. Upon heating, the bubbles were observed to change in size and shape, even after just a 10°C increase in temperature, supporting the hypothesis that it was indeed a gas in the bubble which then expanded with temperature. The properties of the bubbles were studied with force distance-curves, in which an extended pull-off force was observed. This force-distance curve response supports the theory for why the coefficient of friction can be negative as proposed by Deng and co-workers in which the tip is able to lift layers of graphite as it retracts from the graphitic surface.[75] Raman spectroscopy conducted on the large bubbles showed the change in the graphitic lattice with the downshifting of the G band, indicating a change in the carbon-carbon bond distance. This is a new method for bubble formation and completely different from the other techniques in the current literature.

There are many directions where the knowledge gained in this work from the oxidized graphite, oxidized graphene and nanobubble surfaces conducted in this work can be applied. The formation of complex surfaces on graphite by further reacting the oxidized species with click-chemistry reactions could develop a multi-faceted platform for binding materials that require a conductive substrate. This knowledge also could be used to directly bind multilayer graphite to a surface for solid lubrication, or it could serve as a platform for work that can be applied to graphene. Oxidized graphene, as in the case for oxidized graphite, allows for further reaction with the oxygen species for the development of complex systems, and it also opens the band gap so that the graphitic material can be used in FETs. The discovery of the ability to create bubbles by using

samples that had been submersed in warm water demonstrates a new method of creating a strained graphitic sample. Future work on the bubbled graphitic material might include intercalating other reactants in with the water, which could undergo further reactions in the high electric field, high pressure or by creating high temperatures similar to work done with graphene on diamond.[98] Because graphene is transparent, these reactions could be analyzed in-situ. The bubbles themselves create higher reactivity in graphitic materials, so reactions could be selectively directed onto the bubbles. Another route for the usage of graphene bubbles could be the formation of 2-dimensional lenses, as suggested by Georgiou and co-workers.[92]

REFERENCES

(1) Castro Neto, A. H.; Guinea, F.; Peres, N. M. R.; Novoselov, K. S.; Geim, A. K. *Rev. Mod. Phys.* **2009**, *81*, 109.

(2) Gopal, A. V.; Rao, P. V. *Mater. Manuf. Processes* **2004**, *19*, 177.

(3) Park, M. S.; Lee, Y. J.; Rajendran, S.; Song, M. S.; Kim, H. S.; Lee, J. Y. *Electrochim. Acta* **2005**, *50*, 5561.

(4) Beitel, G. *J. Vac. Sci. Technol.* **1971**, *8*, 647.

(5) Kroto, H. W.; Heath, J. R.; Obrien, S. C.; Curl, R. F.; Smalley, R. E. *Nature* **1985**, *318*, 162.

(6) Iijima, S. *Nature* **1991**, *354*, 56.

(7) Novoselov, K. S.; Geim, A. K.; Morozov, S. V.; Jiang, D.; Zhang, Y.; Dubonos, S. V.; Grigorieva, I. V.; Firsov, A. A. *Science* **2004**, *306*, 666.

(8) Peierls, R. E. *Helv. Phys. Acta* **1934**, *7*, 81.

(9) Landau, L. D. *Physikalische Zeitschrift der Sowjetunion* **1937**, *11*, 545.

(10) Mermin, N. D. *Phys. Rev.* **1968**, *176*, 250.

(11) Lee, C.; Wei, X. D.; Kysar, J. W.; Hone, J. *Science* **2008**, *321*, 385.

(12) Berger, C.; Song, Z. M.; Li, T. B.; Li, X. B.; Ogbazghi, A. Y.; Feng, R.; Dai, Z. T.; Marchenkov, A. N.; Conrad, E. H.; First, P. N.; de Heer, W. A. *J. Phys. Chem. B* **2004**, *108*, 19912.

(13) Kim, K. S.; Zhao, Y.; Jang, H.; Lee, S. Y.; Kim, J. M.; Ahn, J. H.; Kim, P.; Choi, J. Y.; Hong, B. H. *Nature* **2009**, *457*, 706.

(14) Dresselhaus, M. S.; Kalish, R. *Ion Implantation in Diamond, Graphite, and Related Materials*; Springer-Verlag: Berlin, Germany, 1992.

(15) Reina, A.; Jia, X. T.; Ho, J.; Nezich, D.; Son, H. B.; Bulovic, V.; Dresselhaus, M. S.; Kong, J. *Nano Lett.* **2009**, *9*, 30.

(16) Stankovich, S.; Dikin, D. A.; Piner, R. D.; Kohlhaas, K. A.; Kleinhammes, A.; Jia, Y.; Wu, Y.; Nguyen, S. T.; Ruoff, R. S. *Carbon* **2007**, *45*, 1558.

(17) Najafabadi, A. T.; Gyenge, E. *Carbon* **2014**, *71*, 58.

(18) Xiao, B. W.; Li, X. F.; Li, X.; Wang, B. Q.; Langford, C.; Li, R. Y.; Sun, X. L. *J. Phys. Chem. C* **2014**, *118*, 881.

(19) Giannazzo, F.; Deretzis, I.; Nicotra, G.; Fisichella, G.; Spinella, C.; Roccaforte, F.; La Magna, A. *Appl. Surf. Sci.* **2014**, *291*, 53.

(20) Berman, D.; Erdemir, A.; Sumant, A. V. *Mater. Today* **2014**, *17*, 31.

(21) Rezania, B.; Dorn, M.; Severin, N.; Rabe, J. P. *J. Colloid Interface Sci.* **2013**, *407*, 500.

(22) Moser, J.; Verdaguer, A.; Jimenez, D.; Barreiro, A.; Bachtold, A. *Appl. Phys. Lett.* **2008**, *92*, 3.

(23) Zhang, Y.; Zhang, L. Y.; Zhou, C. W. *Acc. Chem. Res.* **2013**, *46*, 2329.

(24) Chua, C. K.; Pumera, M. *Chem. Soc. Rev.* **2014**, *43*, 291.

(25) Kang, J.; Shin, D.; Bae, S.; Hong, B. H. *Nanoscale* **2012**, *4*, 5527.

(26) Wallace, P. R. *Phys. Rev.* **1947**, *71*, 622.

(27) Du, X.; Skachko, I.; Barker, A.; Andrei, E. Y. *Nat. Nanotechnol.* **2008**, *3*, 491.

(28) Bourzac, K. *Nature* **2012**, *483*, S34.

(29) Hilsum, C. *Electron. Lett* **1974**, *10*, 259.

(30) Podzorov, V.; Menard, E.; Borissov, A.; Kiryukhin, V.; Rogers, J. A.; Gershenson, M. E. *Phys. Rev. Lett.* **2004**, *93*, 4.

(31) Zhang, Y. B.; Tan, Y. W.; Stormer, H. L.; Kim, P. *Nature* **2005**, *438*, 201.

(32) Emtsev, K. V.; Bostwick, A.; Horn, K.; Jobst, J.; Kellogg, G. L.; Ley, L.; McChesney, J. L.; Ohta, T.; Reshanov, S. A.; Rohrl, J.; Rotenberg, E.; Schmid, A. K.; Waldmann, D.; Weber, H. B.; Seyller, T. *Nat. Mater.* **2009**, *8*, 203.

(33) Caldwell, J. D.; Anderson, T. J.; Culbertson, J. C.; Jernigan, G. G.; Hobart, K. D.; Kub, F. J.; Tadjer, M. J.; Tedesco, J. L.; Hite, J. K.; Mastro, M. A.; Myers-Ward, R. L.; Eddy, C. R.; Campbell, P. M.; Gaskill, D. K. *ACS Nano* **2010**, *4*, 1108.

(34) Novoselov, K. S.; Geim, A. K.; Morozov, S. V.; Jiang, D.; Katsnelson, M. I.; Grigorieva, I. V.; Dubonos, S. V.; Firsov, A. A. *Nature* **2005**, *438*, 197.

(35) Dusari, S.; Barzola-Quiquia, J.; Esquinazi, P.; Garcia, N. *Phys. Rev. B* **2011**, *83*, 6.

(36) Baringhaus, J.; Ruan, M.; Edler, F.; Tejeda, A.; Sicot, M.; Taleb-Ibrahimi, A.; Li, A. P.; Jiang, Z. G.; Conrad, E. H.; Berger, C.; Tegenkamp, C.; de Heer, W. A. *Nature* **2014**, *506*, 349.

(37) Kim, H.; Kim, K. K.; Lee, S. N.; Ryou, J. H.; Dupuis, R. D. *Appl. Phys. Lett.* **2011**, *98*, 3.

(38) Esquinazi, P.; Barzola-Quiquia, J.; Dusari, S.; Garcia, N. *J. Appl. Phys.* **2012**, *111*, 4.

(39) Han, M. Y.; Ozyilmaz, B.; Zhang, Y. B.; Kim, P. *Phys. Rev. Lett.* **2007**, *98*, 4.

(40) Obradovic, B.; Kotlyar, R.; Heinz, F.; Matagne, P.; Rakshit, T.; Giles, M. D.; Stettler, M. A.; Nikonov, D. E. *Appl. Phys. Lett.* **2006**, *88*, 3.

(41) Todd, K.; Chou, H. T.; Amasha, S.; Goldhaber-Gordon, D. *Nano Lett.* **2009**, *9*, 416.

(42) Han, M. Y.; Brant, J. C.; Kim, P. *Phys. Rev. Lett.* **2010**, *104*, 4.

(43) Schedin, F.; Geim, A. K.; Morozov, S. V.; Hill, E. W.; Blake, P.; Katsnelson, M. I.; Novoselov, K. S. *Nat. Mater.* **2007**, *6*, 652.

(44) Jin, W. F.; Gao, Z. W.; Zhou, Y.; Yu, B.; Zhang, H.; Peng, H. L.; Liu, Z. F.; Dai, L. *J. Mater. Chem. C* **2014**, *2*, 1592.

(45) Fiori, G.; Neumaier, D.; Szafranek, B. N.; Iannaccone, G. *IEEE Trans. Electron Devices* **2014**, *61*, 729.

(46) Pletikosic, I.; Kralj, M.; Pervan, P.; Brako, R.; Coraux, J.; N'Diaye, A. T.; Busse, C.; Michely, T. *Phys. Rev. Lett.* **2009**, *102*, 4.

(47) Tang, Q.; Zhou, Z.; Chen, Z. F. *Nanoscale* **2013**, *5*, 4541.

(48) Nakaharai, S.; Iijima, T.; Ogawa, S.; Suzuki, S.; Li, S. L.; Tsukagoshi, K.; Sato, S.; Yokoyama, N. *ACS Nano* **2013**, *7*, 5694.

(49) Mitoma, N.; Nouchi, R.; Tanigaki, K. *J. Phys. Chem. C* **2013**, *117*, 1453.

(50) Liu, F.; Kim, Y. H.; Cheon, D. S.; Seo, T. S. *Sens. Actuators, B* **2013**, *186*, 252.

(51) Yang, D. P.; Wang, X. S.; Guo, X. J.; Zhi, X.; Wang, K.; Li, C.; Huang, G. S.; Shen, G. X.; Mei, Y. F.; Cui, D. X. *J. Phys. Chem. C* **2014**, *118*, 725.

(52) Chung, M. G.; Kim, D. H.; Lee, H. M.; Kim, T.; Choi, J. H.; Seo, D. K.; Yoo, J. B.; Hong, S. H.; Kang, T. J.; Kim, Y. H. *Sens. Actuators, B* **2012**, *166*, 172.

(53) Hafiz, S. M.; Ritikos, R.; Whitcher, T. J.; Razib, N. M.; Bien, D. C. S.; Chanlek, N.; Nakajima, H.; Saisopa, T.; Songsiriritthigul, P.; Huang, N. M.; Rahman, S. A. *Sens. Actuators, B* **2014**, *193*, 692.

(54) Quang, V. V.; Trong, N. S.; Trung, N. N.; Hoa, N. D.; Duy, N. V.; Hieu, N. V. *Anal. Lett.* **2014**, *47*, 280.

(55) Berger, C.; Song, Z. M.; Li, X. B.; Wu, X. S.; Brown, N.; Naud, C.; Mayou, D.; Li, T. B.; Hass, J.; Marchenkov, A. N.; Conrad, E. H.; First, P. N.; de Heer, W. A. *Science* **2006**, *312*, 1191.

(56) Kim, E. A.; Neto, A. H. C. *EPL* **2008**, *84*, 5.

(57) Zong, Z.; Chen, C. L.; Dokmeci, M. R.; Wan, K. T. *J. Appl. Phys.* **2010**, *107*, 3.

(58) Levy, N.; Burke, S. A.; Meaker, K. L.; Panlasigui, M.; Zettl, A.; Guinea, F.; Neto, A. H. C.; Crommie, M. F. *Science* **2010**, *329*, 544.

(59) Yu, T.; Ni, Z. H.; Du, C. L.; You, Y. M.; Wang, Y. Y.; Shen, Z. X. *J. Phys. Chem. C* **2008**, *112*, 12602.

(60) Bunch, J. S.; Verbridge, S. S.; Alden, J. S.; van der Zande, A. M.; Parpia, J. M.; Craighead, H. G.; McEuen, P. L. *Nano Lett.* **2008**, *8*, 2458.

(61) Huang, M. Y.; Yan, H. G.; Heinz, T. F.; Hone, J. *Nano Lett.* **2010**, *10*, 4074.

(62) Nguyen, V. H.; Nguyen, H. V.; Dollfus, P. *Nanotechnology* **2014**, *25*, 7.

(63) Meric, I.; Han, M. Y.; Young, A. F.; Ozyilmaz, B.; Kim, P.; Shepard, K. L. *Nat. Nanotechnol.* **2008**, *3*, 654.

(64) Cocco, G.; Cadelano, E.; Colombo, L. *Phys. Rev. B* **2010**, *81*, 4.

(65) Qu, L. H.; Zhang, J. M.; Xu, K. W.; Ji, V. *Phys. E (Amsterdam, Neth.)* **2014**, *56*, 55.

(66) Lu, Y.; Guo, J. *Nano Res.* **2010**, *3*, 189.

(67) Savage, N. *Nature* **2012**, *483*, S30.

(68) Grierson, D. S.; Carpick, R. W. *Nano Today* **2007**, *2*, 12.

(69) Bartz, W. J. *Wear* **1971**, *17*, 421.

(70) Li, L. X.; Peng, D. S.; Liu, J. A.; Liu, Z. Q. *J. Mater. Process. Technol.* **2001**, *112*, 1.

(71) Dienwiebel, M.; Verhoeven, G. S.; Pradeep, N.; Frenken, J. W. M.; Heimberg, J. A.; Zandbergen, H. W. *Phys. Rev. Lett.* **2004**, *92*, 4.

(72) Rudnck, L. *Lubricant additives chemistry and applications*; M. Dekker: New York City, NY, 2003.

(73) Sprayon, Product Information- Dry Film Graphite Lubricant. www.sprayon.com/products/dry_film_graphite_lubricant. (accessed Feb 7, 2013).

(74) Lee, C.; Li, Q. Y.; Kalb, W.; Liu, X. Z.; Berger, H.; Carpick, R. W.; Hone, J. *Science* **2010**, *328*, 76.

(75) Deng, Z.; Smolyanitsky, A.; Li, Q. Y.; Feng, X. Q.; Cannara, R. J. *Nat. Mater.* **2012**, *11*, 1032.

(76) Li, Q. Y.; Lee, C.; Carpick, R. W.; Hone, J. *Phys. Status Solidi B* **2010**, *247*, 2909.

(77) Wang, Y. Y.; Ni, Z. H.; Yu, T.; Shen, Z. X.; Wang, H. M.; Wu, Y. H.; Chen, W.; Wee, A. T. S. *J. Phys. Chem. C* **2008**, *112*, 10637.

(78) Filleter, T.; McChesney, J. L.; Bostwick, A.; Rotenberg, E.; Emtsev, K. V.; Seyller, T.; Horn, K.; Bennewitz, R. *Phys. Rev. Lett.* **2009**, *102*.

(79) Schriver, M.; Regan, W.; Gannett, W. J.; Zaniewski, A. M.; Crommie, M. F.; Zettl, A. *ACS Nano* **2013**, *7*, 5763.

(80) Xu, K.; Cao, P. G.; Heath, J. R. *Science* **2010**, *329*, 1188.

(81) Severin, N.; Lange, P.; Sokolov, I. M.; Rabe, J. P. *Nano Lett.* **2012**, *12*, 774.

(82) Gao, L. B.; Ni, G. X.; Liu, Y. P.; Liu, B.; Neto, A. H. C.; Loh, K. P. *Nature* **2014**, *505*, 190.

(83) Yoon, T.; Mun, J. H.; Cho, B. J.; Kim, T. S. *Nanoscale* **2014**, *6*, 151.

(84) Gao, W.; Xiao, P.; Henkelman, G.; Liechti, K. M.; Huang, R. *arXiv* **2014**, *1403.3751*.

(85) Feng, X. F.; Maier, S.; Salmeron, M. *J. Am. Chem. Soc.* **2012**, *134*, 5662.

(86) Acik, M.; Mattevi, C.; Gong, C.; Lee, G.; Cho, K.; Chhowalla, M.; Chabal, Y. J. *ACS Nano* **2010**, *4*, 5861.

(87) Ko, J. H.; Kwon, S.; Byun, I. S.; Choi, J. S.; Park, B. H.; Kim, Y. H.; Park, J. Y. *Tribol. Lett.* **2013**, *50*, 137.

(88) Kinoshita, H.; Nishina, Y.; Alias, A. A.; Fujii, M. *Carbon* **2014**, *66*, 720.

(89) Liang, H. Y.; Bu, Y. F.; Zhang, J. Y.; Cao, Z. Y.; Liang, A. M. *ACS Appl. Mater. Interfaces* **2013**, *5*, 6369.

(90) Ou, J. F.; Wang, J. Q.; Liu, S.; Mu, B.; Ren, J. F.; Wang, H. G.; Yang, S. R. *Langmuir* **2010**, *26*, 15830.

(91) Lee, J. U.; Yoon, D.; Cheong, H. *Nano Lett.* **2012**, *12*, 4444.

(92) Georgiou, T.; Britnell, L.; Blake, P.; Gorbachev, R. V.; Gholinia, A.; Geim, A. K.; Casiraghi, C.; Novoselov, K. S. *Appl. Phys. Lett.* **2011**, *99*, 3.

(93) Boddeti, N. G.; Liu, X. H.; Long, R.; Xiao, J. L.; Bunch, J. S.; Dunn, M. L. *Nano Lett.* **2013**, *13*, 6216.

(94) Trabelsi, A. B. G.; Kusmartsev, F. V.; Robinson, B. J.; Ouerghi, A.; Kusmartseva, O. E.; Kolosov, O. V.; Mazzocco, R.; Gaifullin, M. B.; Oueslati, M. *Nanotechnology* **2014**, *25*, 165704.

(95) Koenig, S. P.; Wang, L. D.; Pellegrino, J.; Bunch, J. S. *Nat. Nanotechnol.* **2012**, *7*, 728.

(96) Berry, V. *Carbon* **2013**, *62*, 1.

(97) Wu, Q. Z.; Wu, Y. P.; Hao, Y. F.; Geng, J. X.; Charlton, M.; Chen, S. S.; Ren, Y. J.; Ji, H. X.; Li, H. F.; Boukhvalov, D. W.; Piner, R. D.; Bielawski, C. W.; Ruoff, R. S. *Chem. Commun.* **2013**, *49*, 677.

(98) Lim, C.; Nesladek, M.; Loh, K. P. *Angew. Chem. Int. Ed.* **2014**, *53*, 215.

(99) Bissett, M. A.; Konabe, S.; Okada, S.; Tsuji, M.; Ago, H. *ACS Nano* **2013**, *7*, 10335.

(100) Zhang, Y. H.; Fu, Q.; Cui, Y.; Mu, R. T.; Jin, L.; Bao, X. H. *PCCP* **2013**, *15*, 19042.

(101) Lim, C.; Sorkin, A.; Bao, Q. L.; Li, A.; Zhang, K.; Nesladek, M.; Loh, K. P. *Nat. Commun.* **2013**, *4*, 8.

(102) Perucchi, A.; Baldassarre, L.; Marini, C.; Postorino, P.; Bernardini, F.; Massidda, S.; Lupi, S. *Phys. Rev. B* **2012**, *86*, 4.

(103) Hummers, W. S.; Offeman, R. E. *J. Am. Chem. Soc.* **1958**, *80*, 1339.

(104) Chen, D.; Feng, H. B.; Li, J. H. *Chem. Rev.* **2012**, *112*, 6027.

(105) Wang, L. Y.; Park, Y.; Cui, P.; Bak, S.; Lee, H.; Lee, S. M. *Chem. Commun.* **2014**, *50*, 1224.

(106) Xu, C.; Yang, D. R.; Mei, L.; Li, Q. H.; Zhu, H. Z.; Wang, T. H. *ACS Appl. Mater. Interfaces* **2013**, *5*, 12911.

(107) Wei, N.; Lv, C.; Xu, Z. *Langmuir* **2014**, *30*, 3572.

(108) Yan, J. A.; Xian, L. D.; Chou, M. Y. *Phys. Rev. Lett.* **2009**, *103*, 4.

(109) Dreyer, D. R.; Park, S.; Bielawski, C. W.; Ruoff, R. S. *Chem. Soc. Rev.* **2010**, *39*, 228.

(110) Dimiev, A.; Tour, J. *ACS Nano* **2014**, *8*, 3060.

(111) Binnig, G.; Quate, C. F.; Gerber, C. *Phys. Rev. Lett.* **1986**, *56*, 930.

(112) Majumdar, A.; Oden, P. I.; Carrejo, J. P.; Nagahara, L. A.; Graham, J. J.; Alexander, J. *Appl. Phys. Lett.* **1992**, *61*, 2293.

(113) Leggett, G. J. *Chem. Soc. Rev.* **2006**, *35*, 1150.

(114) Dagata, J. A.; Schneir, J.; Harary, H. H.; Evans, C. J.; Postek, M. T.; Bennett, J. *Appl. Phys. Lett.* **1990**, *56*, 2001.

(115) Giesbers, A. J. M.; Zeitler, U.; Neubeck, S.; Freitag, F.; Novoselov, K. S.; Maan, J. C. *Solid State Commun.* **2008**, *147*, 366.

(116) Weng, L. S.; Zhang, L. Y.; Chen, Y. P.; Rokhinson, L. P. *Appl. Phys. Lett.* **2008**, *93*, 3.

(117) Kumar, K.; Strauf, S.; Yang, E. H. *Nanosci. Nanotechnol. Lett.* **2010**, *2*, 185.

(118) Ferrari, A. C. *Solid State Commun.* **2007**, *143*, 47.

(119) Estrade-Szwarckopf, H. *Carbon* **2004**, *42*, 1713.

(120) Yang, D.; Velamakanni, A.; Bozoklu, G.; Park, S.; Stoller, M.; Piner, R. D.; Stankovich, S.; Jung, I.; Field, D. A.; Ventrice, C. A.; Ruoff, R. S. *Carbon* **2009**, *47*, 145.

(121) Tuinstra, F.; Koenig, J. L. *J. Chem. Phys.* **1970**, *53*, 1126.

(122) Ferrari, A. C.; Robertson, J. *Phys. Rev. B* **2000**, *61*, 14095.

(123) Lucchese, M. M.; Stavale, F.; Ferreira, E. H. M.; Vilani, C.; Moutinho, M. V. O.; Capaz, R. B.; Achete, C. A.; Jorio, A. *Carbon* **2010**, *48*, 1592.

(124) Ferrari, A. C.; Basko, D. M. *Nat. Nanotechnol.* **2013**, *8*, 235.

(125) Dresselhaus, M. S.; Jorio, A.; Souza, A. G.; Saito, R. *Philos. Trans. R. Soc., A* **2010**, *368*, 5355.

(126) Calizo, I.; Bao, W. Z.; Miao, F.; Lau, C. N.; Balandin, A. A. *Appl. Phys. Lett.* **2007**, *91*, 3.

(127) Calizo, I.; Ghosh, S.; Bao, W. Z.; Miao, F.; Lau, C. N.; Balandin, A. A. *Solid State Commun.* **2009**, *149*, 1132.

(128) Tsukamoto, T.; Yamazaki, K.; Komurasaki, H.; Ogino, T. *J. Phys. Chem. C* **2012**, *116*, 4732.

(129) Kanchanapally, R.; Sinha, S. S.; Fan, Z.; Dubey, M.; Zaka, E.; Ray, P. C. *J. Phys. Chem. C* **2014**, *118*, 7070.

(130) Park, W.-H. *J. Phys. Chem. C* **2014**, *118*, 6989.

(131) Blake, P.; Hill, E. W.; Neto, A. H. C.; Novoselov, K. S.; Jiang, D.; Yang, R.; Booth, T. J.; Geim, A. K. *Appl. Phys. Lett.* **2007**, *91*, 3.

(132) Brigham Young University, Silicon Dioxide/Nitride Color vs. Film Thickness and Viewing Angle Calculator. Cleanroom BYU. www.cleanroom.byu.edu/color_chart.phtml (accessed Feb 12, 2014).

(133) Martinez-Martin, D.; Longuinhos, R.; Izquierdo, J. G.; Marele, A.; Alexandre, S. S.; Jaafar, M.; Gomez-Rodriguez, J. M.; Banares, L.; Soler, J. M.; Gomez-Herrero, J. *Carbon* **2013**, *61*, 33.

(134) Kozbial, A.; Li, Z.; Zun, J.; Gong, X.; Zhou, F.; Wang, Y.; Xu, H.; Liu, H.; Li, L. *Carbon* **2014**, *74*, 218.

(135) MikroMasch, SPM Probes & Test Structures MikroMasch Product Catalogue. http://www.spmtips.com/pdf_downloads/MikroMasch-Product-Catalogue-2013.pdf (accessed Mar 25, 2014).

(136) Mate, C. M.; McClelland, G. M.; Erlandsson, R.; Chiang, S. *Phys. Rev. Lett.* **1987**, *59*, 1942.

(137) Snow, E. S.; Campbell, P. M. *Appl. Phys. Lett.* **1994**, *64*, 1932.

(138) Byun, I. S.; Yoon, D.; Choi, J. S.; Hwang, I.; Lee, D. H.; Lee, M. J.; Kawai, T.; Son, Y. W.; Jia, Q.; Cheong, H.; Park, B. H. *ACS Nano* **2011**, *5*, 6417.

(139) Sader, J. E.; Chon, J. W. M.; Mulvaney, P. *Rev. Sci. Instrum.* **1999**, *70*, 3967.

(140) Wojdyr, M. *J. Appl. Crystallogr.* **2010**, *43*, 1126.

(141) Sheiko, S. S.; Moller, M.; Reuvekamp, E.; Zandbergen, H. W. *Phys. Rev. B* **1993**, *48*, 5675.

(142) Asay, D. B.; Hsiao, E.; Kim, S. H. *Rev. Sci. Instrum.* **2009**, *80*, 3.

(143) Pierson, H. O. *Handbook of Carbon, Graphite, Diamond and Fullerenes Properties, Processing and Applications* Noyes Publications: Park Ridge, New Jersey, 1993.

(144) Li, M.; Deng, K.; Yang, Y. L.; Zeng, Q. D.; He, M.; Wang, C. *Phys. Rev. B* **2007**, *76*, 5.

(145) Booth, T. J.; Blake, P.; Nair, R. R.; Jiang, D.; Hill, E. W.; Bangert, U.; Bleloch, A.; Gass, M.; Novoselov, K. S.; Katsnelson, M. I.; Geim, A. K. *Nano Lett.* **2008**, *8*, 2442.

(146) Kwon, S.; Ko, J. H.; Jeon, K. J.; Kim, Y. H.; Park, J. Y. *Nano Lett.* **2012**, *12*, 6043.

(147) Rourke, J. P.; Pandey, P. A.; Moore, J. J.; Bates, M.; Kinloch, I. A.; Young, R. J.; Wilson, N. R. *Angew. Chem. Int. Ed.* **2011**, *50*, 3173.

(148) Bonanni, A.; Ambrosi, A.; Chua, C. K.; Pumera, M. *ACS Nano* **2014**, *8*, 4197.

(149) Huh, S.; Park, J.; Kim, Y. S.; Kim, K. S.; Hong, B. H.; Nam, J. M. *ACS Nano* **2011**, *5*, 9799.

(150) Simmons, J. M.; Nichols, B. M.; Baker, S. E.; Marcus, M. S.; Castellini, O. M.; Lee, C. S.; Hamers, R. J.; Eriksson, M. A. *J. Phys. Chem. B* **2006**, *110*, 7113.

(151) Park, H.; Oh, S.; Kimz, J. *ECS Solid State Letters* **2014**, *3*, M15.

(152) Zhao, S. C.; Surwade, S. P.; Li, Z. T.; Liu, H. T. *Nanotechnology* **2012**, *23*, 6.

(153) Xu, K.; Ye, P. *J. Phys. Chem. C* **2014**, *118*, 10400.

(154) Cambel, V.; Martaus, J.; Soltys, J.; Kudela, R.; Gregusova, D. *Ultramicroscopy* **2008**, *108*, 1021.

(155) Bhushan, B. *Tribol. Lett.* **1998**, *4*, 1.

(156) Reich, S.; Thomsen, C. *Philos. Trans. R. Soc., A* **2004**, *362*, 2271.

(157) Geng, J.; Jung, H. *J. Phys. Chem. C* **2010**, *114*, 8227.

(158) Tivanski, A. V.; Bemis, J. E.; Akhremitchev, B. B.; Liu, H. Y.; Walker, G. C. *Langmuir* **2003**, *19*, 1929.

(159) Geim, A. K.; Novoselov, K. S. *Nat. Mater.* **2007**, *6*, 183.

(160) Zhang, L. M.; Diao, S. O.; Nie, Y. F.; Yan, K.; Liu, N.; Dai, B. Y.; Xie, Q.; Reina, A.; Kong, J.; Liu, Z. F. *J. Am. Chem. Soc.* **2011**, *133*, 2706.

(161) Sarno, M.; Senatore, A.; Cirillo, C.; Petrone, V.; Ciambelli, P. *J. Nanosci. Nanotechnol.* **2014**, *14*, 4960.

(162) Tian, H.; Li, C.; Ali, M. M.; Cui, Y.-L.; Mi, W.-T.; Yang, Y.; Xie, D.; Ren, T.-L. *ACS Nano* **2014**, *6*, 5883.

(163) Choi, W.; Lahiri, I.; Seelaboyina, R.; Kang, Y. S. *Crit. Rev. Solid State Mater. Sci.* **2010**, *35*, 52.

(164) Deng, C.; Lin, W.; Agnus, G.; Dragoe, D.; Pierucci, D.; Ouerghi, A.; Emer, S.; Barisic, I.; Ravelosona, D.; Chappert, C.; Zhao, W. *J. Phys. Chem. C* **2014**, *25*, 13890.

(165) Stolyarova, E.; Stolyarov, D.; Bolotin, K.; Ryu, S.; Liu, L.; Rim, K. T.; Klima, M.; Hybertsen, M.; Pogorelsky, I.; Pavlishin, I.; Kusche, K.; Hone, J.; Kim, P.; Stormer, H. L.; Yakimenko, V.; Flynn, G. *Nano Lett.* **2009**, *9*, 332.

(166) Yue, K. M.; Gao, W.; Huang, R.; Liechti, K. M. *J. Appl. Phys.* **2012**, *112*, 8.

(167) Guinea, F.; Katsnelson, M. I.; Geim, A. K. *Nat. Phys.* **2010**, *6*, 30.

(168) Gao, W.; Xiao, P.; Henkelman, G.; Liechti, K. M.; Huang, R. *J. Phys. D: Appl. Phys.* **2014**, *47*.

(169) Lee, M. J.; Choi, J. S.; Kim, J. S.; Byun, I. S.; Lee, D. H.; Ryu, S.; Lee, C.; Park, B. H. *Nano Res.* **2012**, *5*, 710.

(170) Wang, B.; Woo, C. H. *J. Appl. Phys.* **2003**, *94*, 4053.

(171) Rossmeisl, J.; Qu, Z. W.; Zhu, H.; Kroes, G. J.; Norskov, J. K. *J. Electroanal. Chem.* **2007**, *607*, 83.

(172) Mohiuddin, T. M. G.; Lombardo, A.; Nair, R. R.; Bonetti, A.; Savini, G.; Jalil, R.; Bonini, N.; Basko, D. M.; Galiotis, C.; Marzari, N.; Novoselov, K. S.; Geim, A. K.; Ferrari, A. C. *Phys. Rev. B* **2009**, *79*, 8.

(173) Weder, G.; Voros, J.; Giazzon, M.; Matthey, N.; Heinzelmann, H.; Liley, M. *Biointerphases* **2009**, *4*, 27.

(174) O'Connell, C. D.; Higgins, M. J.; Marusic, D.; Moulton, S. E.; Wallace, G. G. *Langmuir* **2014**, *30*, 2712.